UNIVERSITY
— OF —
JOHANNESBURG

How to cite this thesis

Machine learning prediction of Nd:YAG Laser welded sintered Metallic alloy: Mechanical Properties

Olanipekun Ayorinde Tayo

Supervised by Prof. Madindwa Mashinini

Co-Supervised by Dr. Maledi Nthabiseng

A thesis presented for the degree of Doctor of Philosophy

FACULTY OF ENGINEERING AND BUILT ENVIRONMENT

Department of Mechanical Engineering science University of Johannesburg

November, 2020

Machine learning modelling of Mechanical properties in Nd-YAG laser welded sintered Metallic alloy
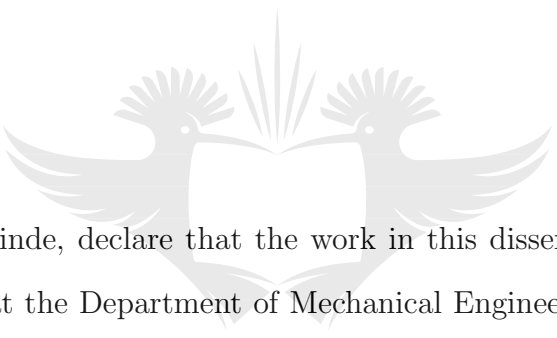
Dedication

I dedicate this thesis to my son, Sasaeniyan Olanipekun, for inspiring me to succeed.

Declaration

I, Olanipekun Ayorinde, declare that the work in this dissertation is based on research carried out at the Department of Mechanical Engineering, University of Johannesburg, in South Africa. No part of this dissertation has been submitted elsewhere for any other degree or qualification.

_____   _____

Olanipekun Ayorinde   Date

Acknowledgements

Acronym

ANN Artificial Neural Network

BM Base Metal

DSS Duplex stainless steel

EBSD Electron backscatter diffraction

FZ Fusion zone

GA Genetic Algorithm

GE General Electric

HAZ Heat affected zone

HV Vickers hardness

LASER Laser Amplified by Stimulated Emission of Radiation

Nd:YAG Neodymium-doped Yttrium-Aluminium-Garnet

ML Machine learning

OM Optical microscope

OM Optical Microscopy

PM Powder Metallurgy

PWHT Post weld heat treatment

S-temp Sintering Temperature

S-time Sintering time

SPS Spark Plasma Sintering

SVM Support Vector Machine

Wel-speed Welding speed

Wel-power welding power

WM Weld Metal

XCT X-Ray Computed Tomography

XRD X-Ray Diffraction

List of Symbols

The following list describes several symbols introduced within the body of the document

ρ_w density of the distilled water
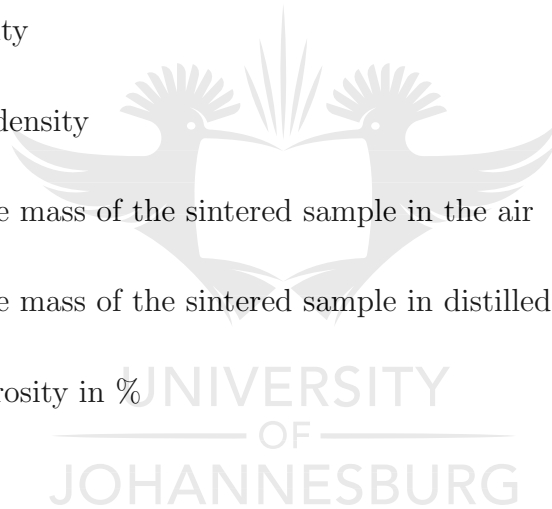
ρ_d sample density

ρ_{th} Theoretical density

B_a measured the mass of the sintered sample in the air

B_w measured the mass of the sintered sample in distilled water

P Absolute porosity in %

Contents

List of Figures

13

List of Tables

Abstract

Machine learning is a branch of artificial intelligence that uses data to build inferences, using designed models to generalize and make predictions. A novel approach was presented on using machine learning techniques in predicting the mechanical properties of welded 2507 DSS. Machine learning algorithms was used to predict the mechanical property from sintered and Nd:YAG laser welding parameters datasets. Welded sintered 2507 duplex stainless steel (DSS) alloy was developed for an automobile, specifically exhaust flanges. Before 1990's welding PM stainless steel was not practiced, until PM stainless steels was considered as a viable candidate for exhaust flanges in hot exhaust gas outlay. Further engineering application of this alloy has been encouraged through several studies performed to investigate the microstructure and properties of Laser welded 2507 DSS alloy using traditional processes. However, till date there is no thorough information on the microstructure and associated mechanical properties of Laser welded Spark plasma sintered (SPS) 2507 DSS. A study was carried out to comprehensively characterize the microstructure and examine the mechanical properties of Nd-YAG Laser welded 2507 DSS produced through SPS to generate data for the machine learning prediction analysis. Therefore this research compares the predictive power of two primary Machine learning algorithms, namely: Artificial Neural Network(ANN), and Support Vector Machine (SVM) to effectively predict the hardness at the weld metal zone, using different statistical metrics like MAE, MSE, and R^2 were used to determine the machine learning algorithm performance.

Chapter 1

Introduction

Stainless steel alloys have seen increased use of the Powder metallurgy (PM) route for its production. Popular for it's outstanding corrosion-resistant properties. Stainless steel application spans many industries, including automotive, aerospace, medical and chemical processing. Meanwhile, corrosion properties are among properties in demand for the increasing application of steel. Adequate processing and sintering of PM stainless steel are known to be an important factors necessary to achieve improved mechanical properties and chemical properties [1]. Duplex stainless steel (DSS) is characterised by dual nature of nearly equal amounts of ferrite and austenite. The austenitic and ferritic phases are responsible for the toughness and strength properties of duplex stainless steel respectively [2]. DSS occupies a unique place in the steel family, and they have found exceptional applications in chemical, oil and gas and food industry industries among others [3]. Also, DSS effectively finds application in chemical, aerospace, biomedical and power industries and other engineering fields, owing to attributed attractive properties such as good weldability, appreciable corrosion resistance, abrasion resistance, outstanding mechanical ductility, strength and corrosion resistance [4]–[6].

In conventional manufacturing, different procedures have been used to process duplex stainless steel, such as forging, extrusion, casting, and rolling. However, these manufacturing processes have been rendered complex by thermal expansion coefficients, precipitation of secondary phase and intermetallics precipitates on the

grain boundaries and the variation in the deformation behaviours of constituent phases [7]. PM creates a different outstanding different route for duplex stainless-steel production. In PM technique simple processes are made use of to produce a product that requires little machining, cost-effective, controlling the composition of the material, microstructure, optimized physical and mechanical properties can be produced by this process. Also, issues synonymous with traditional casting can be avoided by powder metallurgy, with the capability to fabricate near net shape components and semi-finished products [8]–[12]. Meanwhile, out of the different powdered metallurgical manufacturing method, spark plasma sintering (SPS) has been judged to produce a uniform dispersion of reinforcing particles with fine microstructure, producing alloy that does not agglomerate easily, improving compact strength and hardness. The spark plasma sintering process has also attracted some attention because of its attributes of short sintering time resulting from low energy consumption [13]–[16]. Also, SPS being a flexible technique, can rapidly fabricate various materials including ceramics, metals and composites [17]–[19]. In addition, SPS ensures speedy heating of powder and direct stimulation sintering [20], [21]. Components manufactured through PM process finds applications in automotive, aerospace, and defence industry. Production of heavy parts assembly through PM requires joining PM parts [22]. Welding has been one of the most successful joining techniques accepted for fastening several parts [23]. Also, Welding sintered alloys with intrinsic porosity is always an arduous endeavour; the porous property is responsible for thermal conductivity reduction, reduced hardenability and presence of impurities such as oxides [22]. Impurities locked in the pores affect the weldability of the PM part. The locked impurities eventually result in solidification cracking [24]. Welding powdered metal part is different from welding of rolled, cast, and forged parts, owing to porosity in their microstructure. The porosity characteristics is determined by several controlling factors viz; sintering, green density. Specifically, the size fraction, the morphology, and size distribution of the pores have a significant effect on the mechanical behavioural implication on components under welding

conditions. Requirements such as environmental factors, the porosity volume, and strength should be taken into cognizance when selecting the appropriate welding process to join PM parts [25]. The joining processes relevant to PM parts can be divided into a solid-state and liquid-state. Diffusion bonding and brazing, categorized under solid state process, have enjoyed dominance in usage for lower density porous parts. In contrast, higher densities or low porous part are often addressed as fully dense wrought materials. The fusion-based joining processes majorly applied in joining are: Arc welding, that is gas metal arc welding (GMAW), electron beam welding (EBW) and laser welding (LW) [24], [26]. In the work of Seluk et al.[24] on joining PM parts, were able to join low density parts using the solid-state joining method, diffusion bonding [27] and friction stir welding [28]. Parts having higher densities or low porosity can be joined by fusion joining processes namely, laser welding [29].

Dimensional and metallurgical consequences of high heat input on sintered powdered compact had necessitated joining by low heat input processes such as sinter brazing or joining and diffusion bonding [30]. It is well-known fact that metal arc welding, TIG (Tungsten inert gas welding) or MIG (Metal inert gas welding) are always associated with high heat input and requires a shorter joining time. The porosity increase and swelling arising from the evaporation, high oxide formation, low thermal expansion coefficient of the powder resulting in post weld cracks, and brittle phases formation usually have negative effect on the resulting joint. Wahba et al. [31] and J Hamil [26] reported that sintered steels are successfully welded by tungsten arc welding (GTAW/TIG), friction resistance welding (FRW), and laser beam welding (LBW). Therefore, success in welding PM parts requires adequate knowledge of the effect of porosity, impurity level, overall cleanliness, and chemical composition upon weldments properties such as the heat- affected zone cracking and weld metal, ductility, distortion, residual stress, and toughness.

It has been made known that the most exciting tool that was recently added to the materials science toolbox are machine learning (ML) [32], a branch of artificial

intelligence(AI) deals with model creation that can learn from the situation of the past data [33]. In recent times, machine learning algorithms have seen applications in image classification, clustering, regression [34]. ML has been applied within materials science research, including examples for materials properties predictions, using past historical data [35]–[37].

1.1 Motivation for the research

It has become crucial and necessary to quickly and accurately predicts the properties of materials. Applying machine learning model to efficiently model material properties is a new yet promising research area. Therefore this research finds its root within this context. Also, since the material considered is a sintered material, understanding the industrial application of sintered parts and its joining mechanism will be worthy of consideration. Laser welding is considered for this operation, known for its low heat input, reducing the thermal effect on the welded metal. The governing motivation for this research is to have an improved understanding on the application of machine learning algorithms to predict some of the mechanical properties of the welded alloy.

1.2 Problem statement

The use of ML algorithms in predicting mechanical properties of micro-alloyed steels has always been a tedious task that needs a thorough understanding of the processing parameters [38]. Rolled or cast part welding is different from PM metal parts welding, owing to the porous nature of the PM metal. The volume of porosity significantly affects the welding process characteristics [39], [40]. Thermal and metallurgical processes resulting from porosity continues to make PM joining an arduous task [23]. Therefore, pores in the sintered components, act as thermal insulators, slowing down thermal conductivity, heat transfer, and cooling rates,eventually resulting in excessive shrinkage and grain growth.

Due to the factors mentioned above, the following will be an exciting problem to be considered for optimization.

The problem statement will thus be formulated as follows:

- Presentation of machine learning algorithms to optimally predicts materials properties will be considered.

- Optimized parameters that will produce sintered samples with reduced porosity will be worked towards.

1.3 Research Questions

- Machine Learning Prediction

    1. Can ML algorithms be used to predict the vickers hardness properties of the weld zone(WZ) using the process parameters like welding speed, heat input, sintering temperature, and sintering time as input parameters?

- Experimental

    1. Is laser fusion welding of SPS 2507DSS feasible?

    2. Does heat input of Nd:YAG Laser-welding affects the mechanical properties of the weld?

    3. How will the heat input affects grain growth within the melt pool, and can grain growth be controlled?

    4. How can porosity in a laser welded 2507 DSS be examined?

1.4 Research Objectives or Hypotheses

This research will be initiated to systematically and comprehensively study the possibilities of using a machine learning algorithm to predict hardness at the WZ and also the influence of Nd:YAG laser welding process on sintered 2507 DSS. Specifically, it is of interest to:

- Study the prospects of using laser welding to join spark plasma sintered DSS.

- Understand the influence of impurity level, porosity and chemical composition upon the weld metal.

- Investigate the microstructural changes and how it affects the mechanical and microstructural properties of the welded material.

- Study the prospects of using ANN and SVM machine learning model to predict the hardness at the WZ of laser welding to join spark plasma sintered DSS.

1.4.1   Hypotheses

- The hardness at the WZ can be predicted as a function of the process parameters like welding speed, heat input, sintering temperature, and sintering time as input parameters

- The hardness of the WZ can be estimated with an acceptable level of accuracy using ML models

1.5   Research Approach

The various tasks essential to achieve the sets objectives are highlighted below:

- The as-received 2507 DSS powder is first characterized using X-ray diffraction (XRD) and scanning electron microscopy (SEM).

- 2507 DSS powder is sintered with SPS equipment at different sintering parameters. This process is necessary to produce a solid compacts products for the welding operation.

- A comprehensive microstructural characterization of the sintered metal is carried out before proceeding with the welding operation.

- Nd:YAG laser Welding operation is carried out at different parameters.

- Mechanical analysis is carried out on the different weld zones, including micro hardness test and nanohardness test.

- A microstructural analysis is carried out on the weld by SEM, and electron backscattered diffraction (EBSD)

- The porosity in the weld is analysed by X-ray computed tomography (XCT).

- Statistical data analysis implemented in Google Tensor was carried on the data to calculate the statistical significance of sintering and laser welding parameters on the Vickers hardness of the WZ.

- Implementation of algorithms, metrics, and optimization of the ML approaches to predict the mechanical properties of WM of the laser welded DSS alloy. It is worthy to note the ML is Iterative. Furthermore, during the iterative process, methods and algorithms will be used and optimized to achieve possible results. The results will be critically evaluated and compared with one another. The limitations imposed by the data will be pointed out, and recommendations for further developments on the studies.

1.6   Thesis organization

- **Chapter 1** Introduction gives the background information on the research work, research objectives, research approach.

- **Chapter 2** Literature review consist of two sections. The first section gives a detailed review DSS and the welding metallurgy of laser welding of DSS. The second section handles the review on data analysis and Machine Learning and its application to materials properties prediction.

- **Chapter 3** A detailed description of the experimental methods, equipment used for the research is provided. Details on SPS of 2507 DSS, Nd:YAG laser welding, porosity analysis, post-weld heat treatment, data analysis, and machine learning modelling.

- **Chapter 4** Presented in 4 parts. The first part presents the microstructural analysis of the as-received 2507 DSS powder, sintered 2507 DSS, XRD characterization of the phases present in the sintered alloy at different sintering parameters. The second parts discuss Nd:YAG welding operation for the sintered alloy, with the microstructural characterization of the phases presents.The porosity of the welded alloy was also carried out. In addition, the effect of post-weld heat treatment on the microstructure of the 2507 DSS is discussed. The third parts discussed the data and statistical analysis of various processing parameters used in the research and their statistical significance to the mechanical properties. The effect of different ML algorithms in the predictions of mechanical properties was discussed.

- **Chapter 5** Conclusion and potential future work.

Chapter 2

Literature Review

This PhD research focuses on Nd:YAG laser welding of 2507 DSS alloy, its characterization and machine learning modelling of the mechanical properties. A brief introduction to the relevant subjects is essential before presenting our research. Therefore, this chapter starts with the introduction to stainless steels, metallurgy of stainless steel, microstructure of duplex stainless steel, Powder metallurgy, welding of PM stainless steel, applications of sintered steels, laser welding. Also, application of data science to materials science, machine learning application in predictions of material properties was considered.

2.1 Stainless steel: Metallurgy and alloy composition

Stainless steel can be described as an alloy that belongs to the ferrous metal family. They usually have outstanding corrosion resistance. Alloying elements that are highly essential in different stainless steel grades includes, molybdenum, carbon, Nickel, carbon , silicon, manganese, titanium, sulfur and niobium. It is also a known fact that PM stainless steels have been processed from some of the wrought stainless steels grades. Therefore, PM stainless steel has similar characteristics as their wrought counterparts [1]. For steels to be stainless, it has to have at least

11wt% of chromium as an alloy. Stainless steel performs better than ordinary steel when subjected to load at high temperature [41].

2.1.1 Metallurgy of stainless steel

Having a sound understanding of stainless steel is necessary to understand understand the PM stainless steels classification better. Stainless steels can be categorized into five types, microstructure, viz; austenite, ferrite, martensite, and duplex stainless steel. The last is precipitation hardened stainless steel, differentiated by its strengthening mechanism. Structurally, the body-centred cubic (ferritic) structure represents pure iron that exists at room temperature. At thesame time, it transforms to face centered cubic (fcc) (austenite) know as gamma phase (γ) when heated above 910°C, when further heated through 1400°C, it transforms back to ferritic structure. Alpha ferrite (α) stands for the lower temperature formed ferrite, while the phase formed at higher temperature is known as delta ferrite (δ) [42]. Figure 2.1 further explained the different microstructures observable at different temperatures.

Alloying of iron or an iron-chromium alloy with Nickel encourages ferrite transformation to austenite, resulting in the expansion of both γ-phase region and $\alpha+$ γ region. While, chromium is known to be the ferrite forming element. The overall effect of all the ferritizing and austenitizing elements gives us the idea of which phases to be expected in the alloy at room temperature. This type of prediction can be explained by Schaeffler diagram [43].

2.1.2 Duplex stainless steel

A Duplex stainless steel(DSS) can be seen as an alternative to austenitic stainless steel for several industrial applications, such as oil and gas, chemical and automobile. The combination of ferrite and austenite phase provides a good combination of corrosion resistance and improved tensile strength. The austenite phase impacts ductility and general corrosion resistance, while the ferritic phase provides improved strength and local corrosion resistance, eventually combining the attributes of both
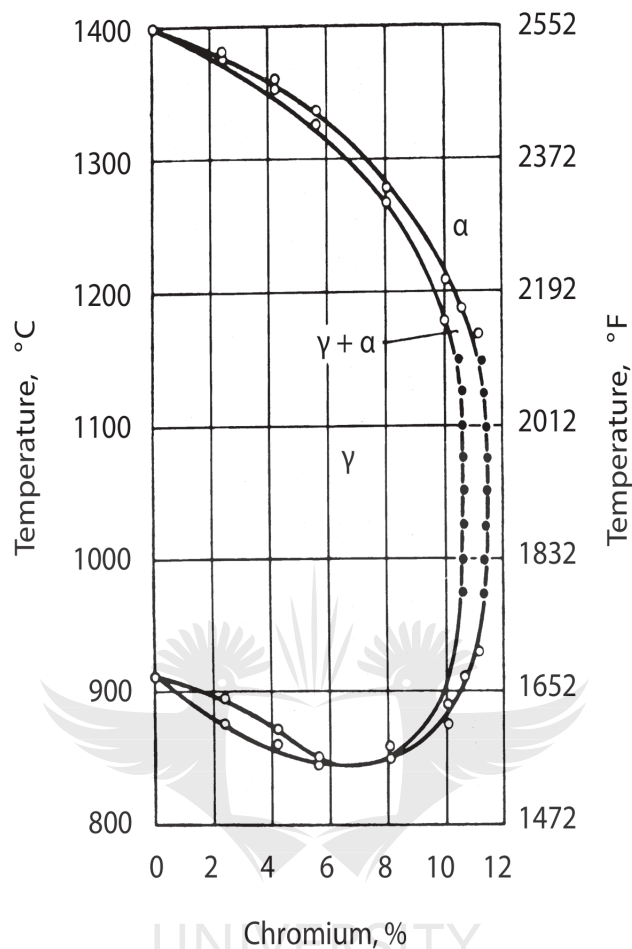
Figure 2.1: Iron-chromium partial phase diagram showing the gamma loop for a 0.004% C- and 0.002% N containing alloy [42].

micro-constituents. [44]. Although, elements like Cr and Mo provide outstanding localized corrosion resistance, they usually lose their corrosion resistance and ductility properties during welding process, requiring post-weld heat treatment to regain the lost properties. Nitrogen as an alloy element is known to reduce the chromium partition between ferrite and austenite phases. This alloy element increases crevice and pitting corrosion resistance of the austenite phase for the second generation DSS grade (SAF2205). The quest for ferrite and austenite balance for best performance led to the discovery of the third generation duplex grades (SAF2507). 2507 DSS
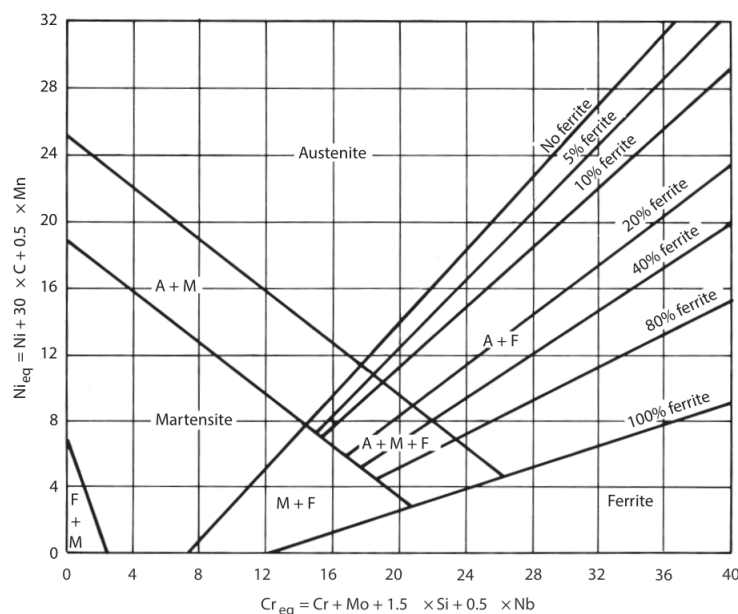
Figure 2.2: Schaeffler diagram for determining phases formed upon solidification, based on chemistry [43].

grade corrosion resistance is boosted with respect to the PREN (Pitting Resistance Equipment Number). The PREN represents an empirical formular for predicting duplex and austenite stainless steel pitting corrosion [45].

PREN=%Cr+ 3.3(%Mo + 0.5%W) + 16%N (>40 for super duplex stainless steels). SAF 2507 is designed designed for a highly corrosive chloride environment, with excellent stress corrosion resistance, crevice and pitting corrosion resistance. Also, it shows high good weldability and high mechanical strength [46]

2.2   Microstructure of Duplex stainless steel

DSS is characterized by a two-phase structure, consisting of 50% BCC ferrite grains and FCC austenite grains [48]. Figure 2.4 shows a schematic section of the Fe-Cr-Ni diagram at the 70%Fe level [49]. The compositions and the phase proportions representation for different alloy is indicated in figure 2.1, which was annealed. The duplex structure was stable at high temperature, mostly due to the nitrogen content's stability effect, than by Mo, or Cr. Usually, in the annealed condition, wrought DSS contain about 40-50% austenite within the ferrite phase, after solidification, δ
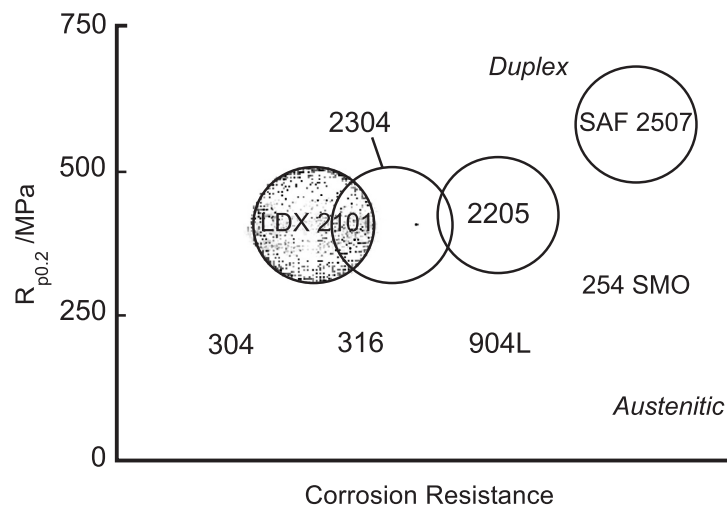
Figure 2.3: Comparison of duplex stainless steels and austenitic stainless steels [47]

ferrite is formed first. Depending on the composition of DSS, different amount of austenite is formed as the last phase. Meanwhile, if the alloy is subjected to subsequent annealing, additional austenite will be formed by solid-phase transformation. [50], [51].

Other phases that can be identified in DSS includes σ, χ, R, $\alpha^{'}$, carbides, and nitrides. These phases are usually studied using heat treatments [52]

2.3   Powder metallurgy

Powder metallurgy (PM) can be defined as a production process to consolidate fine particles to solid materials. The most crucial advantage of PM process over other manufacturing processes lies with the efficient use of material, among other advantages that includes the production of diverse shapes and the reduction of steps involved in the production process [54]. Corrosion-resistant alloys are in recent time produced by PM process. Application of PM stainless steel alloy spans through various of industries, including, automotive, medical, and chemical processing equipment [1].
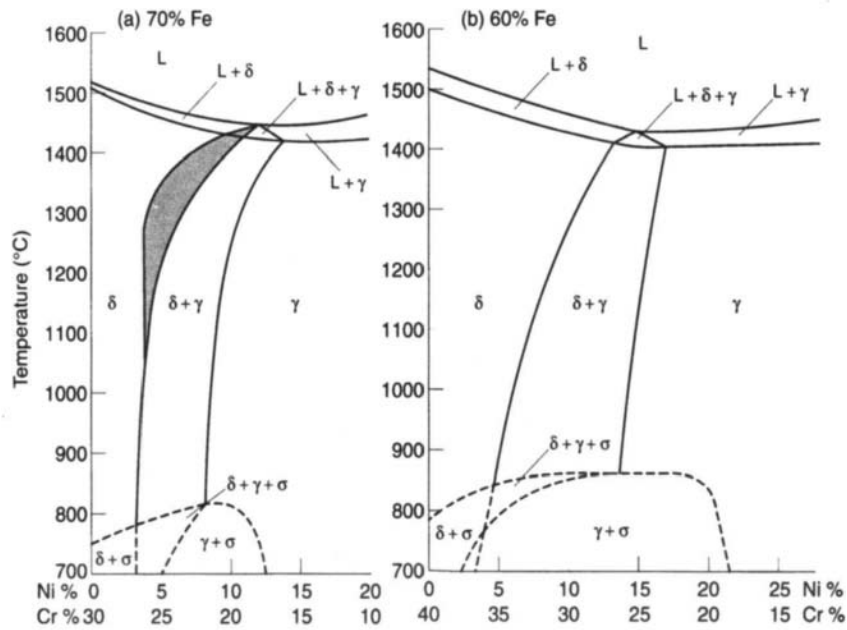
Figure 2.4: Concentration profiles in the ternary Fe-Cr-Ni constitution diagram at 70% and 60%Fe. The schematic effect of nitrogen additions references [49], [53].

2.3.1 Sintering

Sintering is a process used to consolidate loose aggregate of powder with the desired composition, usually under controlled time and temperature conditions [55]. The process has been used for various materials, such as non-metals, metals, polymers, ceramics, and their alloys. A broad group of technologies is employed to obtain different products such as luminescent films and iron ore agglomerate. Many novel sintering methods have been discovered over time, which includes, electric current assisted sintering, laser sintering, microwave sintering, and spark plasma sintering. The technology behind sintering intends to minimize energy used during sintering, and produces materials with exact intended properties [56]. Figure 2.5, shows sintered parts fabrication pattern. Several processing variables and various techniques are involved in sintering steps that eventually leads to the variations in the sintered properties and microstructure. Sintering process aims to design microstructure through sintering variables control. In the process of the microstructure control, the sintered density, grain size, pores distribution, size, and phases distribution plays a vital role in the overall properties of the sintered alloy[57].
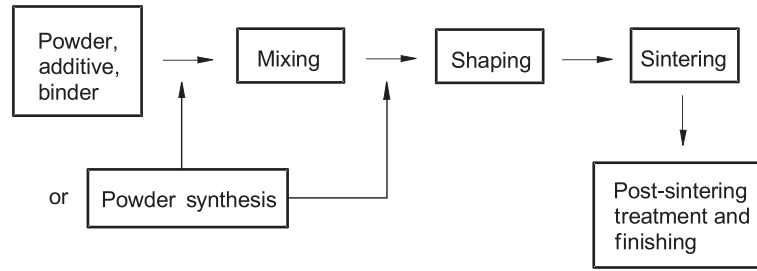
Figure 2.5: Fabrication pattern for sintered parts. [57].

2.3.2 Basic Phenomena and driving force of Sintering

The major driving force of sintering is total interfacial energy reduction. The interfacial energy of a powder compact is expressed as γA, A stands for the total interface surface area of the compact and γ is the specific surface interface energy. The total energy reduction can be expressed as;

$$\Delta(\gamma A) = \Delta\gamma A + \gamma\Delta A \tag{2.1}$$

The interfacial energy changes ($\Delta\gamma$) is caused by change in interfacial area and densification owing to grain coarsening, Figure 2.6 shows the total interfacial energy reduction that occurs through grain growth and densification, which is the foundation of sintering [57].

2.3.3 Effect of Powder Particle Size on the Grain Size of the Sintered Material

Over the years sintered materials produced by PM have been known to possess unique properties different from their counterparts made by conventional manufacturing methods. There has been little attention on the grain structure of sintered materials, and it is a known fact that the grain structure in a PM alloy is smaller than cast alloy that was subjected to the same heat treatment. Meanwhile, several factors responsible for the grain size in a sintered metal include sintering time, sintering temperature, compacting pressure, size, shape, and the surface powder
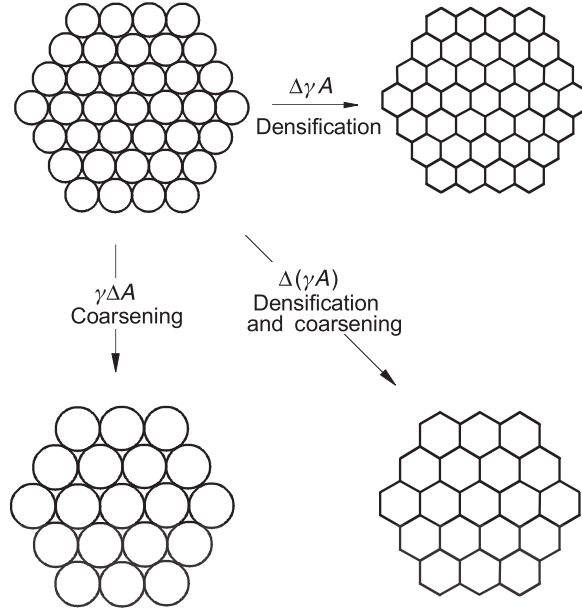
Figure 2.6: Phenomena occurring during sintering under the driving force for sintering. [57].

particle condition [58]. The famous equation for grain growth in solid metal are not applicable to powder compacts grain growth during sintering. Isothermal grain growth occurs, and the the grain diameter D can be denoted by

$$D = Kt^n \tag{2.2}$$

where K and n is the constant at constant temperature and t=time of heating. K can be defined by the Arrhenius relation.

$$K = Ae^{-H}/RT \tag{2.3}$$

Hausner and King [58] performed a test to study the effect of powder particle size on grain size of sintered products. It was noticed that the finer particles usually contained smaller grains that had larger particle size. They concluded from their observations that the grain size of the compact might not necessarily be affected by the density of the sintered compact, at the later stage of sintering. Spheroidization of pores usually occur progressively, which eventually leads to grain growth. It was

also discovered that compacts prepared from fine powders particles contains small pores that spheroidize faster than the coarse particle.

2.4 Welding PM stainless steel

PM stainless steel welding was considered to a great extent because of its application as a steel exhaust gas outlet (HEGO) bosses in the early 1990s. Meanwhile, there is dearth of published work addressing the welding of PM stainless steel. Recently, researchers started working on the welding of PM stainless steels. It was noticed in their research, that the metallurgical underlying principles governing the welding of wrought stainless steel is applies to PM stainless steel. In welding PM alloy, additional consideration should be given to the porosity nature of the alloy. [1].

2.4.1 Welding PM stainless steel basics

Different groups of stainless steels usually have diverse weldability considerations. Majorly determined by the modes of phase transformation that transpire during the solidification process. The weld metal's final composition should be such that resistance to corrosion is not undermined. High ferrite content affects corrosion resistance because pitting corrosion is preferentially located at δ-ferrite phase. Collins and Williams [59] have been able to determine that the tendency for pitting measured by ASTM G 150) precipitously increase when ferrite content exceeds 3.5%, corresponding to Cr_eq / Cr_eq ratio of 1.55 in their study. Welding of low carbon steel and alloy steels requires a meticulous managements of heat input due to the relatively poor thermal diffusivity and their significant coefficient of thermal expansion. The term weldability means the ease at which a sound weld can be achieved and also satisfactorily offering good performance in service. Therefore, it is important that our resulting weld should exhibit good performance in terms of mechanical strength, resistance to corrosion, impact strength, and ductility [1].

2.5 Applications of Sintered Steels

Corrosion resistance had become the major impediment to the industrial application of sintered duplex stainless steel from 1970s to approximately 1990. Corrosion properties have been the major consideration for using sintered steels, just like the case of cast and wrought stainless steel. The following areas have enjoyed the application of PM stainless steel because of the corrosion improvement, like; exhaust system flanges, antilock brake system sensor rings, and oxygen sensor bosses. The major market distribution of sintered stainless steel has prevalently shifted to automotive. As shown in figure 2.7, sintered stainless steel served many market segments, including the automotive industry [60].
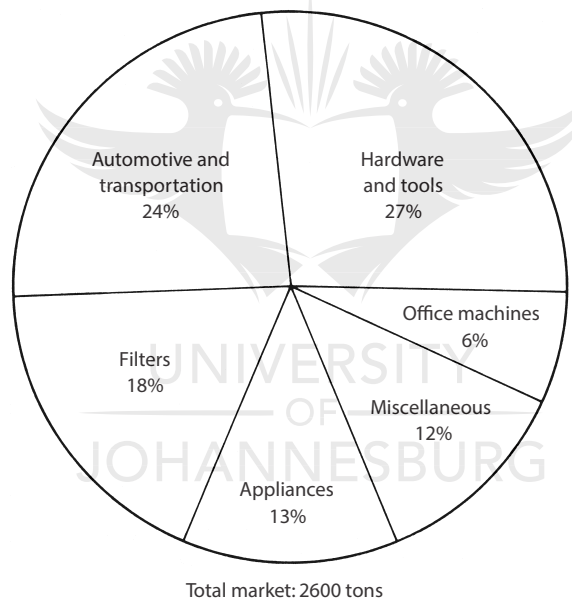
Figure 2.7: Market distribution of powder metallurgy stainless steel products in 1979 for United states [60].

2.6 Laser Welding

Laser welding has seen popularity within the automotive industry and other industries such as, medical, aerospace and construction industries. Laser welding has been found worthy of production speed, quality assurance, final properties, and robustness [61]. However, laser welding also comes with some drawbacks such as maintenance,

poor bridging gap, especially for duplex stainless steel, high cost of equipment, and high cooling rate due to the lower heat input, resulting in excessive ferrite formation [45]. Laser is an abbreviation of Light Amplification by Stimulated Emission of Radiation. The rise of laser welding started in 1971, when the first keyhole effect from the multi-kilowatt CO_2 laser sources has also seen more growth through understanding of the know-how on laser technology [62]. CO_2-Laser was the leading industrial high power laser used from the beginning, before the emergence of Nd:YAG. Meanwhile, Nd:YAG is characterized with 10 times shorter wavelength beam guidance by optical fibres with an advantage of high absorption in metals [63].

2.6.1 Laser Welding mechanisms

Laser welding can be described as a fusion welding, i.e the process that uses heat to join two or more materials together by heating to melting point. Laser welding can be carried out by two mechanisms, viz [64]; (1) conduction welding, where the laser usually acts a the point source of energy. Usually, welds produced by this method are roughly semi-circular in cross section. (2) Keyhole welding , the laser usually acts as the concentrated heat source that penetrates completely or partially through a workpiece, forming a keyhole. The welds produced in this case is usually deep and narrow. The two mechanisms are pictorially shown in Figure 2.8.
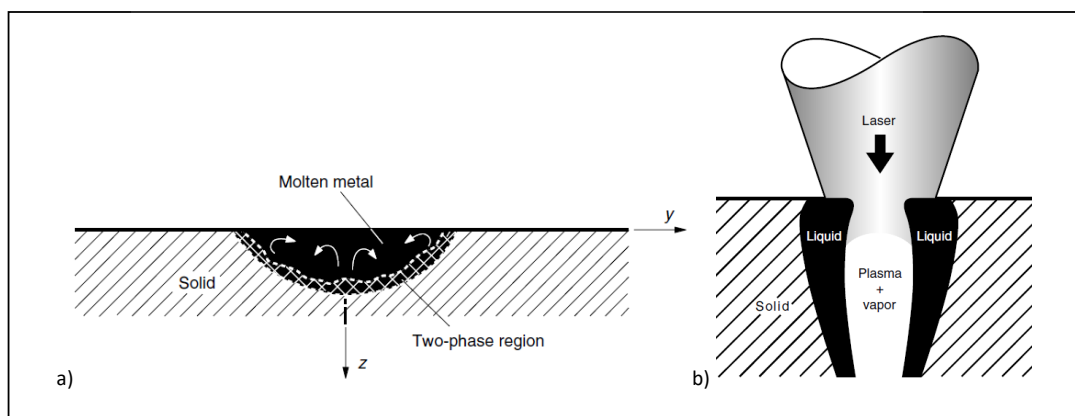
Figure 2.8: (a) Schematic representation of conduction and (b) keyhole mode welding. [65].

Conduction mode welding

Conduction mode welding usually occur whenever the heat input is very low, yielding a semi-spherical shape of the weld, with lower penetration characteristics, poor welding efficiency, and high heat losses [66]. The boiling point of the welding materials is usually higher than the peak temperature of conduction mode, when the heat conduction is from the surface [67]. The stability laser welding brings to the weld pools qualifies laser welding for welding thin materials. This welding method has found application in the automotive, aerospace, and electronics industries [68].

Keyhole mode welding

In this type of welding mode, the weld geometry is dependent on the laser power density and focal size of the laser beam. Keyhole mode welding is known for its high density, high penetration, high accuracy, low heat input, high penetration, and high welding speed [69]. The keyhole mode welding can be divided into two parts: near the parallel-sided area, semi-circular shape at the top of the weld [70].

2.6.2   Laser Welding systems

Differen laser welding systems are applied in the industries. They include: CO_2 and Nd:YAG lasers.

CO_2 Laser

It usually operates at a wavelength of 10.6µm with a power ranging from 1.5-6kW. Generally characterized with low energy absorption of the laser beam by the metal, having overall efficiency of up to 15%, even though the energy transfer efficiency between the work-piece and the laser beam may be up to 0.8 [71]. This type of laser is usually applied to weld sheet metal at high weld speeds [72], [73].

Nd:YAG laser

Neodymium-doped yttrium aluminium garnet (Nd:YAG) laser has a wavelength of 10.64µm and has been chiefly employed to investigate the weldability of various alloys [74]. Pulsed Nd:YAG laser welding has mostly attracted attention in academic's research and industry recently [75]–[79]. Nd:YAG laser is known to have various advantages over CO_2 Laser, such as high-energy absorption rate as a result of its low reflectivity, low residual stress and high welding speed [80]

2.6.3 Laser welding process parameters

Laser parameters can go a long way in determining the weld quality, such as microstructure of the fusion and HAZs, weld geometry, defects formation e.t.c [66], [81]. Selection of the appropriate processing parameters and understanding their interaction is essential in obtaining outstanding results in laser welding [82]. Important process parameters necessary for laser welding of metallic alloy will be discussed in the following section.

Laser power

Conventional laser power employed in the automotive industry is usually around 4-10kW. Meanwhile, high power will result in an excessive melt and solidification of metal at the root of the weld, i.e. welds dropout. The required laser power is always dependent on the materials, welding speed, and the thickness of the material [83]. As shown in Figure 2.9 below. The laser power delivery method can be divided into two modes: pulse wave(PW) mode and continuous wave (CW) mode. Working with the two modes usually results in different results. The laser power in CW laser welding process should be increased whenever the welding speed is increased in direct proportionality with a given thickness of the welding materials. For a laser system with high density, a high welding speed can be achieved by using high laser power [66].

In Figure 2.9(a), laser is kept constant over the whole welding duration. The
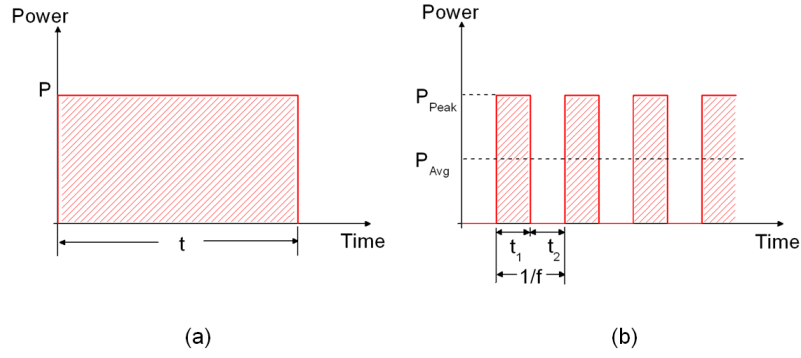
Figure 2.9: Schematic of laser power delivery methods: (a) the continuous wave mode; (b) the pulsed wave mode [84].

energy of continuous-wave laser welding is usually defined as equation 2.4

$$E = P \times t \tag{2.4}$$

In the equation E, P, and t represents the laser energy(J), laser power(W) and the welding duration(s), respectively. While, in pulsed wave laser welding, the quality of the weld is determined by the peak laser power P_{peak}, laser frequency, laser beam diameter, and welding speed. The pulse energy can be defined by equations 2.5 to 2.7, where pulse frequency (f), energy(E), average power (P_{Avg})

Pulse energy:

$$E = P_{peak} \times t_1 \tag{2.5}$$

Duty cycle:

$$f = \frac{t_1}{t_1 + t_2} \tag{2.6}$$

Where t_1 and t_2 are the duration of laser beam on and off respectively.

Average power:

$$P_{Avg} = E \times f \tag{2.7}$$

Welding speed

Welding speed is the speed at which the welding process travels. The laser power[kW] and welding speed [mm/s] determines the heat input [kJ/mm], as depicted by equa-

tion 2.8. [85].

$$Heat input(Q) = \frac{Laser Power(P)}{travel speed(v)} \qquad (2.8)$$

As the weld speed varies the weld pool size and shape changes. The weld pool width increases with lower speed and increases in the dropout, while with higher speed, it causes the weld pool to have difficulty redistributing to form a smooth joint. High welding speed can also lead to undercut in the weld [83]. Also, high welding speed can cause higher angular distortion and lower local deformations [86].

Focusing position

The penetration depth and the local weld shape are determined by the focal position relative to the sheet surface. Insights from various researches have shown the effect of focal length and beam diameter resulting in approximately 1mm below the sheet surface for thin sheet welding [85], [87]

2.6.4 Microstructure of laser beam welds

Welding is a metallurgical process, while the weld quality is usually affected by the physical, thermal, chemical and mechanical properties of the welding materials being welded [84]. Due to the low heat input of laser welding, the material melts for a short time, solidifying very fast, differentiating the microstructure of laser-welded material form other conventional welding methods. Two different regions are visible from a keyhole weld: a fusion zone (FZ) and Heat affected zone(HAZ). In the FZ, the metal, first crystallizes between the solid-liquid interface, which grows rapidly into the inner part of the molten zone. The HAZ can be divided into sub-zones, which represents different types of microstructure. These zones are determined by the nature of the material being welded. Intermetallics brittle phases can result from non-equilibrium phase transformation. Figure 2.10 below presents the case for the structural steel [88].

The fusion zone (FZ)

The peak temperature at the FZ is mostly higher than the melting point of the welded materials for solidification to occur. As the temperature of the welded materials reaches liquid temperature, there will be a loss of alloying elements which will eventually results in the variations of the microstructure and mechanical properties of the weld. Usually, the solidification rate controls the grain size and shape, and also the defects and inclusions distributions, when the fusion zone undergoes a transformation from the liquid phase to a solid phase. Therefore, the microstructure obtained at the FZ resembles the growth rate, cooling rate, temperature gradient and alloy composition of the weld material [89].

The heat-affected zone (HAZ)

In laser welding, the HAZ temperature is usually lower than the material melting point. The heat at the HAZ is enough to cause phase transformation without noticeable melting occurring. The degree of grain growth, microstructure, composition gradients, residual stresses and phase transformation are influenced by the thermal cycle and temperature gradient in the HAZ. Meanwhile, cooling rapidly can reduce grain growth, thereby producing a finer microstructure [90].

2.6.5 Laser weld defects

The heating and cooling rates during the laser welding process can affect the variations in microstructure, composition and residual stresses at the FZ and HAZ [89]. These microstructural and composition changes can lead defects that can eventually mar the weld integrity [92]. The weld's mechanical and chemical properties can be impaired due to phase transformations resulting in porosity, cracking and loss of weld element and oxidation within the weld [93].
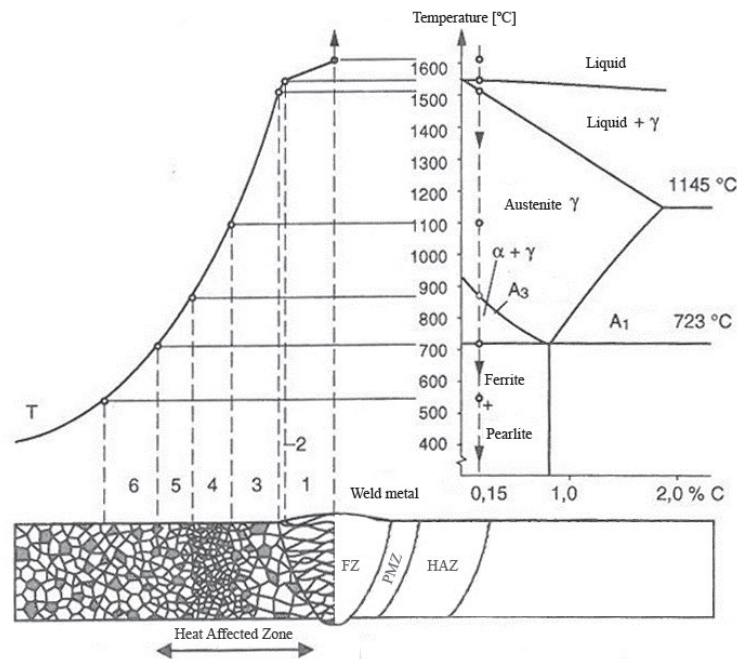
Figure 2.10: A schematic presentation of different regions in the welded joint. [91].

Porosity and cavity

Instabilities within the keyhole usually lead to pores in the weld. The porosity in the weld is usually enhanced by oxides contamination that vaporized, thereby creating gas bubbles that are trapped within the melt solidification. Cavities occur when large pores merge together and form at the interface between welded sheets, with high amount of oxide contamination [94]. Porosity is one of the insidious defects that occur in the weld metal, especially in light metallic alloys. Porosity can lower the mechanical properties of the weld and result in fracture. The keyhole collapse because of the presence of bubbles in the weld [95].

Solidification cracking

In steels, parent steel chemical composition usually have an effect on crack susceptibility. Elements such as phosphorus and sulphur can produce solidification cracking in the weld [96]. However, if manganese is locked up in sulphur, it prevents solidification cracking. Mostly weld profile shape usually causes solidification cracking in the thick section of laser-welded steel. Midsection bugling in the cross-section of

weld can increase solidification cracking susceptibility. Therefore, the weld profile must be carefully controlled when carrying out laser welding [97].

2.7 Machine learning

Machine learning (ML) is known as a branch of Artificial intelligence(AI). ML deals with computer learning from existing data without being explicitly programmed and makes predictions from new data by building a model from the input samples [98]. Machine learning can also be described as a statistical framework that can be used to automates data analysis model fitting for data-driven predictions. Correlations and insights between different types of data can be extracted from ML models [99]. The main idea behind ML is to use features associated with an algorithm and fit it to a target. The features can be said to represents phenomenon of individuals measurable properties being observed [100]. Creating a machine learning model usually requires great mastery and computational efficiency. In this research, a data-driven computational approach will be used by employing some popular machine learning algorithms. Data driven models are usually known to operate in reverse. Meanwhile, ML algorithms are essential to the process needed to execute a data-driven modeling. Before, most programmers use to pass instructions to computers step by step using algorithms. However, with the inception of machine learning, algorithms can learn on the data provided by extracting knowledge from the data provided. In the 1950s Alan Turing made a proposition of eponymous concept, the concept centres on artificial intelligence, which claims a computer learn when humans interact with it. He went further to state that there is no difference between human-computer and human-human interactions [101]. ML systems can be classified into four distinct categories: unsupervised, supervised, semi-supervised and reinforcement learning algorithms [101], [102].

Supervised algorithms

Supervised learning deals with machine learning algorithms learning from data collected from known input values x and measure value y, gotten through observation or experimentation. Using this data, a function f is defined for the prediction of output values from arbitrary input. Continuous variable output is predicted by a regression algorithm, while for output with discrete values, classification algorithms can be used [33]. The examples listed below are types of supervised learning algorithms [102]:

- k-Nearest Neighbors

- Linear Regression

- Neural networks

- Support Vector Machines (SVMs)

- k-Nearest Neighbors

Unsupervised Learning Algorithms

In unsupervised learning, the training data is not labeled. The system learns without being thought. Unsupervised algorithms finds relationships between input variables rather than finding relationship between input and output data [103]. Listed below are examples of popular unsupervised learning algorithms [102]:

1. Clustering

   - Density-based spatial clustering of applications with noise (DBSCAN)

   - K-Means

   - Hierarchical Cluster Analysis (HCA)

2. Anomaly detection and novelty detection

   - Isolation Forest

   - One-class SVM

Semi-supervised learning

Semi-supervised learning refers to algorithms dealing with partially labeled training data, and fewer labeled data [102]. Semi- supervised learning can address most of the problems associated with labelled instance such as time- consuming, capital intensive to obtain and unlabeled data, having an advantage of easy collection, but there have been a few ways to use them. Semi-supervised addresses these problems by using a large amount of labeled and unlabeled data to create a superior classifier [104]

Reinforcement Learning

Reinforcement learning algorithms update the learned model everytime new data is feed into the algorithm. To improve predictions, a feedback mechanism helps the algorithm to update itself on all every new datum [105].

2.7.1 Machine learning application to materials science

The key to the successful application of machine learning algorithms in materials problem is the appropriate selection of the right ML algorithm, as it dictates the efficiency and generalization ability [100]. In classification, regression and high-dimensional data, machine learning has shown good applicability. It has also helped to gained insights from data by learning from previous computations to produce repeatable, reliable decisions and results.The structure-property-performance relationship has always been an important concept in the materials science field [106]. Hence, the efficient control of processing conditions of materials like compositions and structural properties is necessary to produce materials with the required properties and service performance, which is the first step towards material design. Data mining usually helps to reveal hidden relationships between a large amount of material's process conditions, parameters, in relation with materials dependent properties. It is known that machine learning has disrupted the way materials can be developed [107].

2.7.2 Material properties prediction

Designing materials requires a proper understanding of how desired properties such as toughness, ultimate strength, hardness, fracture strength, and fatigue life are affected by intrinsic properties; chemical composition, microstructure, and external processing conditions. Most of these conditions can be mathematically classified as dependent and independent variables. ML algorithm can quantitatively relate dependent and independent variables to make predictions with trained data [107]. Many researchers have applied different machine learning algorithms to predicts materials properties. Tanusree et al. [108] have used Artificial Neural Network (ANN) optimized by Genetic Algorithm (GA) in designing a dual-phase steels with improved performance. They optimized and modelled six different mechanical properties to enhance the strength and ductility simultaneously. Also, Hasam et al.[109] applied ANN with back propagation algorithm and feed-forward topology to predict the chemical composition and tensile parameters on HAZ hardness in X70 pipeline steels. They were able to get a good approximation performance with R value of 0.86 and a mean relative error of 0.74%, showing an outstanding agreement between predicted hardness and the experimental data.

2.7.3 Materials for informatics workflow

The materials informatics methods can be outlined into four steps process as shown in Figure 2.11. The first step is sufficient data collection from a particular material. The next step will be to divide the datasets into test and training datasets for the model, after which the desired inputs and outputs are defined for the model, subjected to data cleaning to ensure there is no duplication of data, followed by normalization. Lastly, an appropriate machine learning model will be selected, depending on the targeted application. Most of the time, machine learning algorithm are selected based on some attributes like, training speed, predictive accuracy, and differentiability [110].
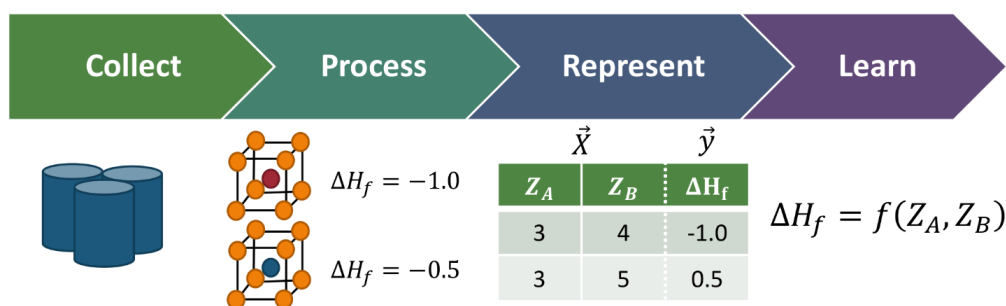
Figure 2.11: Schematic of the workflow for materials informatics. [110].

2.7.4   Features of machine learning

Usually, correlations are built between input and output variables using machine learning algorithms.The learning algorithms are also able to predict results from new unseen input data. Machine learning problems can be solved through two widely used techniques: classification, and regression, classification refers to predictive modeling problem where a class label is predicted for a given input data, while regression predicts values of some variables. Training machine learning model refers to providing algorithm with training data to learn from the training usually includes input and output variables. A training example, having a pair of input and output variables (x_i, y_i), x_i is the input variable, while y_i is the target variable that should be predicted [111].

2.8   Applicable machine learning algorithms

2.8.1   Neural network

An artificial neural network(ANN) is an ML algorithm that can process input with its interconnected neurons and learn by trial and error. ANN can be defined as a regression analysis method, which fitted non-linear function with experimental data[112]. ANN mimics a simplified brain-function model. The human brain cell is known to consists of billions of interconnected neurons. The cells have specialized members that transmit information from a particular neuron to another neuron [113].

The Perceptron

The Neural networks consist of a basic building blocks known as the perceptron. Figure 2.12b shows the smallest neural network possible, with a single layer perceptron. The equation below shows inputs $\mathbf{x}$ is created as:

$$a(\mathbf{x}, \mathbf{w}, \mathbf{b}) = \sum_{i=1}^{4}(w_i x_i + b_i) \tag{2.9}$$

Where $\mathbf{w}$ is the weights matrix, $\mathbf{x}$ is the input data, $\mathbf{b}$ is a bias that defines the activation function, $a(x)$, which stands for the linear classifier of the input data. However, for non-linear function, the activation function $f(x)$ must be expressed in a way that the output of the neuron $h(x)$ will be:

$$h(x) = f(a(\mathbf{x}, \mathbf{w}, \mathbf{b})) \tag{2.10}$$

Activation functions that are mostly used in an Artificial neural network are usually rectified linear unit (ReLu), sigmoid function, hyperbolic tangent (tanh) functions, and sigmoid as shown in Figure 2.12b. Single layer output can be represented as:

$$y(\mathbf{x}, \mathbf{w}, \mathbf{b}) = \begin{cases} 1, & \text{if } h(x) > 0. & (2.11) \\ 0, & \text{otherwise.} & (2.12) \end{cases}$$

The process can be described as sending information through a forward propagation network. Supervised learning is used to optimized the biases $\mathbf{b}$ and weights $\mathbf{w}$ using backpropagation, while the loss function is minimized using gradient descent algorithm. The "cost" associated with a difference between predicted output and true labels can be represented by the loss function, which is usually the mean square error function for a regression problem, while for classification problem it is cross entropy error. The weights are updated using backpropagated gradients, a series of iterations known as steps are used to train the network. An "epoch" represents the number passes of the entire training datasets the machine learning algorithm com-

pleted after backpropagation gradients of network for weights optimization. Figure 2.12 shows perceptron stacked in layers that can be constructed in deep architectures. The input layer/data is represented with four nodes. While, the middle layer is the hidden layer having one unit. The output layer has one unit. Meanwhile, to build a complex neural network, the number of layers can be varied [114].
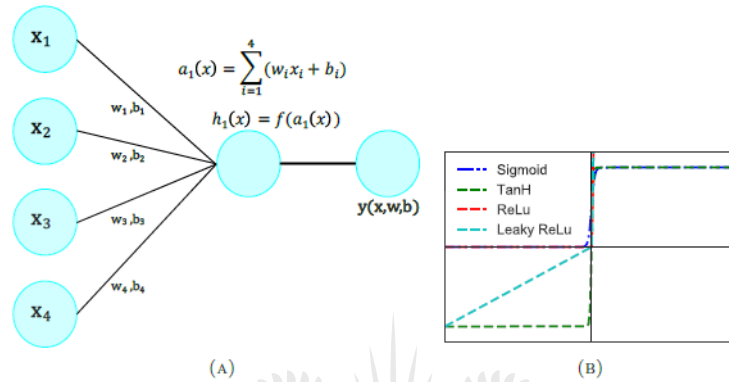
Figure 2.12: a)Schematic of a single layer perceptron b) Different activation functions in a perceptron [99].

2.8.2 Genetic Algorithm

A Genetic algorithm (GA) is a machine learning model, which are usually based on the natural selection and natural genetics mechanisms, inspired by Charles Darwin's principle of natural selection [115], [116]. GA was first proposed by Holland in 1975 [117]. The major idea behind natural selection is the fittest survive. Organisms adapt to optimize their probability of survival in a given environment by the process of natural selection. Usually, random mutations, genetically associated with an organism, can be passed on to its children. Therefore, individuals are evaluated and undergo an evolutionary process, starting with natural selection. The best individual is thus selected from the population. After which, a biological process will occur in the form of crossover, mutation and some recombination, made to create a new individuals generation that will hopefully produce a better offspring. The genetic algorithm is stopped when a target is eventually reached [112], [118]. The procedure for GA are viz:

1. Creating a population of random individuals.

2. Select individuals to be parents

3. Evaluate children

4. Produce children

5. Repeat the selection of individuals to be parents and evaluate children until the predetermined number of generations is met

6. Evaluate each individual's fitness [119]

The 1 and 0 sequence in the GA gene depicts a special solution. The binary number is referred to as one chromosome of the gene. Crossover in GA refers to gene exchange at a certain crossover point. A crossover example with 5 gene length is shown by Figure 2.13, while Figure 2.14 shows the mutation flipping the binary position [120].
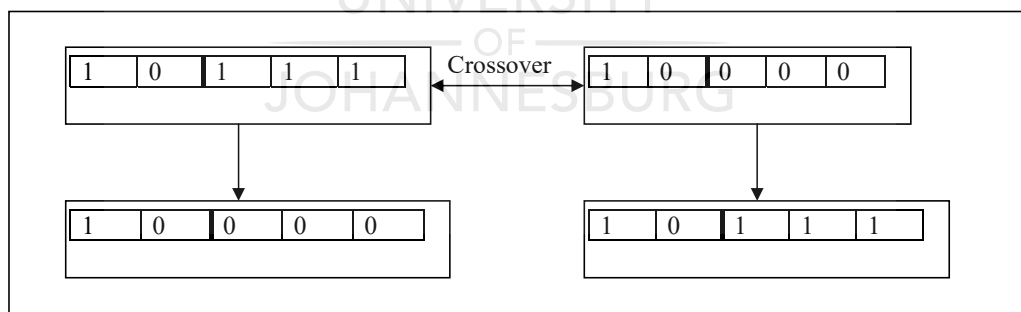
Figure 2.13: One Point Crossover Example [120].
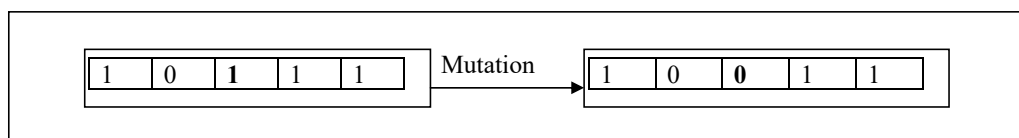
Figure 2.14: Example of a mutation [120].

2.8.3 Support vector machine

Support vector machine (SVM) learning model is a classification model that finds an optimal hyperplane which separates two different classes, as depicted in Figure 2.15. The main essence of SVM is to optimize the margin, which represents the distance from hyperplane to each plane closest point, to eventually have test data with a better classification performance. The basic idea that governs SVM can be simply described as: having classes of different data points, plotted in input features space, the logarithm should construct a plane, that will distinguish points into different classes as shown in Figure 2.16. [111], [121]. After finding the optimal hyperplane, the solution giving by the SVM algorithm can be described by the point located on its margin called "support vectors". The output of the algorithm for non-linear functions is obtained from non-linear space using kernel functions. Meanwhile, non-function are usually used for non linear mapping [122]–[124]. The classification of the functions can be done in five different parts; sigmoid,radial basis, polynomial and linear [125]. Non-linear decision boundary can be made without necessarily carrying out optimal hyperplane parameters computations in the feature space; the solution can therefore be expressed as weighted values of kernels functions combination [122].
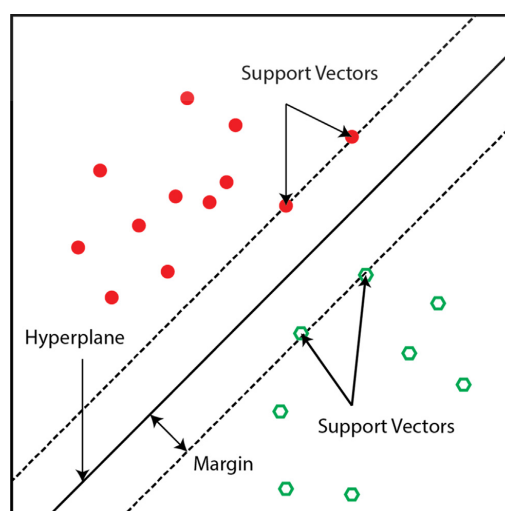
Figure 2.15: Hyperplane classification. [126].
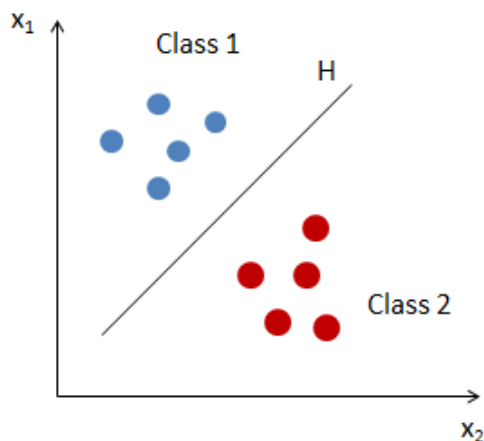
Figure 2.16: Separation of data points, referred to different classes, with a plane H. [111].

2.9   Literature summary

From the literature in this chapter, it is obvious that the porosity level plays a vital role in the weldability and mechanical properties of welded powder metallic alloy. Therefore, the thesis will focus more on the effect of pores on weld integrity. Also, different machine learning algorithms that can be used to predicts materials properties was reviewed. These have provided the adequate background needed to apply machine learning in predicting materials properties.

Chapter 3

Material experimental techniques and ML methods

3.1 Introduction

This chapter consists of three sections that explains the experimental techniques used in thesis. The first section explains the experimental procedures used for the sintering process, microstructural characterization. The second section explains the procedures taken for the Nd:YAG welding of the sintered alloy, microstructural characterization, mechanical analysis. Lastly, different machine learning are introduced to predict the mechanical properties of the welded metallic alloy are introduced.

3.2 Materials

Materials used in this study is powdered 2507 DSS, with high purity of 80.6% and an average particle size of 22μm, validated by Laser diffractometer analysis. The as-received powder of theoretical density of is 4.76 g/cm^3 was supplied by Sandvik Osprey Limited united Kingdom. Particle size distribution is shown in Table 3.1, which clearly shows the difference in shape size of the particles, while the chemical composition is presented below in Table 3.2.

Table 3.1: Particle size of the starting powder.

Powder	Purity($wt.\%$)	Particle size (μm)		
		D_{10}	D_{50}	D_{100}
2507 (DSS)	80.6	4.6	13.1	27.2

3.2.1 Powder Analysis

The morphology of the powder, which appears to be spherical was detected by field emission scanning electron microscope (FE-SEM) (model Carl Zeiss sigma, Germany) equipped with a dispersive energy X-ray (EDX). Pictures of a cross-sectioned powder revealed particles with a fine structure. It appeared that the internal porosity is low and small fractions of internal porosities can be located within the cross-section of the powder, as seen in Figure 3.1(a) and (b). Powder size distribution was obtained from imageJ as shown in Figure 3.2. Shows that the powder particles are within the ranges of approximately 5μm and 25μm. The phases present in the powder was confirmed by X-ray diffractometer (model) using Cu-Kα radiation, as shown in Figure 3.3. The powder consists of ferrite and austenite phases.

Porosity Analysis of the powder from SEM image

The SEM image gotten from the powder was processed in MATLAB, using the code developed by Rabbani [127]. They assume in the code that the input SEM image is gray-scale and the darker parts of the image show a deeper surface which are taken as the pores. This modelling is necessary to calculate the level of porosity in the powder sample. The algorithm used to segment the porous space of the powder is called watershed [2], capable of detecting overlapped porous geometry and effectively estimate the average pore size.

Table 3.2: Chemical composition 2507 DSS powder.

Material	C	P	Si	Ni	N	Mn	S	Cr	Mo	Fe
2507	0.02	0.014	0.4	7.1	0.31	0.8	0.001	24.4	3.76	Balance
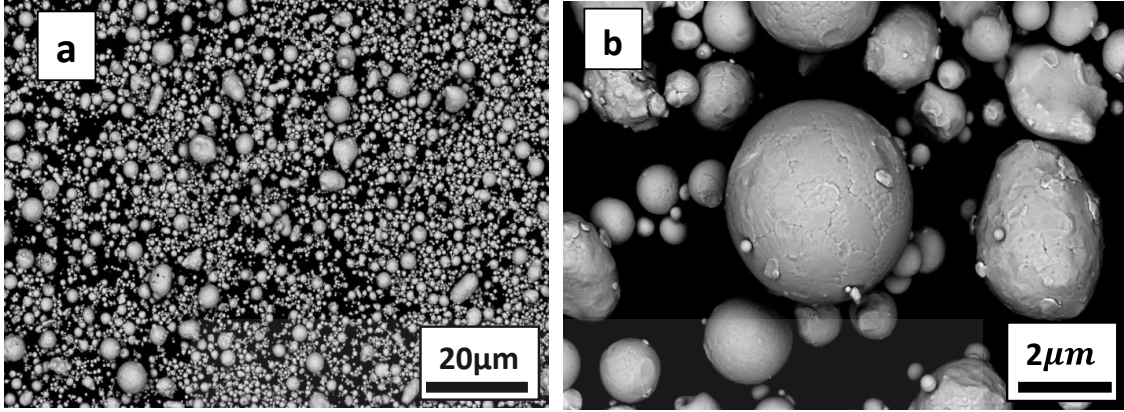
Figure 3.1: SEM image Showing morphology and particle size of 2507 duplex stainless steel powder. (a)20μm (b)2μm scale.
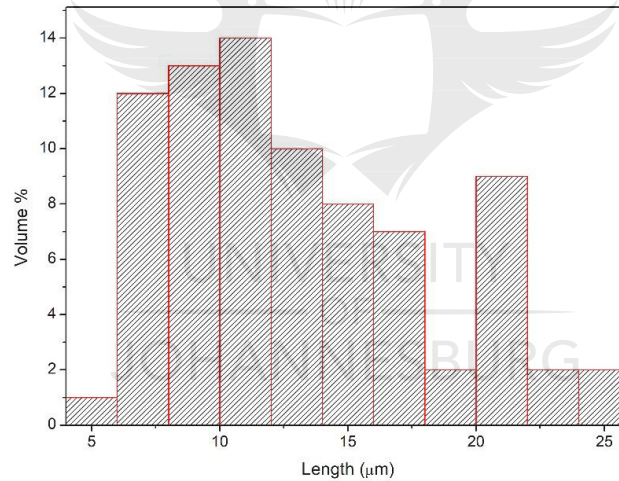
Figure 3.2: size distribution of 2507 duplex stainless steel gotten from image J.

3.3 Spark Plasma Sintering

All SPS experiment was carried out with SPS equipment (model HHPD-25, FCT system GmbH, Rauenstein, Germany). However, prior to the sintering process, the gas-atomized 2507 DSS powder was first pressed in 20mm graphite die and punches, while a tungsten foil was used to separate the samples from the graphite tools properly. The samples were then sintered at the following temperatures 900°C, 1000°C, and 1100°C at a pressure of 50MPa under vacuum. The heating rate considered
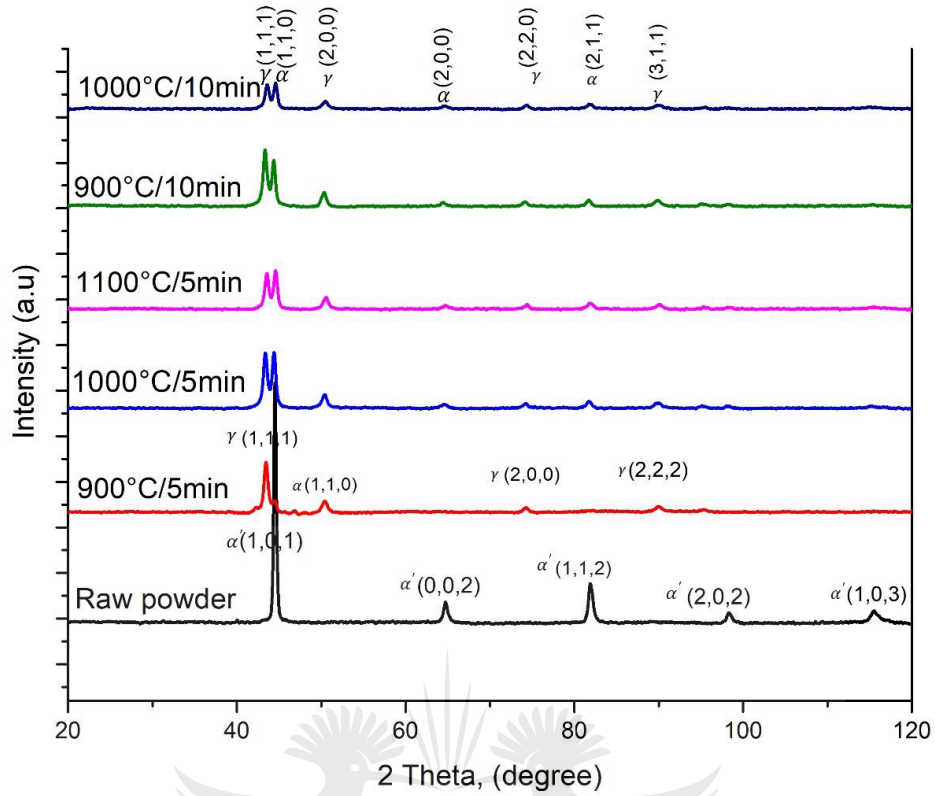
Figure 3.3: XRD patterns of 2507DSS.

for the sintering operation was 100°C/min, and it lasted between 5min-10min. The samples were then cool to room temperature inside the furnace in a vacuum atmosphere. Factoring in the strength, hardness, toughness, ductility, porosity, and particularly sintering temperature is usually selected at 0.6-0.8 Tm of the melting temperature of the alloy. Therefore for powders metallic alloy prone to oxide formations on the surface like stainless steel powders, it is advisable to carry out sintering at high temperature in pure hydrogen [128].

ASTM B962-14, a standard test method is used to calculate the density of PM sintered products using Archimedes' principle by measuring the density after sand blasting. The samples were first weighed in air, then immersed in a distilled water [129]. The density of samples was calculated using equation 3.1.

$$\rho_d = \frac{B_a}{B_a - B_w} \rho_w \tag{3.1}$$

Where B_a is the measured mass of the sintered sample in the air (average of three

independent measurements), B_w is the measured mass of the sintered sample in distilled water (average of three independent measurements), and ρ_w density of the distilled water (which is usually 0.998 g/cm³). Equation 3.2 can be used to calculate the absolute porosity.

$$P = \frac{\rho_{th} - \rho_d}{\rho_{th}} \tag{3.2}$$

P is the absolute porosity in %, ρ_{th} and ρ_d are theoretical and sample density, respectively. These parameters and calculated values are thus well presented in Table 3.3. while SPS equipment is shown in Figure 3.4.
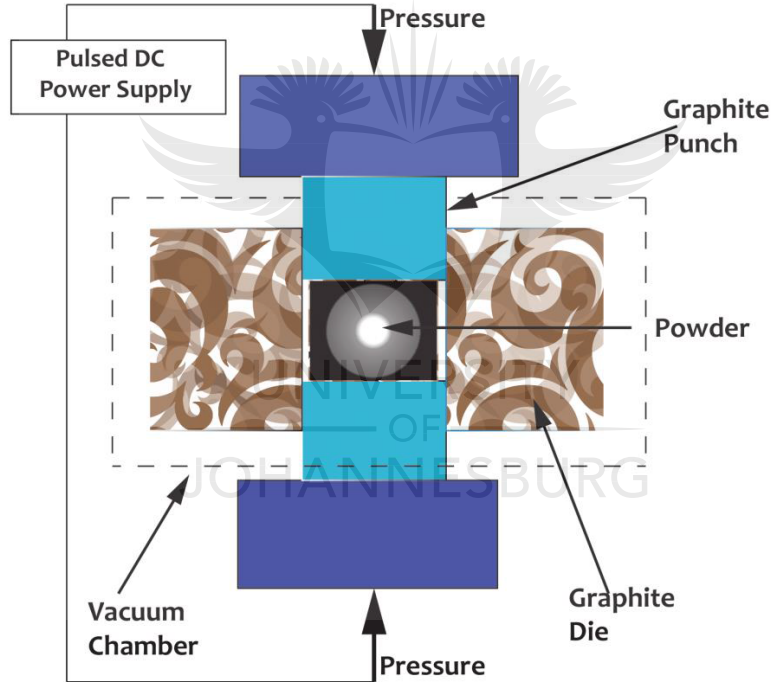
Figure 3.4: Schematic diagram of spark plasma sintering equipment.

Table 3.3: Sintering parameters.

No. of samples.	Sintering Temp.(°C)	Heating rate (°C/min)	Pressure (MPa)	Holding time(min)	Exp. Den (g/cm³)	Rel. Density(%)	%Porosity
1	900	100	50	5	7.16	91.85	8.15
2	1000	100	50	5	7.71	98.85	1.15
3	1100	100	50	5	7.67	98.33	1.67
4	900	100	50	10	7.69	98.54	1.46
5	1000	100	50	10	7.66	98.23	1.77

3.4   Nd:YAG Laser welding

Two specimens were each cut from a single piece of sintered 2507 DSS by wire cutting to (size: $12 \times 12 \times 3 \ mm^3$) joined in a butt joint configuration. The welding operation was performed with a JK 600 pulsed Nd: YAG laser welding machine at the Council for Scientific and Industrial Research (CSIR), South Africa. The welding of the sintered 2507 DSS was performed at average welding power of 1500W, welding speed of (2-3m/min) in an argon (99.99% purity) environment and focal position 5mm. The laser was made to point vertically at the interface of the base alloy. The welding process parameters were determined based on existing literatures and experimental researches. Porosity level is a major determinant of the level of welded metallic alloy integrity. Researchers have shown that metallic alloy with low porosity produces a weldment with outstanding properties compared to high porous metallic alloy, as porous media act a potential site that traps oxides and impurities, which tends to mar the mechanical properties of the weld [130]. Therefore, from Table 3.3, samples 2, 4, and 3 are selected to be welded due to having low porosity. Thus, samples 2, 4, 3 will be designated as samples A, B, and C, respectively as shown in Table 3.4.

Table 3.4: Welding parameters

Samples	Laser Power (W)	Welding speed(mm/min)
A	1500	3
B	1700	3
C	2000	2

3.5   Characterisation Methods

Characterisation of the samples includes microstructure characterisation and secondary phase quantification. The samples are made to undergo standard grinding and polishing procedures, employing grit size up to 3000 followed by electro-chemical etching using 50% KOH solution (5V for 3 secs). The optical microscope (OM)

Figure 3.5: Sintered and cut specimen.

Figure 3.6: Laser welded specimen.

analysis was done using (Axio Carl Zeiss microscopy, GmbH, Germany). Field emission scanning electron microscope (FE-SEM) (model Carl Zeiss sigma, Germany) equipped with an energy dispersive X-ray (EDX) was used to analysed the phases present. Electron backscatter diffraction (EBSD) pattern was acquired on Zeiss cross-beam 540 Scanning electron microscope at an electron voltage of 25kV and a probe current of 10nA. The EBSD data analysis was performed on Oxford EBSD detector with Aztec analysis software and EBSD reference pattern database.

3.6 X-ray computed tomography to analyze the porosity in the weld

X-ray computed tomography (XCT) was used to characterize the spatial and size distribution of the residual pores in the laser-welded sintered samples. The porosity characterization was carried out using X-ray tomography analysis, performed at the University of Stellenbosch CT facility [131]. General Electric (GE) Nanotom S nanoCT scanner system with voltage and current set to 140kV and 130μA was used for the X-ray setting, using 0.5mm copper beam filter, with a voxel size set to 5.0μm. The image was acquired at a time of 500ms per image and recorded in 2000 rotation steps during sample full 360 degree rotation. The system supplied Datos reconstruction software was used to reconstruct the image. Volume Graphics VGStudio Max 3.3. was used to perform data visualization and imgage analysis.

3.7 Mechanical properties analysis

Vickers hardness was conducted to assess the mechanical integrity of the weld.

3.7.1 Vickers hardness test

Microhardness measurements based on the Vickers method were performed using Future-Tech microhardness Tester (FM-700) with an applied load of 100g indentation for 25s. The test was conducted from the BM through HAZ to the WM at a distance ranging from 0mm - 1.5mm.

3.8 Machine learning data analysis and prediction of mechanical properties of the weld metal (WZ)

3.8.1 Exploratory data analytics

In this information era, where there is enormous data like medical data and materials data. Therefore, it is not a coincidence that data science has assisted us in making decisions in all spheres of life. Data science has been accepted as a viable tool in materials science and engineering field to analyze the properties of the materials. The cost of material structure design has been reduced by data science [132]. In this research data used for the input parameters and output parameters are sourced from the experimental processing parameters; sintering temperature, sintering time, welding power, and hardness, which has been published in Mendeley database and our published work [133]. The input parameters are obtained from the welding parameters and sintering parameters while the microhardness used for the prediction was obtained from the WZ. There have been some researches that indicated the importance of the chemical composition to the WM integrity [48]. The data used for the statistical analysis and machine learning analysis were selected based on the optimized parameters, leaving us with 3 samples having outstanding mechanical properties. The Vickers microhardness data targeted at the WM was carried out at different distance for 10 iterations, each for 3 optimized samples, giving us 30 data points. Since hardness values varies along the WM. The datasets of 30 instances were processed using Google Tensor flow, employing the Sklearn packages and python code, to carry out the data analysis: data cleaning, normalization of the data, data splitting to training and test sets, which is later subjected to regression analysis and eventually visualized using different packages in Python. Pearson coefficient and R^2 are the metrics used to calculate the extent of correlation of the input and the output parameters.

Governing equation for data analysis

Normalization of the data was performed by equation 3.3.

$$Y = \frac{(Y_{max} - Y_{min})(X - X_{min})}{X_{max} - X_{min}} + Y_{min} \tag{3.3}$$

Y stands for the normalized datasets, and X is the inputs datasets. The Linear progression equation is represented by equation 3.4.

$$y = b_0 + b_1 x \tag{3.4}$$

x represents the independent variable while the dependent variable is y, b_0 is the intercept, and b_1 is the slope.

$$R^2 = (1 - \frac{MSEofregressionline}{MSEoftheaveragedata}) \tag{3.5}$$

MSE is mean square error, and R^2 is the measure or metrics used to determine how close the data is to the fitted regression line. Pearson correlation is another metric used to measure the correlation strength between measured hardness values and predicted hardness values.

3.8.2 ANN prediction of hardness

Microhardness test

Vickers microhardness (HV) test was carried out using Vickers microhardness (Future Tech FM-700) tester, applying a load of 100g with a dwell time of 25s at room temperature. The Vickers microhardness test was targeted at the WM for this research. The chemical composition of the WM is significant for the mechanical integrity of welded metallic alloy. The microstructure of the WM also differs from the base metal (BM) because of the variations in the chemical composition and the thermal history of the WM [48]. The importance of WM to the overall mechanical integrity of the welded metal made us consider the hardness of the WM in this re-

search for predictive analysis. An average of three spots hardness values were used and utilized in the Neural network because of the variation in hardness around the WM zone. The hardness values are based on the measurements at the WM area.
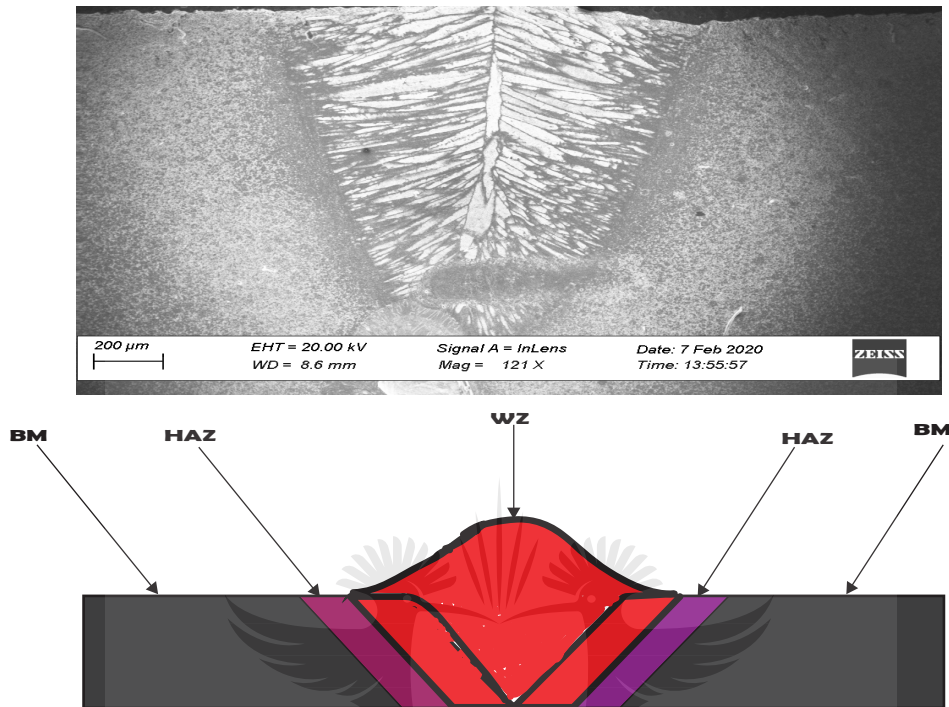
Figure 3.7: Schematic diagram showing the welding zones

ANN Algorithm

In the material processing industry, it is pertinent for material to undergo precise and consistent output to meet the required quality standard set. A neural network has recently been used as a technique developed on processing elements, named neurons that have connections with each other [134]. Given adequate data and algorithm, machine learning with the help of computers has the ability to determine all know physical law [135]. The last decade has witnessed a massive application of Artificial Neural Network (ANN) in many optimizations and prediction applications. ANN is classified as highly nonlinear functions and can capture very complicated patterns in data. They have become the leading technique in machine learning and helped solved complex engineering problems, including the prediction of mechanical properties of materials. They can be represented by the following function indicated

in equation 3.6, where x is the input vector and $\hat{y}$ is the prediction, $f^{(k)}$, $f^{(1-4)}$ represents functions that maps input to output values [135]. Figure 3.8 shows the steps followed for the implementation of the use case.

$$\hat{\boldsymbol{y}} = f(\boldsymbol{x}) = f^{(k)}\left(...f^{(4)}\left(f^{(3)}\left(f^{(2)}\left(f^{(1)}\right)\right)\right)...\right) \tag{3.6}$$

The first layer is called the input layer, it transfers information from the outside entity to the network, while the intermediate layers are called the hidden layers. It acts as the connecting link between the input layer and output layer by performing computation and transferring information between the input and the output layers. The last layer is the output layer, mainly responsible for the computations and re-laying information to outside the world. Therefore, these layers are made of neurons, which can be thought of as a simple computational unit that takes a weighted sum of input variables, sends the sum through an activation function and the output is the predictions. For the gradient descent equation, a linear transformation was applied to an input x by each neuron in the layers, described by equation 3.7, while Figure 3.9 presents the flow chart.

$$\boldsymbol{t} = \boldsymbol{W}\boldsymbol{x} + \boldsymbol{b} \tag{3.7}$$

Where $\boldsymbol{t}$ is a tensor, $\boldsymbol{W}$ is called the weights, and the vector $\boldsymbol{b}$ are is biases. The nonlinear transformation applied by each neuron is called the activation function.

Activation function

There are many activation functions in literature, such as the sigmoid, the hyperbolic tangent, and the rectified linear unit or ReLU. Sigmoid and the hyperbolic tangent are subjected to the so-called gradient vanishing. ReLU activation has enjoyed wide application within neural networks, especially deep neural networks. At the inception, researchers were stimulated to use ReLU because of its biological resemblance. Meanwhile, the ReLU function later showed an improvement in the neural network
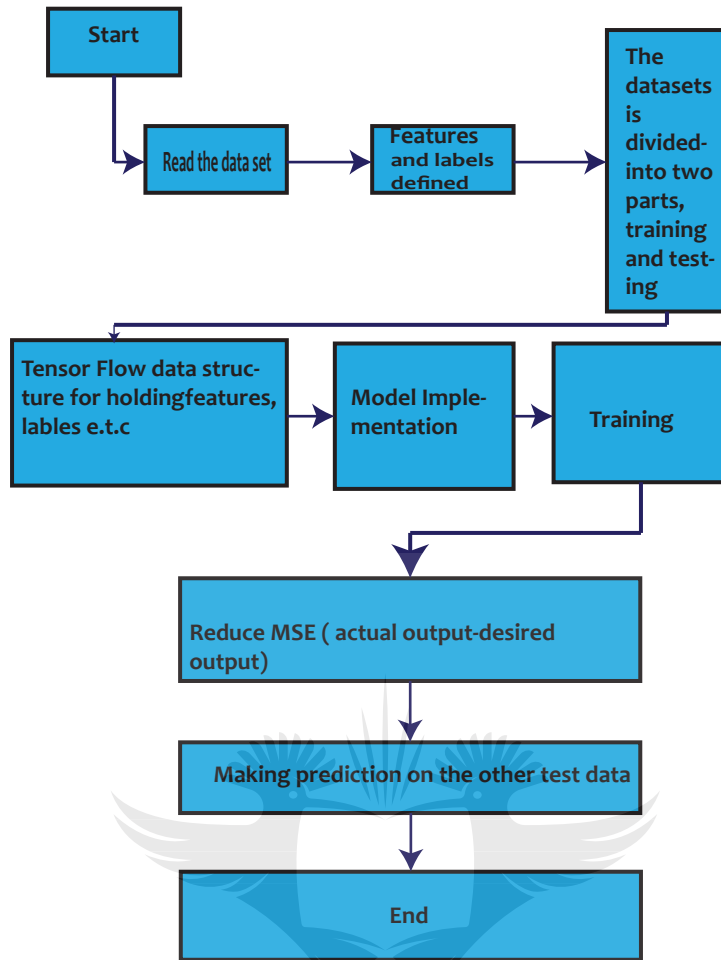
Figure 3.8: Flow diagram for the implementation of the use-case
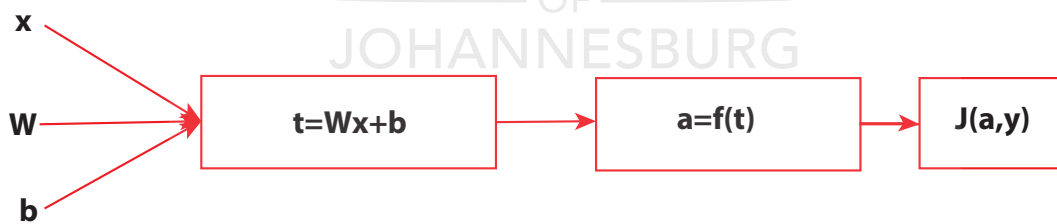
Figure 3.9: Flow chart for the linear transformation

trainig speed, which eventually translates to good results. The top-notch accurate predictive power can be attributed to its simplicity and function derivative. The derivative can be computed easily and does not have a vanishing gradient problem [136]. In this research, the ReLU function was used mainly because it is piecewise and highly nonlinear. It gives better results than the sigmoid and the hyperbolic tangent. Therefore, for this reason, it will be delightful to investigate how a ReLU

function actually helps the networks to approximate functions. Figure 3.10 illustrate ReLU activation function, while Table 3.5 shows the parameters used in the ANN.

$$\hat{\boldsymbol{y}} = f^{(k)}\left(..f^{(4)}\left(\boldsymbol{b}^{(4)} + \boldsymbol{W}^{(4)}f^{(3)}\left(\boldsymbol{b}^{(3)} + \boldsymbol{W}^{(3)}f^{(2)}\left(\boldsymbol{b}^{(2)} + \boldsymbol{W}^{(2)}f^{(1)}\left(\boldsymbol{b}^{(1)} + \boldsymbol{W}^{(1)}\boldsymbol{x}\right)\right)\right)\right)\right)$$

$$(3.8)$$
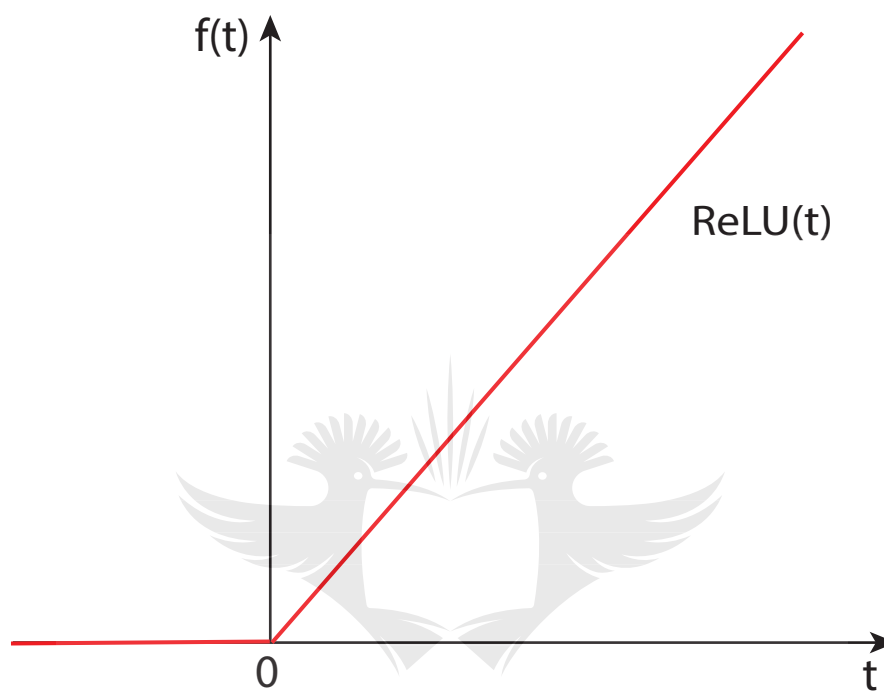
Figure 3.10: The ReLU activation function

Table 3.5: ANN parameters

Model	Parameter (W)	Value
	Number of Input layers	4
	Number of Hidden layers	2,3
ANN	Number of Output layer	1
	Maximum No. of Epochs	750
	Activation function	RMSprop
	Learning rate	0.001

The cost function

Defining a loss or cost function is fundamental to any machine learning problem. During the training process, the interest is in weight that minimizes the discrepancies

between the estimated hardness values of the weld zone in contrast to their actual training data values. The accuracy of the network in the prediction of the new hardness value that is not from the training set tend to increases. There are many cost functions, but for regression problems, the most widely used is the mean square error. In introducing the mean square error cost function, an assumption was made on the dataset:

$$\{(x_i, y_i)\}_{i=1}^N \tag{3.9}$$

With given pairs: features x_i and corresponding target value $y_i \in R$. vector of targets is denoted as $y \in R^N$, such that y_i is target for object x_i. Similarly, $\hat{y} \in R$ denotes predictions for the objects: $\hat{y}_i$ for object x_i. The MSE loss function is defined as follows:

$$MSE(y, \hat{y}) = \frac{1}{N} \sum_{i=1}^N (\hat{y}_i - y_i)^2 \tag{3.10}$$

The goal of the learning algorithm will be to minimize the MSE loss function. In the context of the Deep Neural Network(DNN), this cost function will be written as follows:

$$J(\theta) = \frac{1}{N} \sum_{x \in \boldsymbol{X}} (\boldsymbol{y} - f(\boldsymbol{x}; \boldsymbol{\theta}))^2 \tag{3.11}$$

This is called the loss function of the ANN. The parameter $theta$ (θ) stands for the weights and the biases that need to be optimized to minimize the loss function, and this is done through backpropagation.

Backpropagation

Backpropagation can be described as a supervised learning algorithm for training multi-layer ANN. In this research, work backpropagation was used to compute the gradient of the loss function as indicated by the Equation 3.12

$$\nabla_\theta y = \nabla_\theta J(x; \theta) \tag{3.12}$$

In addition, the choice of the network parameter does not affect the training data; backpropagation consists of finding the gradient of the network. Once the gradient is computed, gradient descent or any related algorithm could be used iteratively to minimize the loss function

$$\theta_k = \theta_{k-1} + \epsilon \nabla_\theta J(x; \theta) \tag{3.13}$$

Where ϵ is called the learning rate, and its value must be set with care for convergence reason. Therefore, the errors are propagated in reverse in the network to adjust the parameter θ until the loss function reaches its minimum.

The optimizer

Recently, diverse methods have been initiated to effectively minimize the loss function by tracking not only the gradient but also the second moment of the gradient. These methods include AdaGrad, AdaDelta, ADAM and Root-Mean-Square propagation (RMS-prop). In RMS prop, in addition to keeping a running average of the first moment of the gradient, the second moment can be tracked or monitored through a moving average. Therefore, the update rule for RMS prop is given by:

$$
\begin{aligned}
\mathbf{g}_t &= \nabla_\theta J(\boldsymbol{\theta}) \\
\mathbf{s}_t &= \beta \mathbf{s}_{t-1} + (1 - \beta)\mathbf{g}_t^2 \\
\boldsymbol{\theta}_{t+1} &= \boldsymbol{\theta}_t + \eta_t \frac{\mathbf{g}_t}{\sqrt{\mathbf{s}_t + \epsilon}},
\end{aligned}
\tag{3.14}
$$

Where β dictates the averaging time of the second moment and is usually taken to be about $\beta = 0.9$, η_t is a learning rate typically chosen to be 10^{-3}, and $\epsilon \sim 10^{-8}$ is a small regularization constant to prevent divergences. It can be inferred from the formula above that the learning rate is reduced in directions where the norm of the gradient is persistently large. Convergence is speed up to enable a larger learning rate for flat directions [137].

Model implementation and learning

ANN model was implemented in an open source Python based deep learning library called Keras with Google machine learning application, TensorFlow framework is used as the back-end engine. ANN with back-propagation algorithm was implemented with four input parameters, namely, welding speed(w-speed), welding temperature(w-temp), sintering time (s-time), and sintering power (s-power). All the processing parameters have an influence on the Vickers hardness of the welded sintered DSS alloy [138], [139], the data used for this analysis has already been published in Mendeley data. The data obtained from the WZ of each sample was split into training and testing data, which was later used in the final evaluation of the model. The ANN models presented in this study utilizes 2 to 3 hidden layers, which are appropriate for the number of unique data. With small data point, the ANN model was tweaked for different activation functions and training algorithms. Meanwhile, 80% of the data was selected as the training data, while the rest was selected for testing. Before training and testing the network, the training datasets were normalized to avoid convergence of the model, thereby making the training to be more difficult and eventually making the resultant model to depend on the unit's choice used in the input. It is a known fact theoretically that ANN has no restriction on its training data even when the magnitude of the measured data varies greatly. To achieve a more excellent training accuracy, it is better to put the training data source in the same order before going ahead. With this understanding, input and output variables were normalized to the range [0,1], using equation 3.3. Four neurons were fixed in the input layer corresponding to the input layer, with a hidden layer with variation between 2 and 3 layers. One neuron corresponding to the one output was fixed in the output layer, as shown in Figure 3.11 (a) and (b). RMSprop optimizer was used to minimize loss. To improve the generalization property of proposed neural network model, early stopping technique was used. Also, early stopping was adopted to stop the training after a step of epochs elapses without showing improvement. In this research, the number of hidden layers that perfectly

gives an optimized neural network was obtained through trial and error by varying the training algorithm, activation function and hidden layers. The model was later compiled for the minimized MSE, R^2 and MAE loss function, which was used as the metric to evaluate the prediction precision. MAE is represented by equation 3.15. The model was later trained for 1000 epochs, visualization of the training models was done using the statistics stored in the history.

$$MAE = \frac{1}{n} \sum_{t=1}^{n} |e_t| \qquad (3.15)$$

(a)   (b
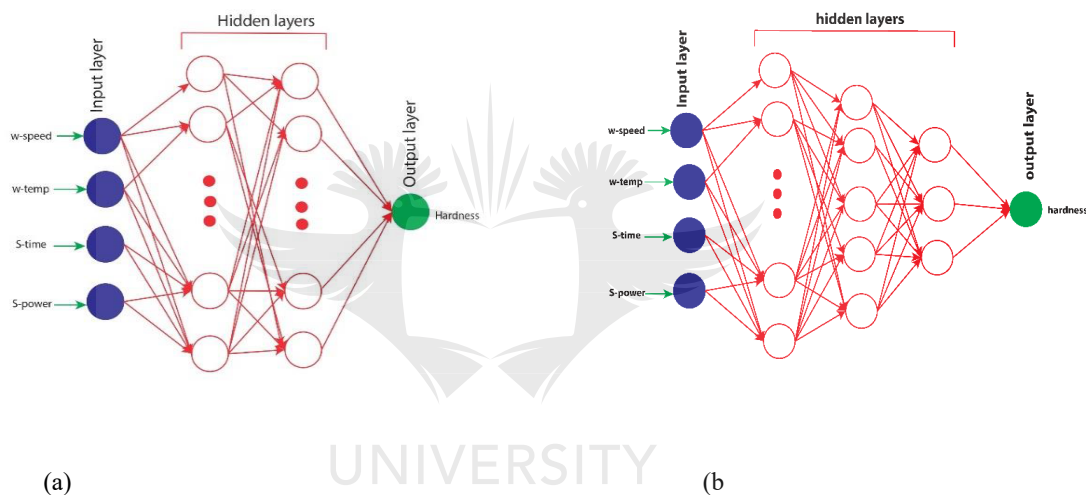
Figure 3.11: (a) 2 hidden-layers and (b)3 hidden-Layers graphical representation of Neural network.

3.8.3 SVM

The same datasets used for ANN was used for SVM. In this research, the predictions were carried out using MATLAB software, implementing linear and non-linear SVM kernels. Linear, quadratic, and cubic kernels were used. The accuracy of the SVM models is compared using different metrics mentioned earlier. The SVM algorithms is one of the most powerful machine learning tools. It uses a set of mathematical functions called kernels that usually transform input data into high dimensional space, after which the data points are classified in distinct clusters. The MATLAB code used for the SVM analysis can be found in Appendix A.B.

Linear Kernel

Linear SVM correlates with linear kernel where $\phi(x) = x$ and $\phi(x') = x'$. The linear kernel optimization problem is much faster when compared to others [140]. Finding perfect training data can be time-consuming. Therefore, to reduce the time, two running parameters (gamma and regularization parameter) can be introduced in the SVM classifiers.

Nonlinear SVM Kernels

As the linear models give limited classification power, non-linear models give more enhanced predicted outputs [141]. Various kernels can be used to transform nonlinear function features. The kernels are listed and explained below:

- Polynomial Kernel: Polynomial function is usually employed to input variables and finding similarities in training vectors [141].

$$K\left(x_i, x_j\right) = \left(1 + x_i x_j\right)^p \tag{3.16}$$

- Quadratic Kernel: With quadratic kernel, it is possible to visualize the given data points being lifted to fit into the shape of a quadratic function[141]. Suppose there are two features (x_1, x_2). Quadratic kernel expands the two into five $(x_1, x_2, x_1^2, x_2^2, x_1 x_2)$. The decision boundary is given by:

$$\mathbf{w}^T \phi(x) + b = 0 \tag{3.17}$$

where $\mathbf{w}^T$ is a vector, b is bias, and $\phi(x) = (x_1, x_2, x_1^2, x_1, x_2, x_2^2)$. Quadratic kernel leads to decision boundary having a mixture of quadratic functions. The decision boundary is defined by $y \big| \sum_i \alpha_i k\left(x_i, y\right) = b$. For example, consider

the decision boundary and the kernel function $k\left(x, y\right) = \left(x^T y + c\right)^2$:

$$
\begin{aligned}
\sum_i \alpha_i \left(x_i^T y + c\right)^2 &= \sum_i \left[\alpha_i \left(x_i^T\right)^2 + 2\alpha_i x_i^T y + \alpha_i c^2\right] \\
&= \sum_i \alpha_i y^T x_i x^T y + \left(\sum_i 2\alpha_i x_i\right)^T y + c^2 \sum_i \alpha_i \\
&= y^T \left(\sum_i \alpha_i x_i x_i^T y\right) y + \left(\sum_i 2\alpha_i x_i\right)^T y + c^2 \sum_i \alpha_i
\end{aligned}
\tag{3.18}
$$

- Cubic Kernel: It is usually defined as a third-order polynomial function. Cubic kernel can be used to visualize the given data points being formed to fit into the shape of a cubic function [141]. Assuming there are only two features (x_1, x_2). The decision boundary in such case is usually given by:

$$
\beta_0 + \beta_1 x_1 + \beta_2 x_1^2 + \beta_3 x_2 + \beta_4 x_2^2 + \beta_5 x_2^3 = 0
\tag{3.19}
$$

The equation for the SVM model trained with the cubic kernel is:

$$
K\left(x_1, x_2\right) = \left(x_1^T x_2 + 1\right)^2
\tag{3.20}
$$

K is the kernel function.

- Gaussian Radial Basis Function Kernel: most sought out for among the kernel functions in SVM classification [141]. It is defined as :

$$
K\left(x_i, x_j\right) = \exp\left[-\frac{\left|x_i - x_j\right|^2}{2\sigma^2}\right]
\tag{3.21}
$$

The adjustable parameter σ is set according to the nature of the problem. If set very low, it affects the regularization functions and eventually making the training data to be sensitive to noise; however, when sets high, the kernel behaves almost linearly, causing overestimation of the problem [141].

3.9 Summary

For the machine learning predictions, ANN model with 2-3 hidden layers was employed. The prediction power was compared with all the different SVM with linear, quadratic, cubic and Gaussian kernels described above. The Processing parameters for both sintering and welding operations constitute the parameters used to generate the input data. These includes: Welding speed, welding temperature, sintering temperature, and sintering power. The hardness data to be predicted was measured data at the WM interface of the welded alloy.

Chapter 4

Results and Discussion

4.1 Introduction

The results of the experimental work and discussion in this chapter are presented in three parts. The first part discusses the microstructure of the sintered part. The second parts will be dedicated to the microstructure and mechanical characterisation of laser-welded sintered parts.

4.2 An XRD analysis

An XRD pattern of the 2507 duplex stainless steel is presented in Figure 3.3, which confirmed the presence of austenite and ferrite phases in all the sintered samples at (900°C/5min, 1000°C/5min, 1100°C/5min, 900°C/10min, 1000°C/10min) and raw powder.

4.3 SEM powder image processing analysis using MATLAB

Using the watershed algorithm discussed in chapter 3 for image analysis. The pore size distribution, porosity and the standard deviation of the pore size of the powdered sample SEM image were calculated. Figure 4.1. shows the original and the final

processed images. The porosity in the powdered sample is calculated by dividing the total porous area by a number of pores observed. Also, the MATLAB programme was able to calculate the pore size distribution by measuring the area of the detected pore and calculates the radius of the equivalent circles within the same area, as shown in Table 4.1. The observed phenomena can be explained thus, whenever large particle size is packed close to one another, the empty spaces between the particles (pores) will be larger. In contrast, while the pore size will be reduced when the particle size is smaller. Table 4.1 shows the porosity, average and standard deviation of the pore sizes of the powdered sample.
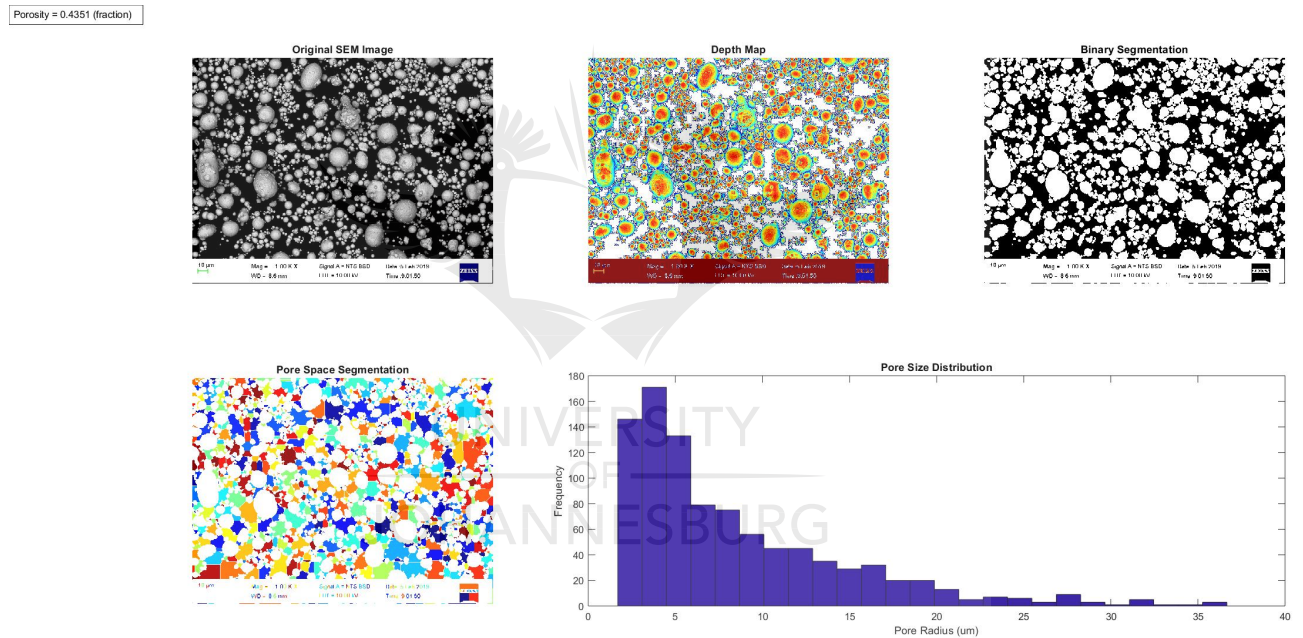
Figure 4.1: 2507 SEM powder image porosity and pore size analysis using MATLAB.

Table 4.1: Properties of powdered particles extracted from SEM image

Parameters	Values
Average Porosity (Micro)	8.4658
Standard deviation of Pore size (Micro)	6.3938
Porosity (Ratio)	0.4351

4.4   Microhardness and density studies

The effect of sintering temperature on the relative density and hardness of the developed 2507 DSS samples are shown in Figure 4.2. High relative densities of more than 98% was observed for samples sintered at different sintering conditions. A relationship between sintering temperature and relative density was established as the relative density of metallic alloy are usually influenced by the sintering temperature. It was noticed that the maximum relative density of 98.85% was achieved at sintering temperature corresponding to 1000°C. There is slight variations in the density values for the sintered samples. It can be inferred from the plot that the microhardness of the sintered alloy decreases with increasing sintering temperature. The increment in sintering temperature from 900-1100°C resulted in a maximum microhardness of 375HV at 900°C. This result is similar to that of a metallic alloy that is heat-treated. Hence, the higher the holding temperature, the faster the grain growth Phenomenon. Therefore hardness evolution is related to grain growth [142]. Also, the value of the microhardness can be attributed to the particle re-arrangement and homogeneous redistribution of the secondary phases, which usually occur at elevated temperatures [143].

4.5   Microstructural characterization

4.5.1   SEM analysis of the laser-welded samples

The BM, WM and HAZ microstructure for samples A, B, C are shown in Figure 4.4 SEM image. During the laser welding, ferrite formed directly from the liquid molten pool, while after cooling, there is the transformation of austenite in the form of high ferrite in form of grain boundary austenite (GBA) [144], Widmanstatten austenite (WA) [145] and intragranular austenite (IGA) [146]. There is high austenite transformation in WM, which in a way prevented chromium nitride precipitation. The HAZ also experience austenite transformation from ferrite, similar to what is observed in WM. The austenite content is lower in HAZ compared to BM, the lower
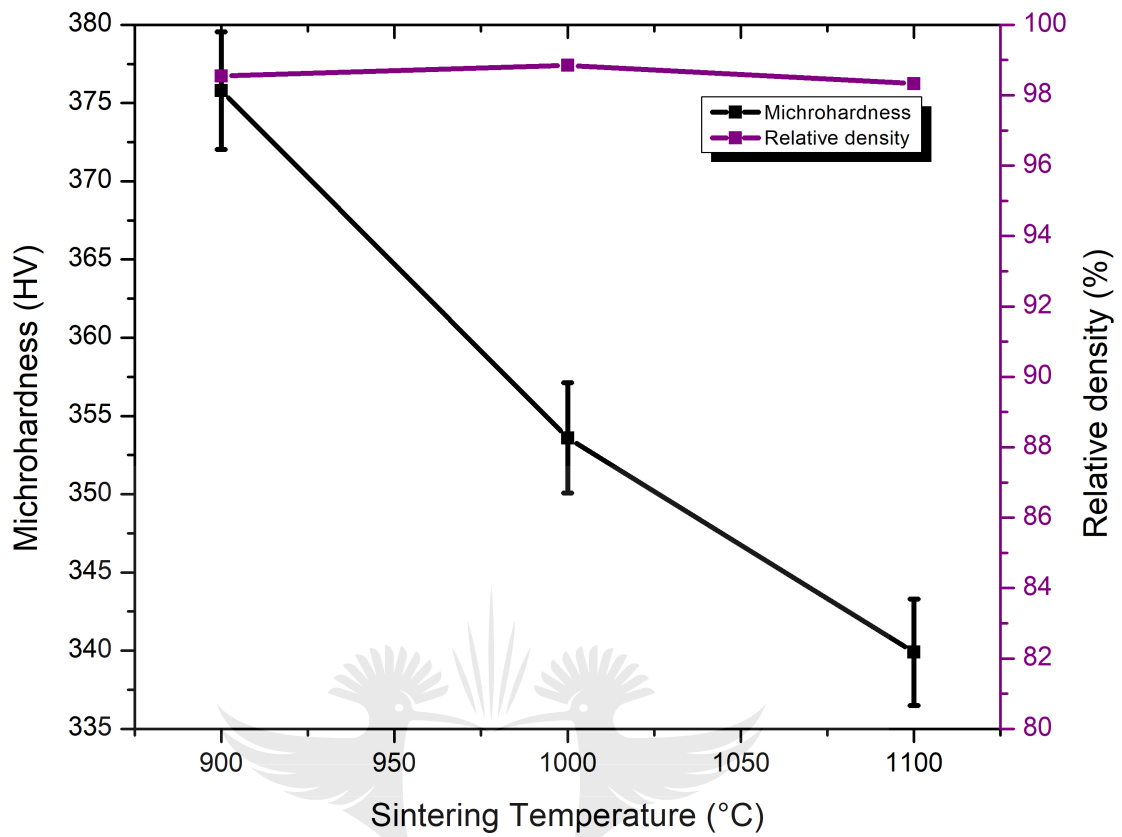
Figure 4.2: Effect of sintering temperature on Relative Density and Microhardness properties of sintered 2507 DSS.

austenite in the HAZ can be associated with two factors since the laser welding process comes with fast cooling. There is limited time available for the austenite to transform from ferrite due to the fast cooling rate at the HAZ; 2)The thermal welding cycle produced ferrite grains that are coarse in the HAZ, as reported in the work of Zhang et al. [147]; in consequence, there is a noticeable decrease in the ferrite grain boundarie, and eventually, there is a decrease in the GBA nucleation sites, and finally producing less austenite content. Chromium nitrides are usually precipitated during the rapid cooling process of the laser-welded samples. The precipitation of the chromium nitride within ferrite can be due to inadequate diffusion of N. Cr_2N rods was observed within the ferrite matrix in HAZ at high magnification, as shown in Figure 4.5c for samples A, B, C. It is known that Cr_2N precipitate is detrimental

to the mechanical properties of the DSS.
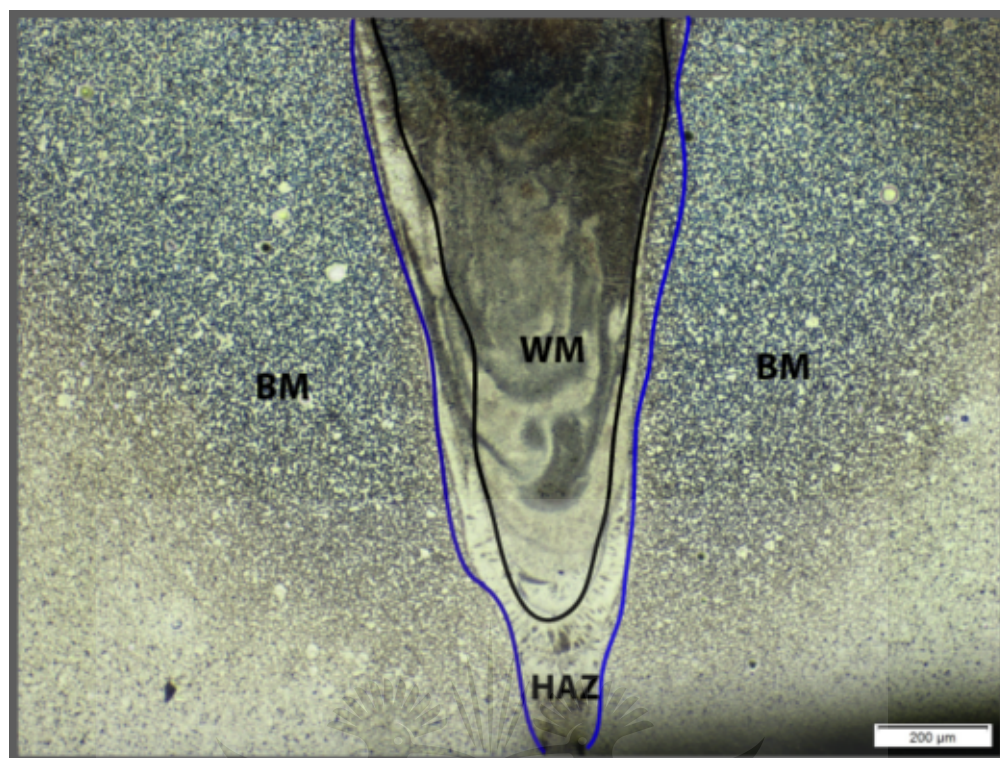
Figure 4.3: Optical image showing the cross-section of BM,WM, and HAZ.
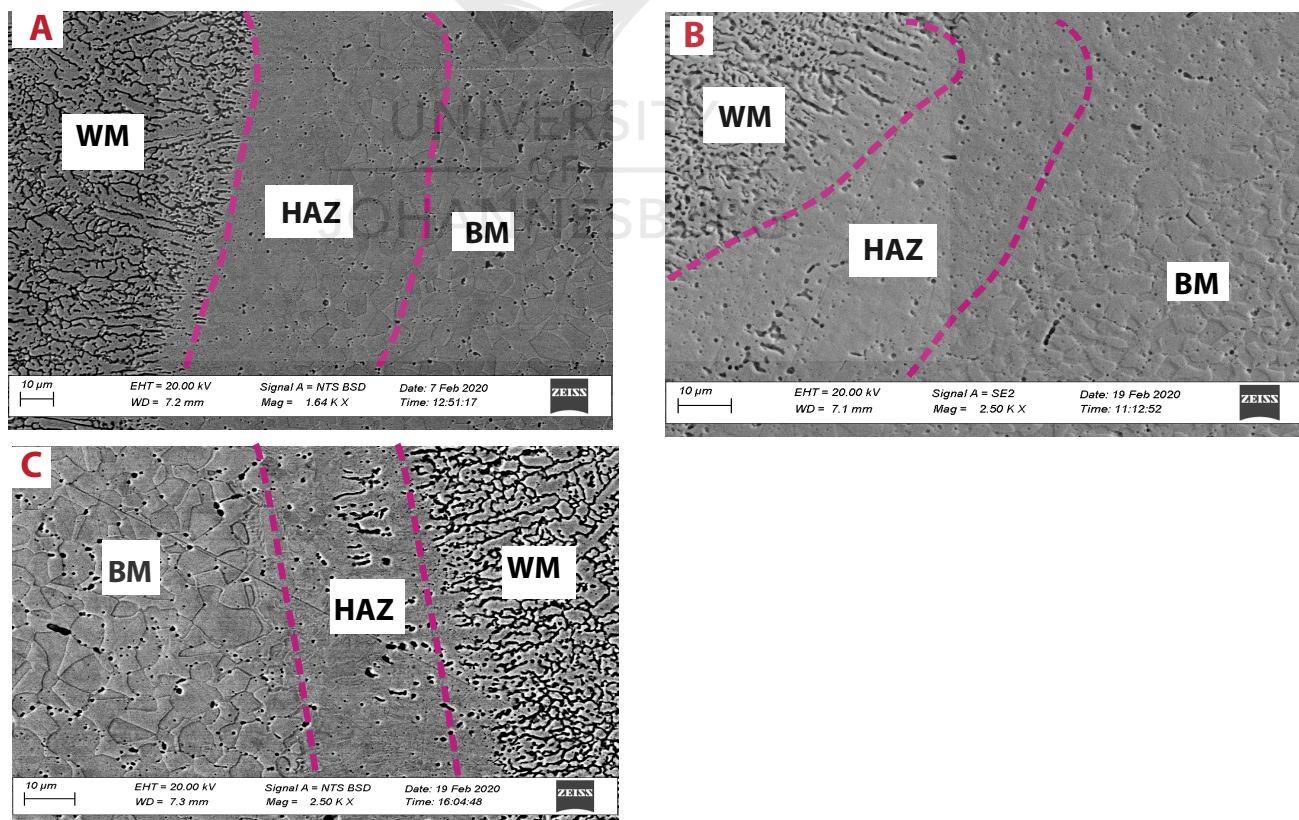
Figure 4.4: SEM image for samples A, B, C showing the BM,WM, and HAZ.

(a) BM

(b) WM
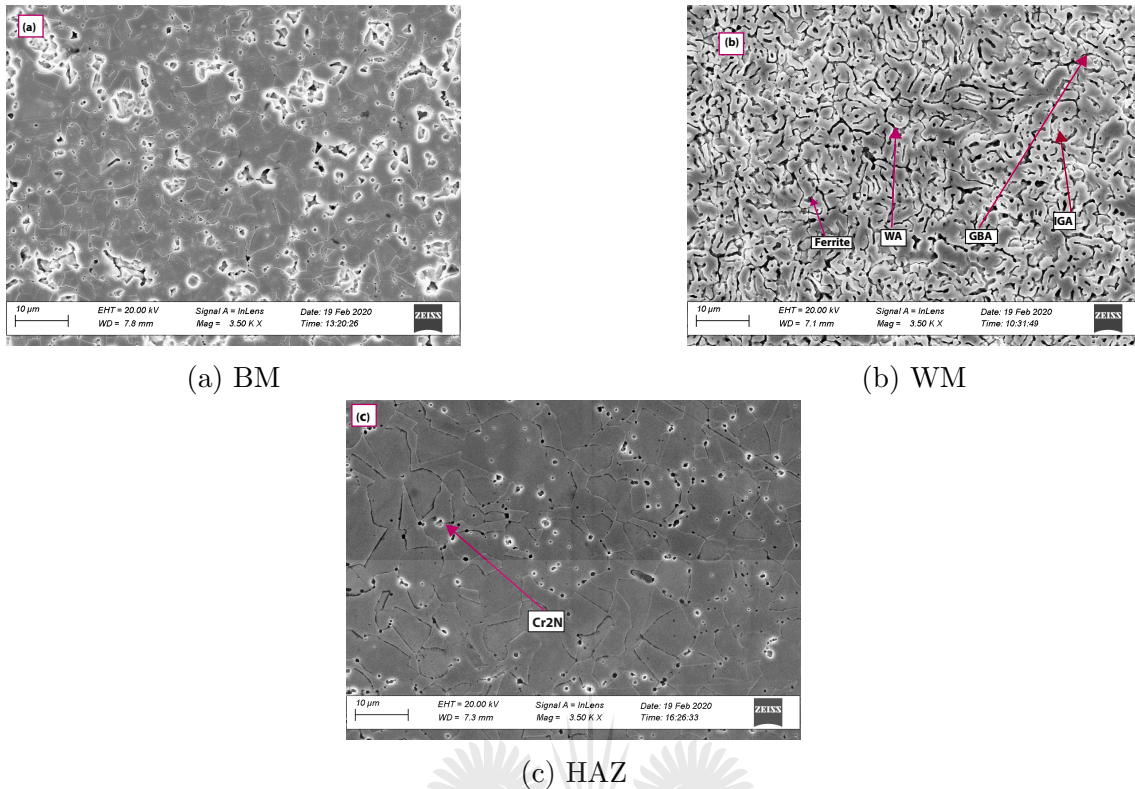
(c) HAZ

Figure 4.5: Microstructures of the 2507 DSS joints. (a) BM, (b) WM, (c) HAZ (the inset shows a SEM image of the Cr_2N precipitates within ferrite)

4.5.2 EBSD Analysis

The EBSD examination was used to identify the grain size in the HAZ. It was observed in Figure 4.6 (b) that the grain size of the as-welded HAZ is generally large compare to BM. The austenitic phase can be noticed at the HAZ. The unique microstructure observed in the HAZ is associated with phase transition during the weld thermal cycle. Through the heating period, the banded microstructure of ferrite and austenite close to the fusion line transform into δ ferrite. Also, at the interface of the WZ, there is a diffusion of alloying elements (Cr, Mo) and carbon takes place, prompting it to form carbon precipitates at the boundaries in the form Cr_2N during cooling. Meanwhile, Ni alloy dissolved in the δ ferrite, due to high cooling rate fine austenite inform of δ ferrite is noticed in the HAZ. In the work of Bettahar et al. [148] It was made known that the ratio of ferrite and austenite in the HAZ of 2205 stainless steel weld depends on the cooling and the alloy composition.
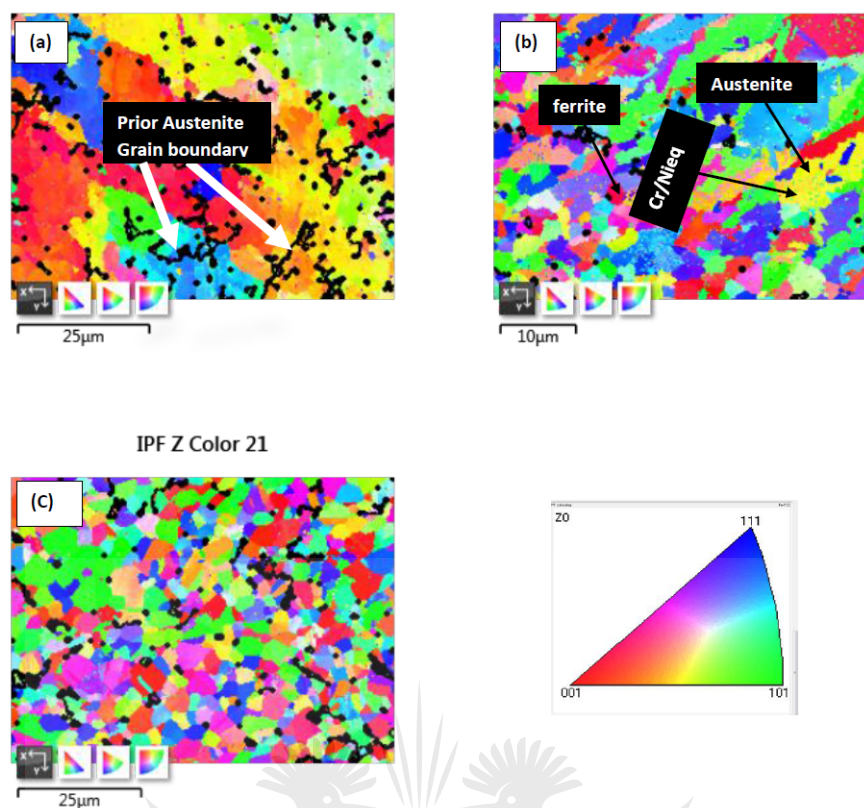
Figure 4.6: Microstructures of the 2507 DSS joints for sample A, EBSD image showing the orientation (a) WM (b) HAZ (c) BM

4.6 Hardness distribution of the weld

The microhardness profile across the welded joints for different Nd:YAG samples (A, B, C) is shown in Figure 4.7. There is a significant variation of hardness value across the weld. The WM shows highest microhardness value for the samples A,B,and C. The average microhardness value for sample A WM is 386.4 HV, while the average microhardness of the HAZ for sample B is 367.5 HV. Sample B WM shows highest average microhardness value of 365HV and 339HV average HAZ microhardness value. The hardness value for samples A, B and C is the lowest at the BM. High hardness value. High hardness at the WM can be ascribed to the presence of a high amount of ferrite [149]–[151].
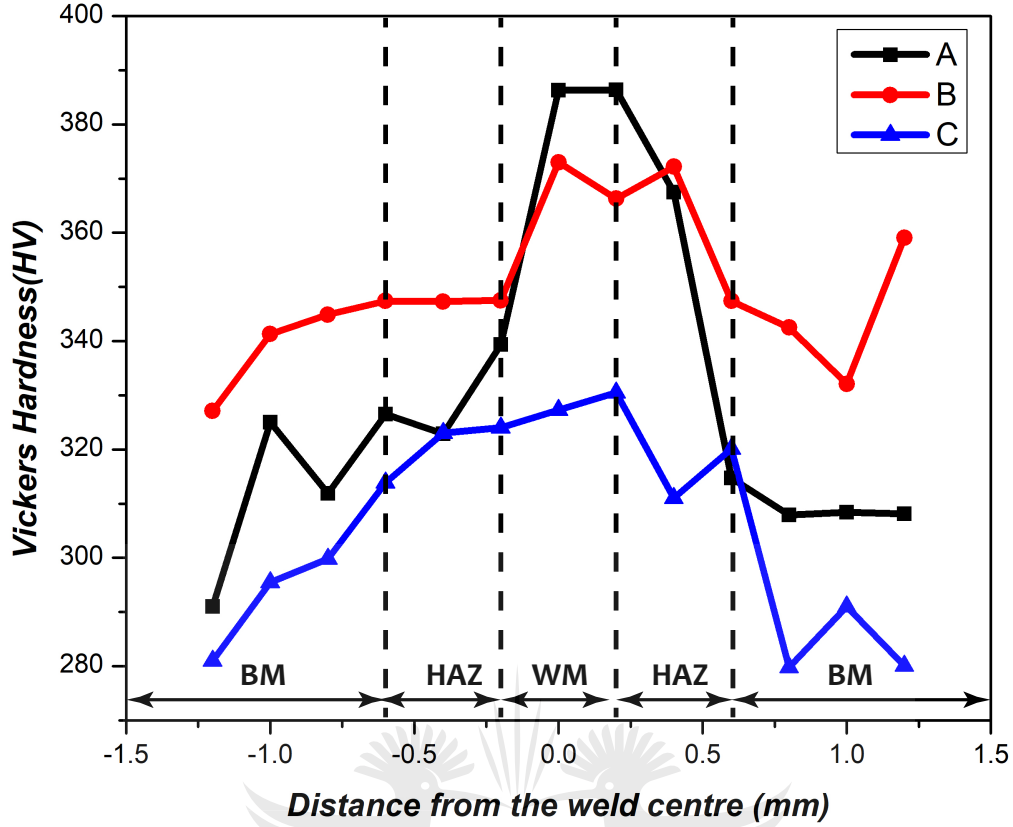
Figure 4.7: Vickers hardness measured across the weld plot.

4.7 X-ray computed tomography analysis

Reconstructed side views transparent porosity distribution was shown in Figure 4.8. Sample A shows the least or minimum pore volume compared to sample B, and C, this contributes to its high hardness at the WM. Also, the pores are limited only to the WM for samples A and C, with sample B having the pores scattered not only in WM, also in HAZ/BM. Pore morphology is found to be more spherical in the case of sample C and irregular in shape for samples A and B. According to Jiang et al. [152]. The pore morphology was characterized using the sphericity formula as shown in equation 4.1;

$$\psi = \left(\frac{36 V_p^2}{A_p^3} \right)^{1/3} \tag{4.1}$$

Where ψ stands for the sphericity of pores, $\psi=1$ shows that the sphere is perfect. A_p and V_p represent surface area and volume of the pores, respectively.
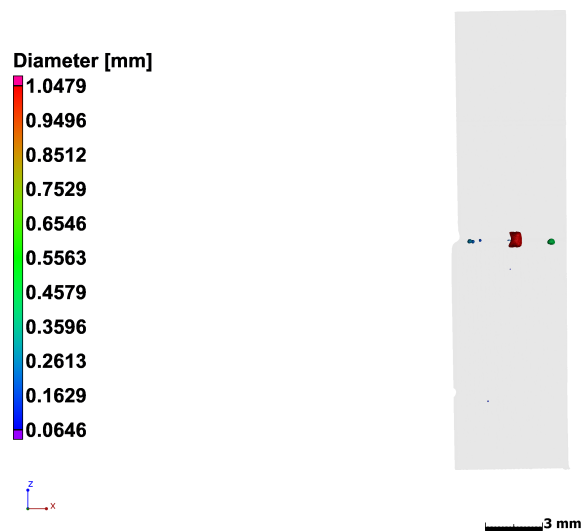
(a) Sample A
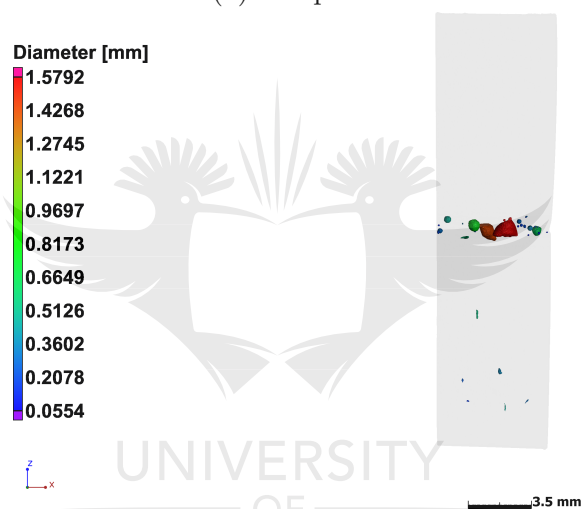
(b) Sample B
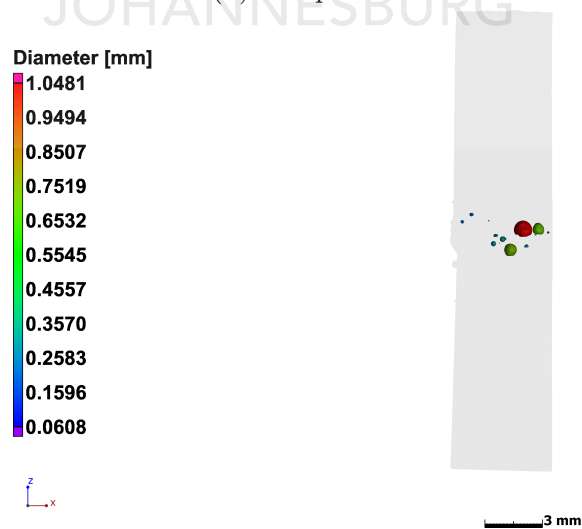
(c) Sample C

Figure 4.8: Reconstructed side view transparent porosity distribution of Nd:YAG Laser welded joint.

4.8 Data Exploration and visualization

4.8.1 Seaborn Plot

According to the paired seaborn plot(Figure 4.9), showing marginal distributions for all pairwise relationships and each of the following variables; s-temp, s-time, wel-power, and hardness in each column. It also shows the univariate distribution plot of each variable on the diagonal axis.
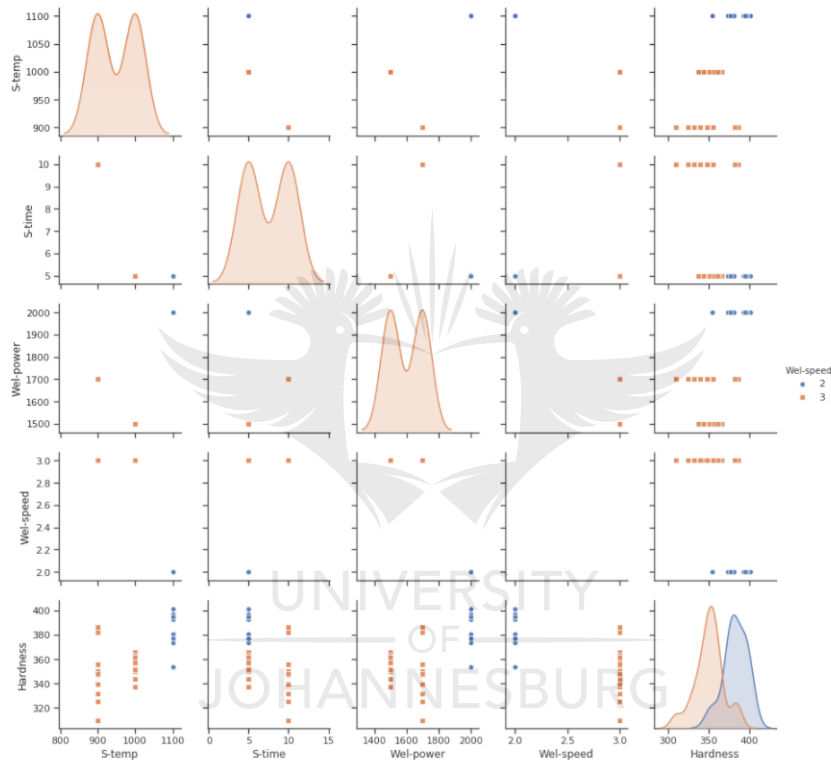
Figure 4.9: Seaborn Plot.

4.8.2 Heatmap analysis

The heatmap plot shown in Figure 4.10 represents a 2-D visualization of the data. Table 4.2 presents the correlation data of the input and output parameters, providing the relation between two features, presented by the shades of colours. To determine collinearity in our data and to visualize the numeric predictors correlation matrix, heat map analysis will be used. Visualization was carried out by the heat map and target variables like (Hardness) proportional to colour with re-

spect to variables, 'wel-power', 'S-temp', 'S-time', and 'wel-speed' in the vertical and horizontal axis, respectively. This allows us to visualize the hardness is related to 'wel-power', 'S-temp', 'S-time', and 'wel-speed'. It was then checked if the features are highly correlated with each other. Highly correlated attributes are shaded darker than the rest, which signifies a positive correlation, as shown in Figure 4.10. High correlation was noticed between S-temp and hardness, S-time and hardness,it can be concluded that S-temp, S-time and Wel-power are a good predictor for hardness. The same information can be inferred from the correlation values from Table 4.2. S-temp indicates a large positive relationship with hardness, S-time indicates moderate positive relationship with hardness, Wel-power indicates a moderate positive relationship with the hardness, Wel-speed indicates large negative relationship with the hardness.
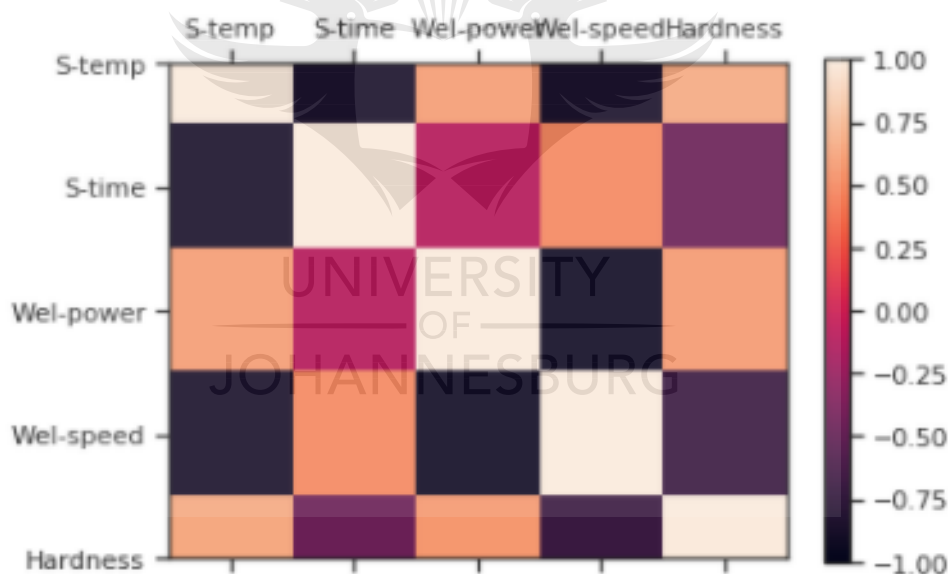
Figure 4.10: 2-D Heatmap Visualization map.

Table 4.2: Correlation Analysis

	S-temp.(°C)	S-time (min)	Wel-power(W)	Wel-speed(mm/min)	Hardness(HV)
S-temp	1.0000	-0.8660	0.5960	-0.8660	0.6600
S-time	-0.8660	1.0000	-0.1147	0.5000	-0.4539
Wel-power	0.5960	-0.1147	1.0000	-0.9177	0.5823
Wel-speed	-0.8660	0.5000	-0.9177	1.0000	-0.6892
Hardness	0.6600	-0.4539	0.5824	-0.6892	1.0000

4.8.3 Regression plot

Linear regression plot represented by Figure 4.11 shows hardness against sintering time(S-time). Figure 4.12 illustrates the regression plot for welding power (Wel-power) against hardness. While Figure 4.13 describes the linear regression plot for hardness against welding speed (Wel-speed). Fig. 4.14 illustrates the regression plot for hardness against sintering temp (S-temp). Meanwhile, for all the regression plots, some data points are scattered and far from the fitted line. The blue diagonal line represents how perfect prediction should be to the closest blue points (observations) to the diagonal line, the better the model.
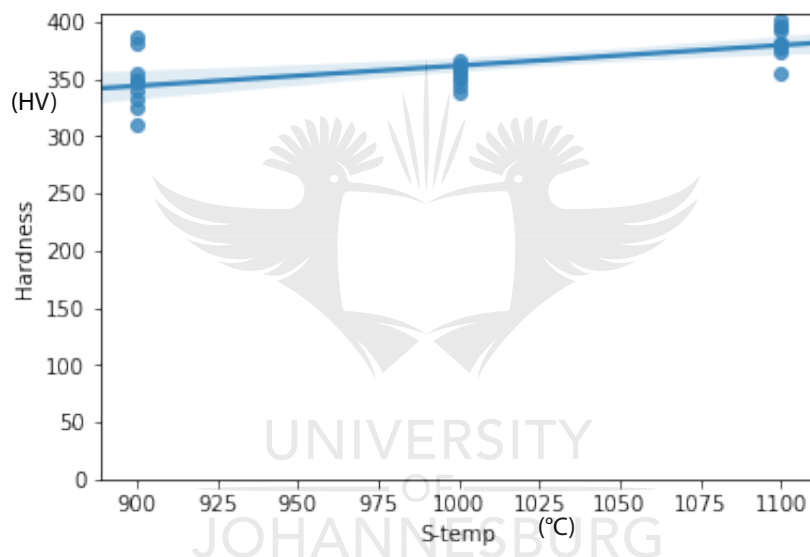
Figure 4.11: Linear Regression plot of hardness against Sintering temperature.

4.9 Machine learning analysis

4.9.1 ANN Prediction

Parameters and the range used in the ANN model is presented in Table 4.3. The model is proposed with 4 input layers, varying the hidden layers between 2-3 hidden layers, using ReLU activation function. In the neural networks, the weight and biases are adjusted iteratively by using a training algorithm. Figure 4.15 shows the numbers of hardness values to be predicted. Meanwhile, the most important metric
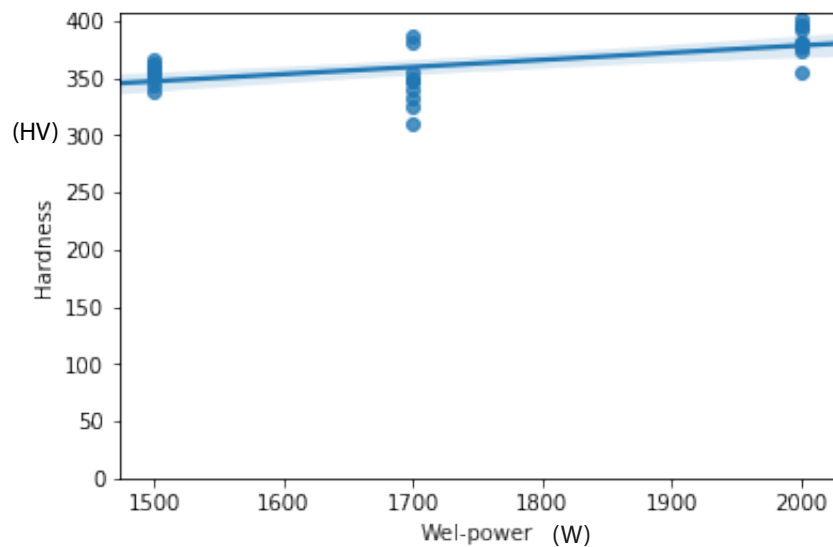
Figure 4.12: Linear regression plot of hardness against welding power.
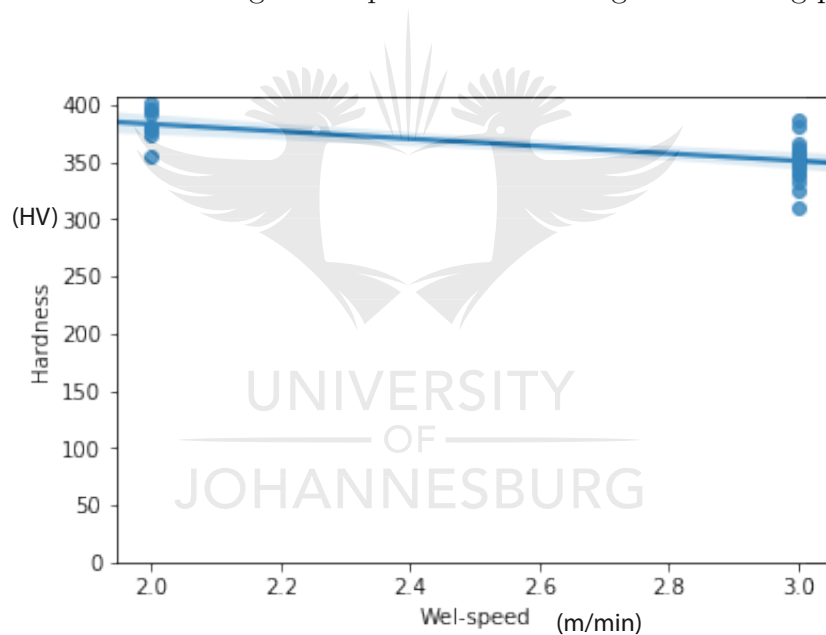
Figure 4.13: Linear Regression plot of hardness against welding speed.

performance used in this neural network is MSE [138] The regression plot of the developed ANN model for hardness prediction at the WZ of 2507 is shown in Figure 4.16(a) and (b). Therefore, the basic training curve calculated from the training datasets gives an idea of how well the model is learning. The basic validation curve calculated from a holdout validation dataset that gives an idea of how well the model is generalizing. Figure 4.17 and Figure 4.18 shows little improvement or even degradation in the validation error after approximately 100 epochs. To improve the
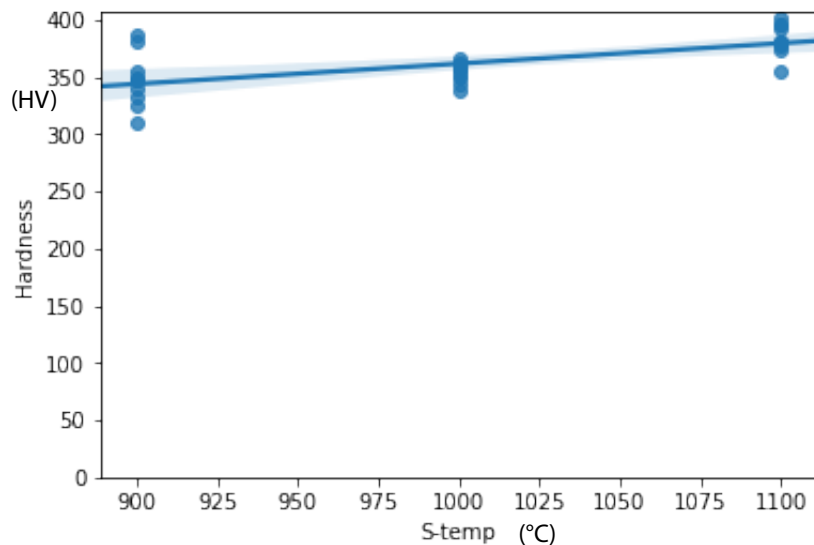
Figure 4.14: Linear Regression plot of hardness against sintering temperature.

network generation, the combination of MSE and the mean square of the weights are minimized, weights are also considered as random variables with Gaussian distribution. However, for generalization property of the different ANN proposed to be improved, an early stopping callback is used. If the set amount of epoch elapses without showing improvements, the early stopping callback automatically stops the training, as shown in Figure 4.19(a) and 4.19(b). The plots show that the training process stopped, as soon as the error validation set started to increase, showing the variation of MAE and MSE with epoch. In this research R^2 and MAE are metrics used in evaluating and predicting the precision of proposed models for both test and training sets, shown in Table 4.4 [153]. Meanwhile, different activation functions and optimizers available under Keras API was tested, ReLU and RMSProp respectively give the best optimized predicted values, with 2 and 3 hidden layers. It is important to note, as shown in Table 4.4, that the model performs better when applied to the test set than when it is applied to the training set. The reason may be due to the fact that training datasets have more data points than the test sets, therefore there is a probability of it containing a greater number of abnormal values is high, thereby significantly increasing the MSE value. The best R^2 gotten for both test and training for hidden layers 2 and 3 have the best value compared to others tested number of hidden layers. Meanwhile, the value of R^2 gotten shows low ability

of generalization. Table 4.5 and 4.6 show the predicted values with their errors, for both test and training sets, representing the best predicted ANN architecture with two hidden layers. Figure 4.15 shows the plot of the actual values and the predicted values. The maximum and the minimum possible errors values for the prediction of the hardness value are 9.57% and 0.09%. Clearly, with such a small dataset, lack of generalization is expected, warranted the use of another metric to appreciate how well the model is at prediction. The percentage error was computed on each prediction according to Equation 4.2. TV is the target value and PV is the predicted value.

$$PE = 100 \times \frac{|TV - PV|}{TV} \tag{4.2}$$

The code is available on Github: https://github.com/AyorindeTayo/ANN-prediction-of-Hardness-using-Tensor-Flow/blob/master/ANNhardness.ipynb

Table 4.3: parameters and their range used in the ANN

Parameter	minimum	Maximum	mean	Standard deviation
S-temp	900	1100	1000	83.41
S-time	5.0	10	1733	2.41
Wel-power	1500	2000	1733	210
Wel-speed	2.0	3.0	2.67	0.48
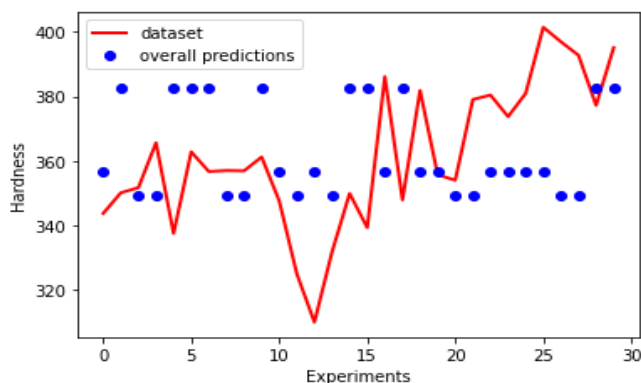
Figure 4.15: Actual versus ANN predicted results for hardness.
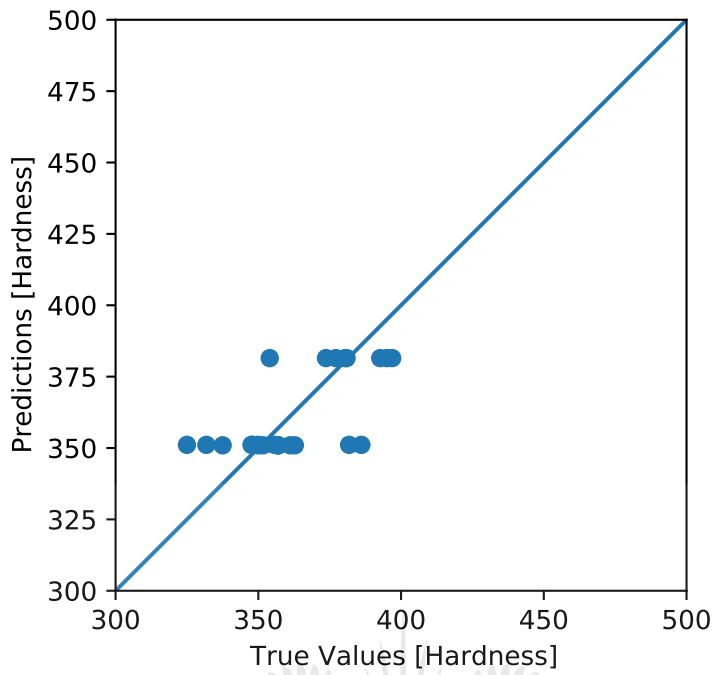
(a) Training
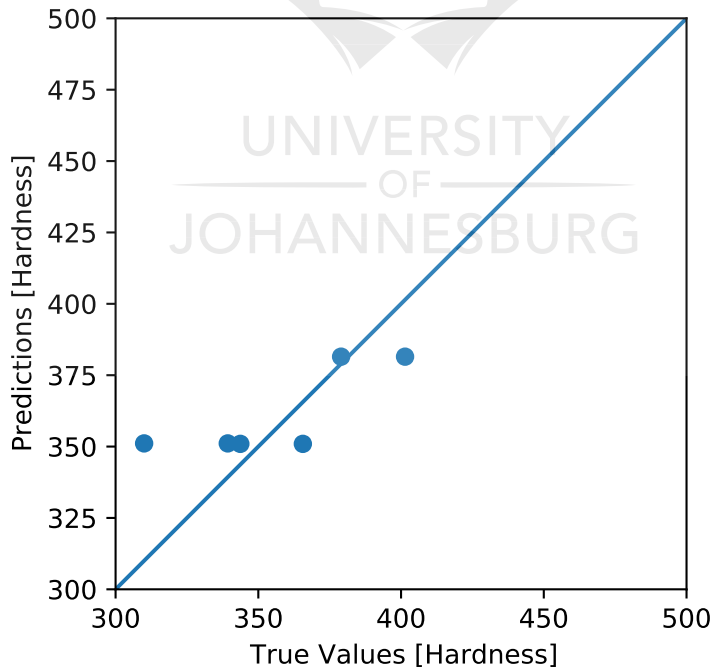
(b) Testing

Figure 4.16: Plot of predicted hardness values against True hardness value (HV) for (a) Training and (b) Testing sets.)

Table 4.4: Calculated values for R^2 and MAE for training and testing data.

Model(Hidden layers)	Training R^2 MAE	Test R^2 MAE
2	0.43 9.60	0.54 15.42
3	0.41 10.50	0.57 15.42
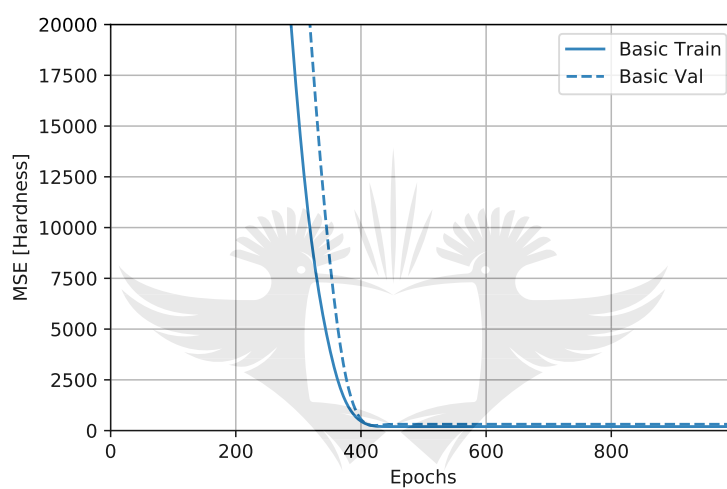
Figure 4.17: Plots of MSE against number of Epochs.
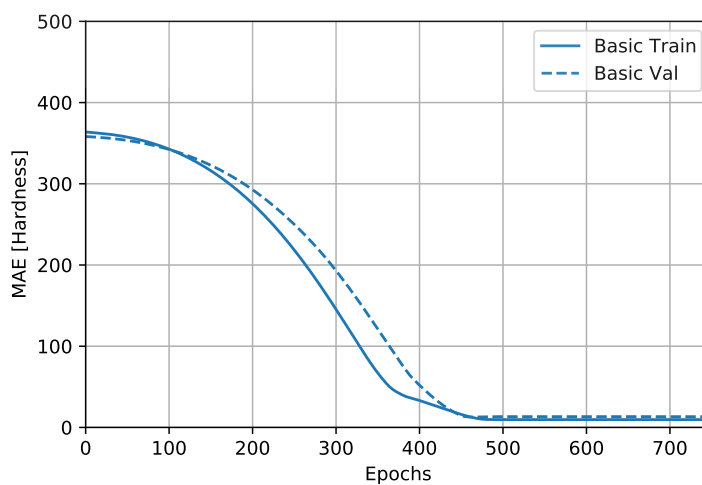
Figure 4.18: Plots of MAE against number of epochs.
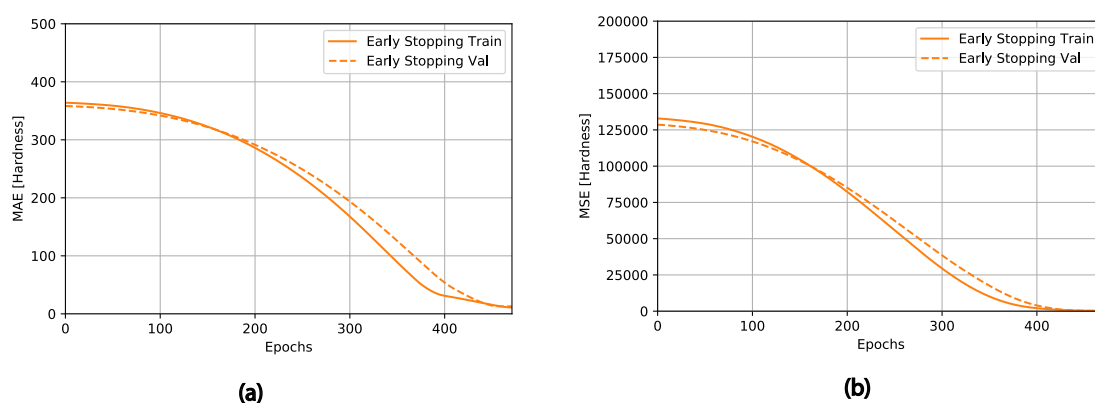
Figure 4.19: Early stopping plot of (a) MAE and (b) MSE against Epochs.

Table 4.5: Training Predictions vs True value of Hardness.

Number	True values	Training Predictions	% error
2	351.70	35.56	1.38
28	377.20	382.58	1.43
13	331.80	349.17	5.23
10	347.60	349.17	0.45
26	396.90	382.58	3.61
24	380.90	382.58	0.44
27	392.70	382.58	2.58
11	325.00	349.17	7.44
17	347.90	349.17	0.36
22	380.40	382.58	0.57
5	362.80	356.56	1.72
16	386.10	349.17	9.57
8	356.90	356.56	0.09
14	349.90	349.17	0.21
23	373.70	382.58	2.38
20	354.00	382.58	8.07
1	350.10	356.56	1.85
29	395.10	382.58	3.17
6	356.70	356.56	0.04
4	337.50	356.56	5.65
18	381.80	349.18	8.55
19	355.70	349.187	1.84
9	361.2	356.56	1.28
7	357.0	356.56	0.12

4.9.2 Comparison of SVM Kernels

Performance assessment of the SVM algorithms has been carried out using several statistical methods that describe the model fitting. The Statistical Performance of

Table 4.6: Testing Prediction Vs True Values of Hardness.

Number	True values	Testing Prediction	% error
0	343.7	356.56	3.74
3	365.7	365.56	2.47
12	310.0	349.17	12.64
15	339.3	349.17	2.91
21	379.0	382.58	0.95
25	401.0	382.58	4.69

SVM with linear, quadratic, cubic, and Gaussian kernel for the datasets is shown in Table 4.7, contains the summary of statistical metrics and their respective calculated values employed for evaluating the ML models. This method shows how well the predicted values fit with the actual data. Quadratic SVM and Gaussian SVM has a better performance with R^2 value of 44% for both SVM, higher than R^2 value of Linear and cubic SVM, which is both 43%. Also, RMSE is also calculated, RMSE is an error metric. The lower the value, the better predictive performance is. Table 4.3 shows the least RMSE value for Gaussian SVM, closely followed by quadratic SVM, both having a better predictive performance compared to Linear and cubic SVM, with both having the same RMSE value of 16.73. Figure 4.20, Figure 4.21, Figure 4.22, Figure 4.23 show the predicted vs response plot for linear, quadratic, cubic and Gaussian SVM, respectively. The black diagonal line represents how perfect prediction should be. The closest the blue points (observations) to the diagonal line, the better the model. For all our models, most of the points are located near the diagonal line. It can be observed that SVM algorithms have achieved an acceptable predictive accuracy compared to the percentage of data used. The accuracy of the prediction is not that high as observed from the R^2 value, which is below 50%. The major problem with gathering data for machine learning analysis in material science is high cost of gathering data, which can also be referred to as computational cost. It is well known that the higher the volume of the data the better, the performance. Therefore, larger datasets will be required for better accuracy, as stated in the work of Jing et al. [154].

Summary

It is worthy to state here that the ANN model and SVM models closely have the same value R^2 and MSE values. This shows models performed well, only hindered by the volume of the data.
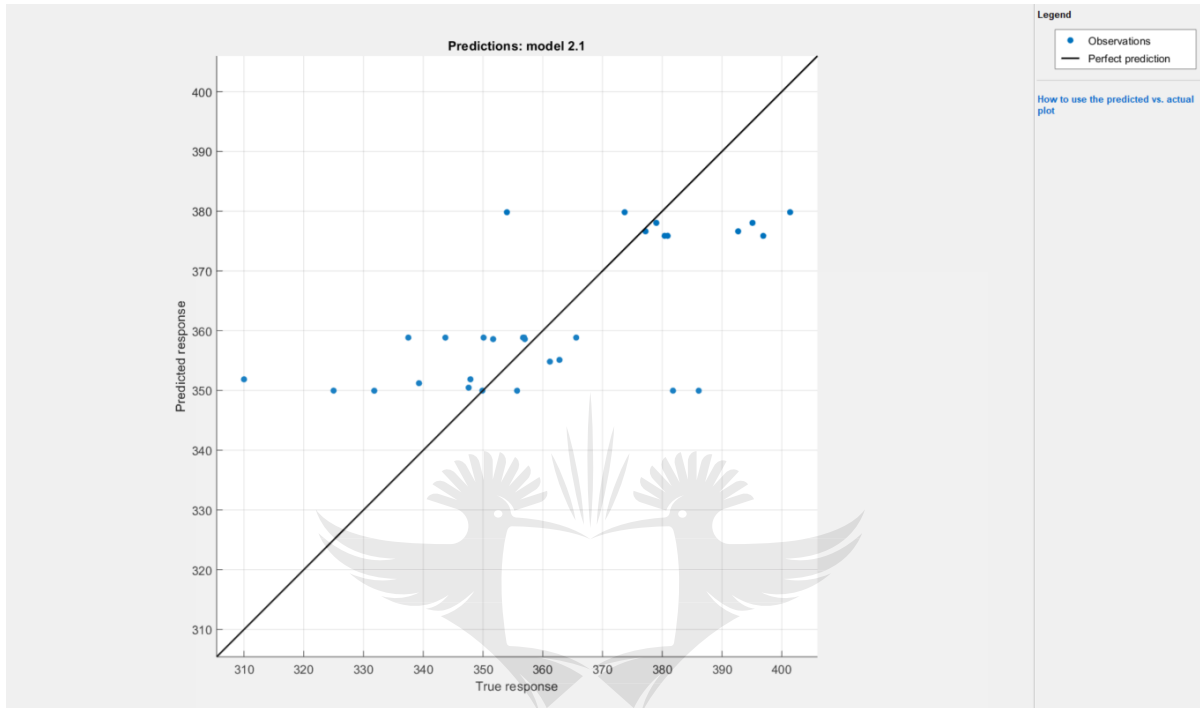
Figure 4.20: Predicted Vs. Actual Response (Linear SVM).

Table 4.7: Statistical parameters result

Kernel	RMSE	R^2	MSE	MAE
Linear SVM	16.73	0.43	279.93	12.497
Quadratic SVM	16.68	0.44	278.08	12.43
Cubic SVM	16.73	0.43	279.8	12.21
Gaussian SVM	16.67	0.44	277.9	12.198
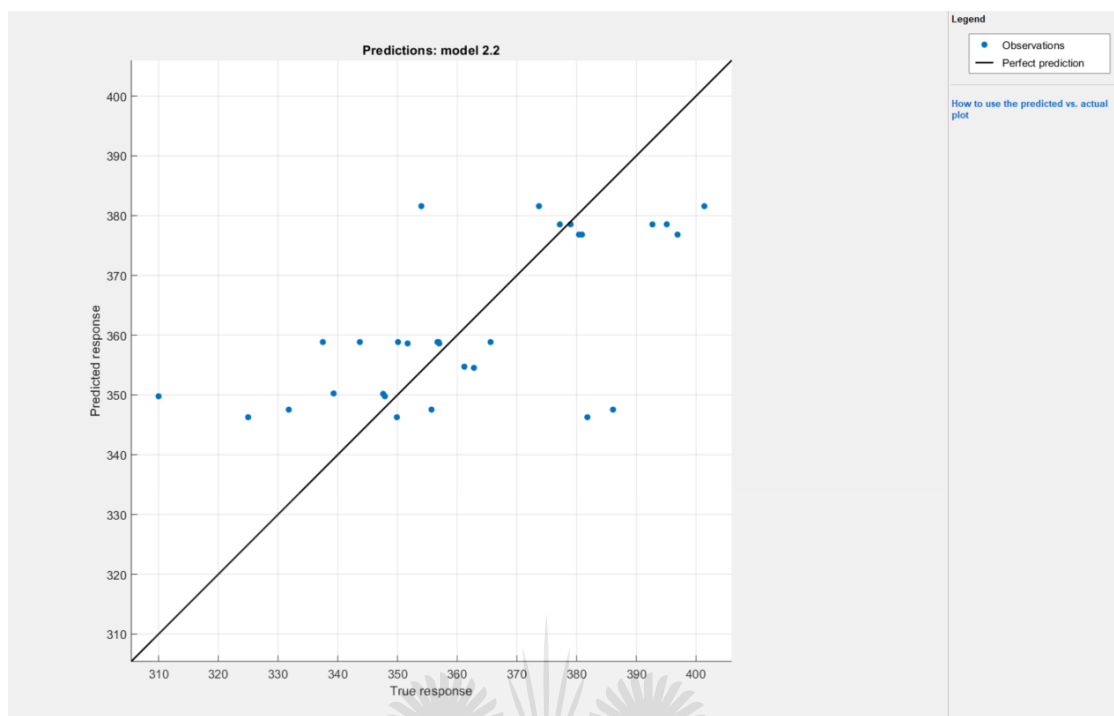
Figure 4.21: Predicted Vs. Actual Response (Quadratic SVM).
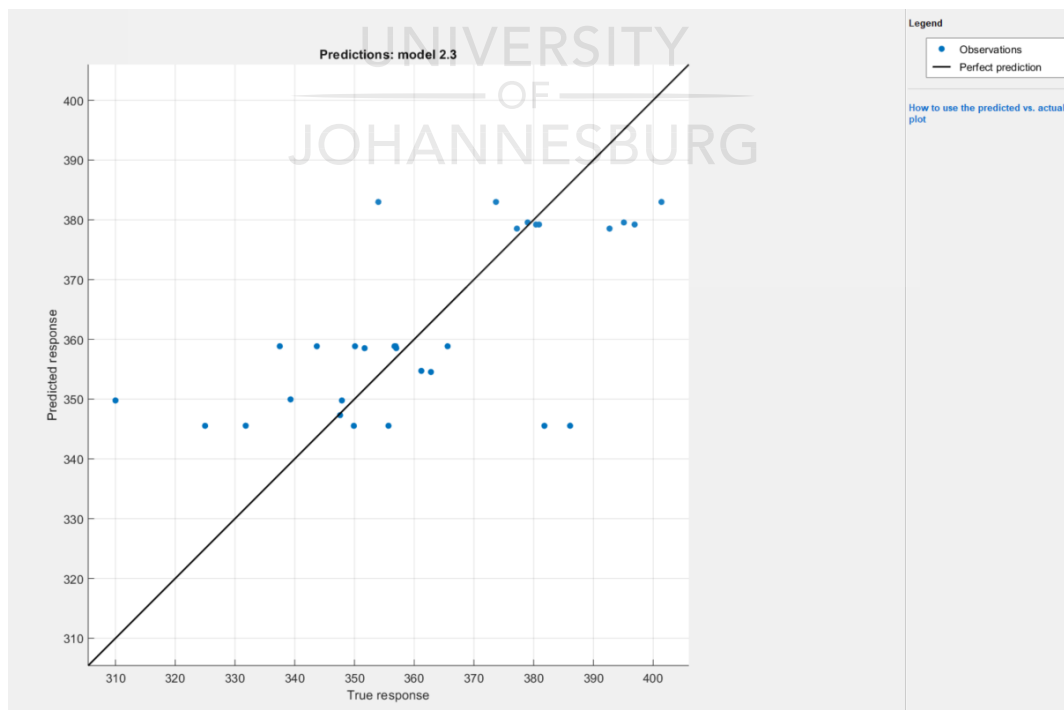
Figure 4.22: Predicted Vs. Actual Response (Cubic SVM).
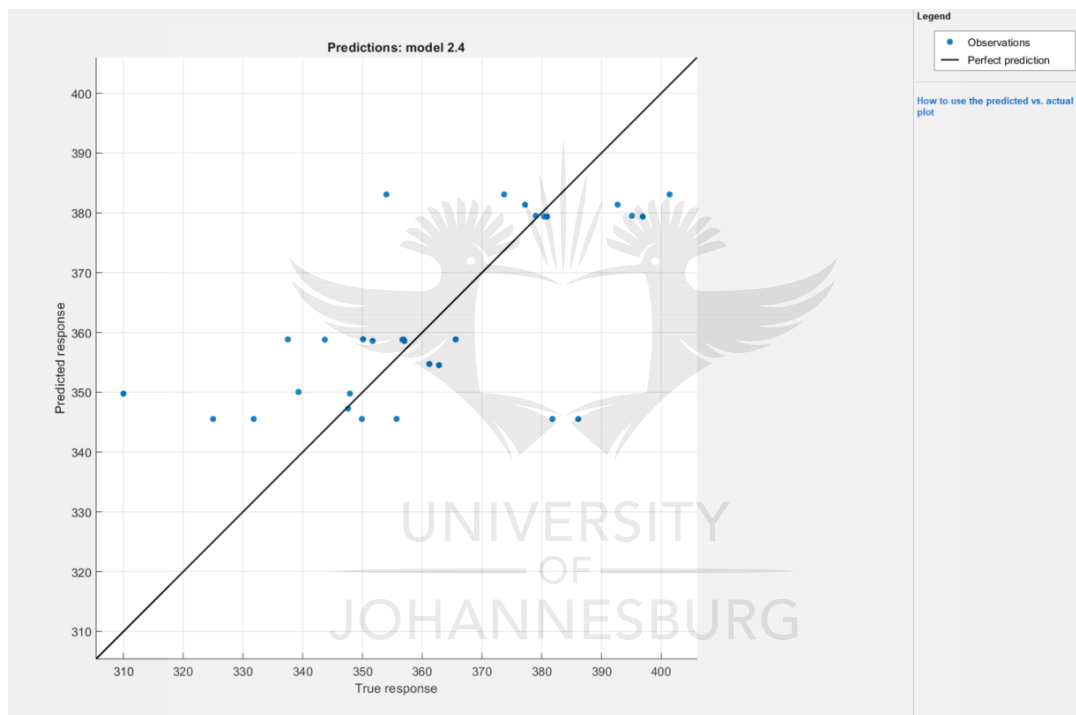
Figure 4.23: Predicted Vs. Actual Response (Gaussian SVM).

Chapter 5

Conclusion

5.1 Conclusion and potential future work

In this thesis, a new approach that aims to accelerate the data-driven discovery of materials properties was introduced. Machine learning algorithms supervised by fundamental materials science principles were developed to predict, and model vickers hardness of laser-welded 2507 DSS alloy. In working towards this objective, contributions were made to the field of machine learning application to materials properties predictions. This thesis provides a foundation for machine learning research on training materials science datasets and provides important lessons for both future researchers and practitioners in this field. The contributions include both experimental and theoretical analysis of the mechanical properties of metallic alloy for training in the machine learning algorithm.

5.1.1 Conclusion

Optimized sintering paramters

In the sintering experiment for 2507 alloy, different sintering parameters was used; at the end, it was possible to select the best sintering parameters that gave the least porosity, since the level of porosity in sintered material is an important factor in Laser welding. Therefore three samples with optimized properties was selected for

laser welding and machine learning analysis. The optimized sintering parameters for Samples A, B and C are 900 °C, 1000 °C, 1100 °C, sintering time that ranges between 5 min to 10 min, heating rate of 1000 °C/min and pressure of 50 MPa.

Hardness and Microstructural of the welded alloy

The hardness profile can be seen to be affected by the Laser power, and hardness values increase with a decrease in the laser power. However, high hardness at the WM zones for Samples A, B, and C can be due to the presence of a high amount of ferrite at that region. Microstructure phase analysis showed the presence of phases like δ ferrite, Cr_2N, and fine austenite inform of δ ferrite is noticed in the HAZ.

Machine learning model

Our approach was successfully applied and tested to predict the hardness properties of laser-welded 2507 DSS. The ANN predictive model was developed by using a neural network with RMS-prop optimizer and ReLU activation, which seems to be the best parameter selected. The hidden layer varied from 2 to 3 to predict hardness value. Through the linear regression analysis, it can be inferred that the predictive values and the real values deviated to some extent. Empirical examinations of the predicted hardness value (by comparing MSE, MAE metrics) shows that the proposed neural network has the advantage of improving the precision of predicting the hardness of the welded metallic alloy. It can be noticed that the evolution of MSE with the training and the test data of the ANN suggested no over-fitting of the ANN. However, top-notch performance of the ANN model cannot be guaranteed, as the R^2 gotten in the test data is greater than that of the training data. This may be due to the fact that there is not much numerical diversity in the input data used. Hence the anomalous values might be more noticeable in the training sets than the test sets, given their larger dimension when compared to the tests sets, which increases the R^2 value of the test sets. Forecasts of the hardness value were considered to be acceptable under the technological viewpoint. As stated earlier

in chapter four different activation functions and optimizers available under keras API was tested, ReLU and RMSProp respectively give the best optimized predicted values, with 2 and 3 hidden layers for ANN analysis. Meanwhile, for SVM, the best algorithm choice was made based on the kernel function used. Therefore in this research, the best kernel that gives the best values are Quadratic and Gaussian kernels. However, it will be suggested for anyone that may want to apply the model used in this research to use an increase number of data point for training, testing and validation process to enhance the reliability of the model and also improve predictive performance of the ANN model. The SVM model with different kernels closely give the value of the same metrics with the ANN model. This clearly shows that our models perform creditably well. It can be concluded that the SVM and ANN is an outstanding tool with a great potential in materials design. This research work proposes that full integration of analysis and prediction into one framework can be possible.

5.1.2   Future recommendations

This work has provided the foundation for the study of machine learning techniques in training materials properties data but is by no means exhausts the tendencies for more research in this area. This section highlighted some extensions of this work that could provide greater benefits for machine learning application to material science and for anyone that want to further explore this research in the nearest future.

Datasets

Obtaining appropriate and large datasets have been a major challenge in the application of machine learning to material science, has a large volume of training data improves the efficiency of the machine learning model and its predictive capabilities. Therefore, the cost of obtaining large datasets can be a stumbling block to successful machine learning application in material science field, which leave a considerable work to be done in future. Thus, an important area of consideration will

be the collection of new larger datasets. Larger datasets is known to pose additional complexities that machine learning algorithms such ANNs can utilize.

Machine learning models

Although this research covered some machine learning models out of several other machine learning algorithms that are commonly applied in the materials science field. It is therefore, suffice to say there are still more models left to be explored, for example, K-nearest Neighbor, Extreme Gradient Boosting, decision tree, Naives Bayes and DBSCAN.

Research Contributions

Peer-reviewed Journal publications can be found at Appendix A.C, and Appendix A

- Data on assessment and exploratory statistical correlation data analysis of sintered Nd:YAG laser welded 2507 duplex stainless steel August 2020 Data in Brief DOI: 10.1016/j.dib.2020.106201

- The synergy between powder metallurgy processes and welding of metallic alloy: a review. August 2020 Powder Metallurgy 63(4):254-267. DOI: 10.1080/00325899.2020.1807712

Bibliography

[1] K. Erhard and S. P. K, *Powder metallurgy stainless steels: processing, microstructures, and properties.* ASM international, 2007.

[2] G. Chail and P. Kangas, "Super and hyper duplex stainless steels: Structures, properties and applications," *Procedia Structural Integrity*, vol. 2, pp. 1755–1762, 2016.

[3] T. F. d. A. Santos, E. A. Torres, and A. J. Ramirez, "Friction stir welding of duplex stainless steels," *Welding international*, vol. 32, no. 2, pp. 103–111, 2018.

[4] A. Fedrizzi, M. Pellizzari, M. Zadra, and E. Marin, "Microstructural study and densification analysis of hot work tool steel matrix composites reinforced with tib2 particles," *Materials characterization*, vol. 86, pp. 69–79, 2013.

[5] R. Kolmorgen and H. Biermann, "Thermo-mechanical fatigue behaviour of a duplex stainless steel," *International journal of fatigue*, vol. 37, pp. 86–91, 2012.

[6] D. Chaira *et al.*, "Phase transformation and microstructure study of nanostructured austenitic and ferritic stainless steel powders prepared by planetary milling," *Powder technology*, vol. 259, pp. 125–136, 2014.

[7] Y. Han, D. Zou, Z. Chen, G. Fan, and W. Zhang, "Investigation on hot deformation behavior of 00cr23ni4n duplex stainless steel under medium–high strain rates," *Materials Characterization*, vol. 62, no. 2, pp. 198–203, 2011.

[8] P. Datta and G. Upadhyaya, "Sintered duplex stainless steels from premixes of 316l and 434l powders," *Materials chemistry and physics*, vol. 67, no. 1-3, pp. 234–242, 2001.

[9] L. Dobrzański, Z. Brytan, M. A. Grande, M. Rosso, and E. Pallavicini, "Properties of vacuum sintered duplex stainless steels," *Journal of Materials Processing Technology*, vol. 162, pp. 286–292, 2005.

[10] J. M. Dutkiewicz, W. Maziarz, T. Czeppe, L. Lityńska, W. Nowacki, S. Gadaj, J. Luckner, and E. Pieczyska, "Powder metallurgy technology of niti shape memory alloy," *The European Physical Journal Special Topics*, vol. 158, no. 1, pp. 59–65, 2008.

[11] M. Morakotjinda, N. Kuljittipipat, N. Poolthong, N. Tosangthum, P. Wila, R. Krataitong, T. Yodkaew, O. Coovattanachai, B. Vetayanugul, and R. Tongsri, "Sintered materials prepared from stainless steel series 300 and 400 powders," *Journal of Metals, Materials and Minerals*, vol. 18, no. 1, 2008.

[12] M. Rosso, M. A. Grande, and D. Ornato, "Sintering of duplex stainless steels and their properties," *Powder Metallurgy Progress*, vol. 2, no. 1, pp. 10–17, 2001.

[13] G. Cui and Z. Kou, "The effect of boron on mechanical behavior and microstructure for fe–cr matrix alloy prepared by p/m," *Journal of alloys and compounds*, vol. 586, pp. 699–702, 2014.

[14] A. Das and S. P. Harimkar, "Effect of graphene nanoplate and silicon carbide nanoparticle reinforcement on mechanical and tribological properties of spark plasma sintered magnesium matrix composites," *Journal of Materials Science & Technology*, vol. 30, no. 11, pp. 1059–1070, 2014.

[15] S. Diouf and A. Molinari, "Densification mechanisms in spark plasma sintering: Effect of particle size and pressure," *Powder technology*, vol. 221, pp. 220–227, 2012.

[16] J. Jain, A. M. Kar, and A. Upadhyaya, "Effect of yag addition on sintering of p/m 316l and 434l stainless steels," *Materials Letters*, vol. 58, no. 14, pp. 2037–2040, 2004.

[17] L. Cheng, Z. Xie, G. Liu, W. Liu, and W. Xue, "Densification and mechanical properties of tic by sps-effects of holding time, sintering temperature and pressure condition," *Journal of the European Ceramic society*, vol. 32, no. 12, pp. 3399–3406, 2012.

[18] X. Li, C. Liu, K. Luo, M. Ma, and R. Liu, "Hot deformation behaviour of sic/aa6061 composites prepared by spark plasma sintering," *Journal of Materials Science & Technology*, vol. 32, no. 4, pp. 291–297, 2016.

[19] R. Marder, R. Chaim, G. Chevallier, and C. Estournès, "Densification and polymorphic transition of multiphase y2o3 nanoparticles during spark plasma sintering," *Materials Science and Engineering: A*, vol. 528, no. 24, pp. 7200–7206, 2011.

[20] P. Drescher, K. Witte, B. Yang, R. Steuer, O. Kessler, E. Burkel, C. Schick, and H. Seitz, "Composites of amorphous and nanocrystalline zr–cu–al–nb bulk materials synthesized by spark plasma sintering," *Journal of Alloys and Compounds*, vol. 667, pp. 109–114, 2016.

[21] S.-J. Oh, D. Park, K. Kim, I.-J. Shon, and S.-J. Lee, "Austenite stability and mechanical properties of nanocrystalline fe–mn alloy fabricated by spark plasma sintering with variable mn content," *Materials Science and Engineering: A*, vol. 725, pp. 382–388, 2018.

[22] R. Chandramouli, T. Kandavel, and P. Karthikeyan, "Experimental investigations on welding behaviour of sintered and forged fe–0.3% c–3% mo low alloy steel," *Materials & Design*, vol. 53, pp. 645–650, 2014.

[23] ——, "Experimental investigations on welding characteristics of sinter-forged pre-alloy atomet 4601 steel," *The International Journal of Advanced Manufacturing Technology*, vol. 88, no. 1-4, pp. 1065–1074, 2017.

[24] C. Selcuk, "Joining processes for powder metallurgy parts," in *Advances in Powder Metallurgy*, Elsevier, 2013, pp. 380–398.

[25] E. O. Correa, "Weldability of iron based powder metal alloys using pulsed gtaw process," *Arc Welding*, pp. 109–126, 2011.

[26] J. Hamill, "Weld techniques give powder metal a different dimension," *Metal Powder Report*, vol. 62, no. 5, pp. 22–31, 2007.

[27] M. Fillabi, A. Simchi, and A. Kokabi, "Effect of iron particle size on the diffusion bonding of fe–5% cu powder compact to wrought carbon steels," *Materials & Design*, vol. 29, no. 2, pp. 411–417, 2008.

[28] K. Jayabharath, M. Ashfaq, P. Venugopal, and D. Achar, "Investigations on the continuous drive friction welding of sintered powder metallurgical (p/m) steel and wrought copper parts," *Materials Science and Engineering: A*, vol. 454, pp. 114–123, 2007.

[29] M. Suresh, B. Vamsi Krishna, P. Venugopal, and K. Prasad Rao, "Effect of pulse frequency in gas tungsten arc welding of powder metallurgical preforms," *Science and Technology of welding and joining*, vol. 9, no. 4, pp. 362–368, 2004.

[30] Ş. Talaş, M. Doğan, M. Çakmakkaya, and A. Kurt, "The effect of voltage on the arc stud welding of microwave sintered fe+ al powder mixture," *Materials Research*, vol. 17, no. 3, pp. 632–637, 2014.

[31] M. Wahba, Y. Kawahito, K. Kondoh, and S. Katayama, "A fundamental study of laser welding of hot extruded powder metallurgy (p/m) az31b magnesium alloy," *Materials Science and Engineering: A*, vol. 529, pp. 143–150, 2011.

[32] J. Schmidt, M. R. Marques, S. Botti, and M. A. Marques, "Recent advances and applications of machine learning in solid-state materials science," *npj Computational Materials*, vol. 5, no. 1, pp. 1–36, 2019.

[33] T. Mueller, A. G. Kusne, and R. Ramprasad, "Machine learning in materials science: Recent progress and emerging applications," *Reviews in Computational Chemistry*, vol. 29, pp. 186–273, 2016.

[34] S. Marsland, *Machine learning: an algorithmic perspective.* CRC press, 2015.

[35] C. Long, J. Hattrick-Simpers, M. Murakami, R. Srivastava, I. Takeuchi, V. L. Karen, and X. Li, "Rapid structural mapping of ternary metallic alloy systems using the combinatorial approach and cluster analysis," *Review of Scientific Instruments*, vol. 78, no. 7, p. 072 217, 2007.

[36] G. Pilania, C. Wang, X. Jiang, S. Rajasekaran, and R. Ramprasad, "Accelerating materials property predictions using machine learning," *Scientific reports*, vol. 3, no. 1, pp. 1–6, 2013.

[37] K. Hansen, G. Montavon, F. Biegler, S. Fazli, M. Rupp, M. Scheffler, O. A. Von Lilienfeld, A. Tkatchenko, and K.-R. Muller, "Assessment and validation of machine learning methods for predicting molecular atomization energies," *Journal of Chemical Theory and Computation*, vol. 9, no. 8, pp. 3404–3419, 2013.

[38] M. J. Faizabadi, G. Khalaj, H. Pouraliakbar, and M. R. Jandaghi, "Predictions of toughness and hardness by using chemical composition and tensile properties in microalloyed line pipe steels," *Neural Computing and Applications*, vol. 25, no. 7-8, pp. 1993–1999, 2014.

[39] A. Kurt, H. Ates, A. Durgutlu, and K. Karacif, "Exploring the weldability of powder metal parts," *Welding journal*, vol. 83, no. 12, pp. 34–37, 2004.

[40] F. Thümmler, R. Oberacker, *et al.*, *An introduction to powder metallurgy.* Institute of Materials London, 1993, vol. 490.

[41] J. K. L. Lai, C. H. Shek, and K. H. Lo, *Stainless steels: An introduction and their recent developments.* Bentham Science Publishers, 2012.

[42] D. Peckner, I. M. Bernstein, and D. Peckner, *Handbook of stainless steels.* McGraw-Hill New York, 1977.

[43] A. L. Schaeffler, "Constitution diagram for stainless steel weld metal," *Metal progress*, vol. 56, no. 11, p. 680, 1949.

[44] N. I. A. Haddad, "The development of microstructure in duplex stainless steel welds," PhD thesis, University of Cambridge, 1989.

[45] E. E. Dengiz, *Fiber laser welding of saf 2507 duplex stainless steel*, 2012.

[46] A. Sandvik, "Sandvik saf 2507," *Tube and pipe, seamless, Datasheet*, 2012.

[47] M. Liljas, P. Johansson, H.-P. Liu, and C.-O. A. Olsson, "Development of a lean duplex stainless steel," *steel research international*, vol. 79, no. 6, pp. 466–473, 2008.

[48] R. Gunn, *Duplex stainless steels: microstructure, properties and applications.* Elsevier, 1997.

[49] P. Schafmeister and R. Ergang, "Brittle sigma phase in three component fe-cr-mn system," *Arch. Eisenhüttenwes*, vol. 12, no. 10, pp. 507–510, 1939.

[50] H. D. Solomon and T. Devine Jr, "Duplex stainless steels–a tale of two phases," in *Duplex stainless steels*, 1982, pp. 693–756.

[51] L. Flasche, "Weldability of ferralium alloy 255," *Duplex Stainless Steels, Paper*, pp. 8201–028, 1983.

[52] T. A. Debold, "Duplex stainless steel—microstructure and properties," *JOM*, vol. 41, no. 3, pp. 12–15, 1989.

[53] J. Charles, "Proceedings conf. duplex stainless steels," *Beaune, France, Les editions de physique*, vol. 1, pp. 3–48, 1991.

[54] M. Qian and F. H. Froes, *Titanium powder metallurgy: science, technology and applications.* Butterworth-Heinemann, 2015.

[55] R. G. Narayanan, *Powder metallurgy-basic & aplication.*

[56] V. Shatokha, *Sintering: Methods and products.* BoD–Books on Demand, 2012.

[57] S.-J. L. Kang, *Sintering: densification, grain growth and microstructure.* Elsevier, 2004.

[58]   H. H. Hausner, *Iron powder metallurgy.* Metal Powder Industry, 1968, vol. 3.

[59]   S. Collins and P. Williams, "Electropolished tubing: Avoiding corrosion in welded applications-identifying optimum aisi 316l compositions," *Chemical Processing*, vol. 63, no. 12, pp. 33–36, 2000.

[60]   D. L. Dyke and H. D. Ambs, "Stainless steel powder metallurgy," *American Society for Metals, Powder Metallurgy–Applications, Advantages and Limitations,*, pp. 123–144, 1983.

[61]   S. Zhou, Y. Zhao, Z. Peng, and F. Ren, "The investigation of laser lap welding process on high-strength galvanized steel sheets," *International Scholarly Research Notices*, vol. 2011, 2011.

[62]   L. E. Stridh, "Laser hybrid welding in stainless steels and in high strength steels," in *Materials science forum*, Trans Tech Publ, vol. 539, 2007, pp. 3991–3995.

[63]   J. Sundqvist, "Heat conduction effects during laser welding," PhD thesis, Luleå tekniska universitet, 2015.

[64]   C. Lampa, I. Sarady, J. Powell, J. Mattson, and C. Magnusson, "Laser welding of dissimilar metals," in *Conf. Proc. of 4th Conf. on Laser Materials Processing in the Nordic Countries, NOLAMP*, 1993, pp. 215–224.

[65]   E. Kannatey-Asibu Jr, *Principles of laser materials processing.* John Wiley & Sons, 2009, vol. 4.

[66]   L. Quintino, A. Costa, R. Miranda, D. Yapp, V. Kumar, and C. Kong, "Welding with high power fiber lasers–a preliminary study," *Materials & Design*, vol. 28, no. 4, pp. 1231–1237, 2007.

[67]   I. Miyamoto, T. Kosumi, S.-J. Park, H. Uragishi, K. Watanabe, and T. Ooie, "Applications of single-mode fiber lasers to novel microwelding," in *Fifth International Symposium on Laser Precision Microfabrication*, International Society for Optics and Photonics, vol. 5662, 2004, pp. 507–514.

[68]   R. P. Martukanitz, "A critical review of laser beam welding," in *Critical Review: Industrial Lasers and Applications*, International Society for Optics and Photonics, vol. 5706, 2005, pp. 11–24.

[69]   S.-K. Cho, Y.-S. Yang, K.-J. Son, and J.-Y. Kim, "Fatigue strength in laser welding of the lap joint," *Finite Elements in analysis and design*, vol. 40, no. 9-10, pp. 1059–1070, 2004.

[70]   W. Steen, J. Dowden, M. Davis, and P. Kapadia, "A point and line source model of laser keyhole welding," *Journal of Physics D: Applied Physics*, vol. 21, no. 8, p. 1255, 1988.

[71]   M. Essien and P. Fuerschbach, "Beam characterization of a materials processing co2 laser," *Welding Journal-Including Welding Research Supplement*, vol. 75, no. 2, pp. 47–50, 1996.

[72]   L. Beckmann and D. Ehrlichmann, "Optical systems for high-power laser applications: Principles and design aspects," *Optical and quantum electronics*, vol. 27, no. 12, pp. 1407–1425, 1995.

[73]   J. Rapp, C. Glumann, F. Dausinger, and H. Hügel, "Laser welding of aluminium lightweight materials: Problems, solutions, readiness for application," *Optical and Quantum Electronics*, vol. 27, no. 12, pp. 1203–1211, 1995.

[74]   K. Abderrazak, W. Kriaa, W. B. Salem, H. Mhiri, G. Lepalec, and M. Autric, "Numerical and experimental studies of molten pool formation during an interaction of a pulse laser (nd: Yag) with a magnesium alloy," *Optics & Laser Technology*, vol. 41, no. 4, pp. 470–480, 2009.

[75]   F. M. Ghaini, M. Hamedi, M. Torkamany, and J. Sabbaghzadeh, "Weld metal microstructural characteristics in pulsed nd: Yag laser welding," *Scripta Materialia*, vol. 56, no. 11, pp. 955–958, 2007.

[76]   M. Hazratinezhad, N. M. Arab, A. Sufizadeh, and M. Torkamany, "Mechanical and metallurgical properties of pulsed neodymium-doped yttrium alu-

minum garnet laser welding of dual phase steels," *Materials & Design*, vol. 33, pp. 83–87, 2012.

[77] F. Mirakhorli, F. M. Ghaini, and M. Torkamany, "Development of weld metal microstructures in pulsed laser welding of duplex stainless steel," *Journal of materials engineering and performance*, vol. 21, no. 10, pp. 2173–2176, 2012.

[78] C. Seang, A. K. David, and E. Ragneau, "Effect of nd: Yag laser welding parameters on the hardness of lap joint: Experimental and numerical approach," *Physics Procedia*, vol. 41, pp. 38–40, 2013.

[79] Q. Sun, H.-S. Di, J.-C. Li, and X.-N. Wang, "Effect of pulse frequency on microstructure and properties of welded joints for dual phase steel by pulsed laser welding," *Materials & Design*, vol. 105, pp. 201–211, 2016.

[80] M. Pang, G. Yu, H.-H. Wang, and C.-Y. Zheng, "Microstructure study of laser welding cast nickel-based superalloy k418," *Journal of Materials Processing Technology*, vol. 207, no. 1-3, pp. 271–275, 2008.

[81] H. Park and S. Rhee, "Analysis of mechanism of plasma and spatter in co2 laser welding of galvanized steel," *Optics & Laser Technology*, vol. 31, no. 2, pp. 119–126, 1999.

[82] A. Kouadri and L. Barrallier, "Texture characterisation of hexagonal metals: Magnesium az91 alloy, welded by laser processing," *Materials Science and Engineering: A*, vol. 429, no. 1-2, pp. 11–17, 2006.

[83] J. Ion, *Laser processing of engineering materials: principles, procedure and industrial application*. Elsevier, 2005.

[84] H.-C. Chen, "Fibre laser welding of dissimilar materials," PhD thesis, The University of Manchester (United Kingdom), 2010.

[85] W. M. Steen and J. Mazumder, *Laser material processing*. springer science & business media, 2010.

[86] E. Schubert, M. Klassen, I. Zerner, C. Walz, and G. Sepold, "Light-weight structures produced by laser beam joining for future applications in automobile and aerospace industry," *Journal of Materials Processing Technology*, vol. 115, no. 1, pp. 2–8, 2001.

[87] L. Mei, G. Chen, X. Jin, Y. Zhang, and Q. Wu, "Research on laser welding of high-strength galvanized automobile steel sheets," *Optics and Lasers in Engineering*, vol. 47, no. 11, pp. 1117–1124, 2009.

[88] S. Hernández, *Laser welding of hardenable steel*, 2010.

[89] S. David and T. DebRoy, "Current issues and problems in welding science," *Science*, vol. 257, no. 5069, pp. 497–502, 1992.

[90] Z. Sun and J. Ion, "Laser welding of dissimilar metal combinations," *Journal of Materials Science*, vol. 30, no. 17, pp. 4205–4214, 1995.

[91] M. Peltonen *et al.*, "Weldability of high-strength steels using conventional welding methods," 2014.

[92] J. Kim, T. Watanabe, and Y. Yoshida, "Effect of the beam-defocusing characteristics on porosity formation in laser welding," *Journal of materials science letters*, vol. 14, no. 22, pp. 1624–1626, 1995.

[93] C. Kwok, S. Fong, F. Cheng, and H. Man, "Pitting and galvanic corrosion behavior of laser-welded stainless steels," *Journal of materials processing technology*, vol. 176, no. 1-3, pp. 168–178, 2006.

[94] P. Berger, H. Hügel, and T. Graf, "Understanding pore formation in laser beam welding," *Physics Procedia*, vol. 12, pp. 241–247, 2011.

[95] S. Katayama, M. Mizutani, and A. Matsunawa, "Development of porosity prevention procedures during laser welding," in *First International Symposium on High-Power Laser Macroprocessing*, International Society for Optics and Photonics, vol. 4831, 2003, pp. 281–288.

[96] J. Kristensen, L. Hansen, S. Neilsen, and K. Borggreen, "Laser welding of c-mn steels and duplex stainless steels'," in *Proc. Conf.'Assessment of Power Beam Welds', Geesthacht, Germany*, 1999, pp. 4–5.

[97] J. Russell, "Laser weldability of c-mn steels," *WELDING RESEARCH ABROAD*, vol. 47, no. 9/10, pp. 23–28, 2001.

[98] X. Yu, "Machine learning application in the life time of materials," *arXiv preprint arXiv:1707.04826*, 2017.

[99] A. Mangal, "Applied machine learning to predict stress hotspots in materials," PhD thesis, Carnegie Mellon University, 2018.

[100] C. M. Bishop, *Pattern recognition and machine learning.* springer, 2006.

[101] M. A. Shandiz and R. Gauvin, "Application of machine learning methods for the prediction of crystal system of cathode materials in lithium-ion batteries," *Computational Materials Science*, vol. 117, pp. 270–278, 2016.

[102] A. Géron, *Hands-on machine learning with Scikit-Learn, Keras, and Tensor-Flow: Concepts, tools, and techniques to build intelligent systems.* O'Reilly Media, 2019.

[103] A. Ethem, *Introduction to machine learning: Massachusetts institute of technology*, 2014.

[104] X. J. Zhu, "Semi-supervised learning literature survey," University of Wisconsin-Madison Department of Computer Sciences, Tech. Rep., 2005.

[105] F. Pedregosa, G. Varoquaux, A. Gramfort, V. Michel, B. Thirion, O. Grisel, M. Blondel, P. Prettenhofer, R. Weiss, V. Dubourg, *et al.*, "Scikit-learn: Machine learning in python," *the Journal of machine Learning research*, vol. 12, pp. 2825–2830, 2011.

[106] C. H. Tung, "Process-structure-property relationship and its impact on microelectronics device reliability and failure mechanism," *JOURNAL OF SEMICONDUCTOR TECHNOLOGY AND SCIENCE*, vol. 3, no. 3, pp. 107–113, 2003.

[107] H. Bhadeshia, D. MacKay, and L.-E. Svensson, "Impact toughness of c–mn steel arc welds–bayesian neural network analysis," *Materials Science and Technology*, vol. 11, no. 10, pp. 1046–1051, 1995.

[108] T. Dutta, S. Dey, S. Datta, and D. Das, "Designing dual-phase steels with improved performance using ann and ga in tandem," *Computational Materials Science*, vol. 157, pp. 6–16, 2019.

[109] H. Pouraliakbar, M.-j. Khalaj, M. Nazerfakhari, and G. Khalaj, "Artificial neural networks for hardness prediction of haz with chemical composition and tensile test of x70 pipeline steels," *Journal of Iron and Steel Research International*, vol. 22, no. 5, pp. 446–450, 2015.

[110] L. T. Ward, "Machine learning for materials discovery and design," PhD thesis, Northwestern University, 2017.

[111] V. Sotskov *et al.*, "Band gap prediction for inorganic crystals with machine learning," 2018.

[112] A. Delorme, "Genetic algorithm for optimization of mechanical properties," Technical report, University of Cambridge, Tech. Rep., 2003.

[113] D. F. Cha, H. Zhang, and M. Blumenstein, "Prediction of maximum wave-induced liquefaction in porous seabed using multi-artificial neural network model," *Ocean engineering*, vol. 38, no. 7, pp. 878–887, 2011.

[114] Y. LeCun, Y. Bengio, and G. Hinton, "Deep learning," *nature*, vol. 521, no. 7553, pp. 436–444, 2015.

[115] D. E. Goldberg, "Genetic algorithms in search," *Optimization, and Machine-Learning*, 1989.

[116] D. Whitley, "A genetic algorithm tutorial," *Statistics and computing*, vol. 4, no. 2, pp. 65–85, 1994.

[117] J. Holland, "Adaptation in natural and artificial systems: An introductory analysis with application to biology," *Control and artificial intelligence*, 1975.

[118] S. Steven, "Skiena, the algorithm design manual. springer," 2012.

[119] L. M. Howard and D. J. D'Angelo, "The ga-p: A genetic algorithm and genetic programming hybrid," *IEEE expert*, vol. 10, no. 3, pp. 11–15, 1995.

[120] X. Fang, "Engineering design using genetic algorithms," 2007.

[121] M. DeRousseau, J. Kasprzyk, and W. Srubar III, "Computational design optimization of concrete mixtures: A review," *Cement and Concrete Research*, vol. 109, pp. 42–53, 2018.

[122] R. Moraes, "Jo ao francisco valiati, and wilson p gavi ao neto. 2013. document-level sentiment classification: An empirical comparison between svm and ann," *Expert Systems with Applications*, vol. 40, p. 2, 2013.

[123] N. J. Vickers, "Animal communication: When i'm calling you, will you answer too?" *Current biology*, vol. 27, no. 14, R713–R715, 2017.

[124] O. Kisi, "Pan evaporation modeling using least square support vector machine, multivariate adaptive regression splines and m5 model tree," *Journal of Hydrology*, vol. 528, pp. 312–320, 2015.

[125] A. Zendehboudi, M. Baseer, and R. Saidur, *Application of support vector machine models for forecasting solar and wind energy resources: A review (2018).*

[126] W. B. Chaabene, M. Flah, and M. L. Nehdi, "Machine learning prediction of mechanical properties of concrete: Critical review," *Construction and Building Materials*, vol. 260, p. 119 889, 2020.

[127] A. Rabbani and S. Salehi, "Dynamic modeling of the formation damage and mud cake deposition using filtration theories coupled with sem image processing," *Journal of Natural Gas Science and Engineering*, vol. 42, pp. 157–168, 2017.

[128] P. Liu, G. Chen, P. Liu, and G. Chen, "Chapter two-making porous metals," *Porous Materials*, pp. 21–112, 2014.

[129] A. B962-08, *Standard test methods for density of compacted or sintered powder metallurgy (pm) products using archimedes' principle*, 2008.

[130] J. Rudy and E. Rupert, "Effects of porosity on mechanical properties of aluminum welds," *WELD J*, vol. 49, no. 7, p. 322, 1970.

[131] A. du Plessis, S. G. le Roux, and A. Guelpa, "The ct scanner facility at stellenbosch university: An open access x-ray computed tomography laboratory," *Nuclear Instruments and Methods in Physics Research Section B: Beam Interactions with Materials and Atoms*, vol. 384, pp. 42–49, 2016.

[132] G. Posch, J. Bruckner, and H. Ennsbrunner, "Industry 4.0 in welding," *Biuletyn Instytutu Spawalnictwa w Gliwicach*, vol. 62, 2018.

[133] A. T. Olanipekun, P. M. Mashinini, and N. B. Maledi, "Data on assessment and exploratory statistical correlation data analysis of sintered nd: Yag laser welded 2507 duplex stainless steel," *Data in brief*, vol. 32, p. 106 201, 2020.

[134] K. Balasubramanian, G. Buvanashekaran, and K. Sankaranarayanasamy, "Modeling of laser beam welding of stainless steel sheet butt joint using neural networks," *CIRP Journal of Manufacturing Science and Technology*, vol. 3, no. 1, pp. 80–84, 2010.

[135] B. K. Spears, J. Brase, P.-T. Bremer, B. Chen, J. Field, J. Gaffney, M. Kruse, S. Langer, K. Lewis, R. Nora, *et al.*, "Deep learning: A guide for practitioners in the physical sciences," *Physics of Plasmas*, vol. 25, no. 8, p. 080 901, 2018.

[136] M. Hansson and C. Olsson, "Feedforward neural networks with relu activation functions are linear splines," *Bachelor's Theses in Mathematical Sciences*, 2017.

[137] S. Ruder, "An overview of gradient descent optimization algorithms," *arXiv preprint arXiv:1609.04747*, 2016.

[138] G. R. Mohammed, M. Ishak, S. N. Aqida, and H. A. Abdulhadi, "Effects of heat input on microstructure, corrosion and mechanical characteristics of

welded austenitic and duplex stainless steels: A review," *Metals*, vol. 7, no. 2, p. 39, 2017.

[139] P. K. Kumar, N. V. Sai, and A. G. Krishna, "Influence of sintering conditions on microstructure and mechanical properties of alloy 218 steels by powder metallurgy route," *Arabian journal for science and engineering*, vol. 43, no. 9, pp. 4659–4674, 2018.

[140] V. D. Sánchez A, "Advanced support vector machines and kernel methods," *Neurocomputing*, vol. 55, no. 1-2, pp. 5–20, 2003.

[141] P. Batta, M. Singh, Z. Li, Q. Ding, and L. Trajković, "Evaluation of support vector machine kernels for detecting network anomalies," in *2018 IEEE International Symposium on Circuits and Systems (ISCAS)*, IEEE, 2018, pp. 1–4.

[142] B. Mouawad, D. Fabregue, M. Perez, M. Blat, F. Delabrouille, C. Domain, and C. Pokor, "Sintering of ferritic and austenitic nanopowders using spark plasma sintering," *Metallurgical Research & Technology*, vol. 111, no. 5, pp. 305–310, 2014.

[143] B. Gowon, K. S. Mohammed, S. B. B. Jamaluddin, Z. Hussain, P. Evarastics, *et al.*, "The effects of sintering temperature on the densification of mechanically alloyed w-brass composites," *Open Journal of Metal*, vol. 5, no. 03, p. 19, 2015.

[144] Y. Shi, Y. Hu, Y. Yi, S. Lin, and Z. Li, "Porosity and microstructure of underwater wet fcaw of duplex stainless steel," *Metallography, Microstructure, and Analysis*, vol. 6, no. 5, pp. 383–389, 2017.

[145] K. Sun, M. Zeng, Y. Shi, Y. Hu, and X. Shen, "Microstructure and corrosion behavior of s32101 stainless steel underwater dry and wet welded joints," *Journal of Materials Processing Technology*, vol. 256, pp. 190–201, 2018.

[146] E. M. Westin, "Microstructure and properties of welds in the lean duplex stainless steel ldx 2101," PhD thesis, KTH, 2010.

[147] Y. Zhang, C. Jia, B. Zhao, J. Hu, and C. Wu, "Heat input and metal transfer influences on the weld geometry and microstructure during underwater wet fcaw," *Journal of Materials Processing Technology*, vol. 238, pp. 373–382, 2016.

[148] K. Bettahar, M. Bouabdallah, R. Badji, M. Gaceb, C. Kahloun, and B. Bacroix, "Microstructure and mechanical behavior in dissimilar 13cr/2205 stainless steel welded pipes," *Materials & Design*, vol. 85, pp. 221–229, 2015.

[149] N. McPherson, Y. Li, and T. Baker, "Microstructure and properties of as welded duplex stainless steel," *Science and technology of welding and joining*, vol. 5, no. 4, pp. 235–244, 2000.

[150] E. Capello, P. Chiarello, B. Previtali, and M. Vedani, "Laser welding and surface treatment of a 22cr–5ni–3mo duplex stainless steel," *Materials Science and Engineering: A*, vol. 351, no. 1-2, pp. 334–343, 2003.

[151] E. M. Westin, K. Stelling, and A. Gumenyuk, "Single-pass laser-gma hybrid welding of 13.5 mm thick duplex stainless steel," *Welding in the World*, vol. 55, no. 1-2, pp. 39–49, 2011.

[152] L. Jiang, N. Chawla, M. Pacheco, and V. Noveski, "Three-dimensional (3d) microstructural characterization and quantification of reflow porosity in sn-rich alloy/copper joints by x-ray tomography," *Materials characterization*, vol. 62, no. 10, pp. 970–975, 2011.

[153] H. Pouraliakbar, A. H. Monazzah, R. Bagheri, S. S. Reihani, G. Khalaj, A. Nazari, and M. Jandaghi, "Toughness prediction in functionally graded al6061/sicp composites produced by roll-bonding," *Ceramics International*, vol. 40, no. 6, pp. 8809–8825, 2014.

[154] J. Wei, X. Chu, X.-Y. Sun, K. Xu, H.-X. Deng, J. Chen, Z. Wei, and M. Lei, "Machine learning in materials science," *InfoMat*, vol. 1, no. 3, pp. 338–358, 2019.

Appendix A

Python and Matlab Code with Appended Publications

Appendix A.A   :ANN code

```python
1  # -*- coding: utf-8 -*-
2  """ANNhardness.ipynb
3
4  Automatically generated by Colaboratory.
5
6  Original file is located at
7      https://colab.research.google.com/github/AyorindeTayo/ANN-
      prediction-of-Hardness-using-Tensor-Flow/blob/master/ANNhardness
      .ipynb
8  """
9
10 import tensorflow as tf
11 import numpy as np
12 import pandas as pd
13 import seaborn as sns
14 import matplotlib.pyplot as plt
15 from tensorflow import keras
16
17 print(tf.__version__)
```

```python
18

19 !pip install git+https://github.com/tensorflow/docs

20

21 """# A quick exploratory data analysis"""

22

23 from google.colab import files
24 files.upload()

25

26 df=pd.read_excel('data_1004.xlsx')
27 df.head()

28

29 plt.plot(df.index, df['Hardness'], color='r', lw=2, label='dataset'
       )
30 plt.xlabel('Experiments')
31 plt.ylabel('Hardness')
32 plt.legend()
33 plt.show()

34

35 """# Preparation of the data for training"""

36

37 train_dataset = df.sample(frac=0.8,random_state=0)
38 test_dataset = df.drop(train_dataset.index)

39

40 train_stats = train_dataset.describe()
41 train_stats.pop("Hardness")
42 train_stats = train_stats.transpose()
43 train_stats

44

45 train_labels = train_dataset.pop('Hardness')
46 test_labels = test_dataset.pop('Hardness')

47

48 """# Defining the function to normalize the data"""

49

50 def norm(x):
51   return (x - train_stats['mean']) / train_stats['std']
```

```python
52 normed_train_data = norm(train_dataset)
53 normed_test_data = norm(test_dataset)
54
55 """# Defining the shallow neural network model"""
56
57 def build_model():
58   model = keras.Sequential([
59     keras.layers.Dense(64, activation='relu', input_shape=[len(
     train_dataset.keys())]),
60     keras.layers.Dense(64, activation='relu'),
61     keras.layers.Dense(1)
62   ])
63
64   optimizer = tf.keras.optimizers.RMSprop(0.001)
65
66   model.compile(loss='mse',
67                 optimizer=optimizer,
68                 metrics=['mae', 'mse'])
69   return model
70
71 model = build_model()
72
73 """# Training and validation of the model"""
74
75 import tensorflow_docs as tfdocs
76 import tensorflow_docs.plots
77 import tensorflow_docs.modeling
78
79 EPOCHS = 1000
80
81 history = model.fit(
82   normed_train_data, train_labels,
83   epochs=EPOCHS, validation_split = 0.2, verbose=0,
84   callbacks=[tfdocs.modeling.EpochDots()])
85
```

```
86  """# Learning and validation results"""

87

88  hist = pd.DataFrame(history.history)

89  hist['epoch'] = history.epoch

90  hist.tail()

91

92  """# Plotting the results"""

93

94  plotter = tfdocs.plots.HistoryPlotter(smoothing_std=3)

95

96  plotter.plot({'Basic': history}, metric = 'mae')

97  plt.ylim([0, 500])

98  plt.ylabel('MAE [Hardness]')    #mean_absolute_error

99

100 #plt.savefig('1.pdf')

101

102 #files.download('1.pdf')

103

104 plotter.plot({'Basic': history}, metric = 'mse')

105 plt.ylim([0, 20000])

106 plt.ylabel('MSE [Hardness]') #mean_squared_error

107

108 #plt.savefig('2.pdf')

109

110 #files.download('2.pdf')

111

112 loss, mae, mse = model.evaluate(normed_train_data, train_labels,
        verbose=2)

113

114 print("Training Mean Abs Error: {:5.2f} Hardness".format(mae))

115

116 loss, mae, mse = model.evaluate(normed_test_data, test_labels,
        verbose=2)

117

118 print("Testing set Mean Abs Error: {:5.2f} Hardness".format(mae))
```

```
119
120  train_predictions = model.predict(normed_train_data).flatten()
121
122  a = plt.axes(aspect='equal')
123  plt.scatter(train_labels, train_predictions)
124  plt.xlabel('True Values [Hardness]')
125  plt.ylabel('Predictions [Hardness]')
126  lims = [0, 1000]
127  plt.xlim(lims)
128  plt.ylim(lims)
129  _ = plt.plot(lims, lims)
130
131  #plt.savefig('3.pdf')
132
133  #files.download('3.pdf')
134
135  test_predictions = model.predict(normed_test_data).flatten()
136
137  a = plt.axes(aspect='equal')
138  plt.scatter(test_labels, test_predictions)
139  plt.xlabel('True Values [Hardness]')
140  plt.ylabel('Predictions [Hardness]')
141  lims = [0, 1000]
142  plt.xlim(lims)
143  plt.ylim(lims)
144  _ = plt.plot(lims, lims)
145
146  #plt.savefig('4.pdf')
147
148  #files.download('4.pdf')
149
150  t1=np.corrcoef(test_labels, test_predictions)[0,1]
151  k1=np.corrcoef(train_labels, train_predictions)[0,1]
152  print('the corralation on the training set is',t1,'and that on the
          test set is',k1)
```

```
153
154 train_pred = model.predict(normed_train_data).flatten()
155 test_pred = model.predict(normed_test_data).flatten()
156
157 err1 = 100*(np.abs(test_pred - test_labels))/test_labels
158 err2=100*(np.abs(train_pred - train_labels))/train_labels
159
160 print(test_labels)
161 print('-'*50)
162 print(test_pred)
163 print('-'*50)
164 print(err1)
165
166 print(train_labels)
167 print('-'*50)
168 print(train_pred)
169 print('-'*50)
170 print(err2)
171
172 """# Model with early stopping"""
173
174 model1 = build_model()
175
176 # The patience parameter is the amount of epochs to check for
        improvement
177 early_stop = keras.callbacks.EarlyStopping(monitor='val_loss',
      patience=10)
178
179 early_history = model1.fit(normed_train_data, train_labels,
180                    epochs=EPOCHS, validation_split = 0.2, verbose
      =0,
181                    callbacks=[early_stop, tfdocs.modeling.
      EpochDots()])
182
183 """# Results of the model with early stopping"""
```

```
184
185 plotter.plot({'Early Stopping': early_history}, metric = "mae")
186 plt.ylim([0, 500])
187 plt.ylabel('MAE [Hardness]') #mean_absolute_error
188
189 plt.savefig('5.pdf')
190
191 files.download('5.pdf')
192
193 plotter.plot({'Early Stopping': early_history}, metric = "mse")
194 plt.ylim([0, 200000])
195 plt.ylabel('MSE [Hardness]') #mean_squared_error
196
197 plt.savefig('6.pdf')
198
199 files.download('6.pdf')
200
201 """# Training loss"""
202
203 loss, mae, mse = model1.evaluate(normed_train_data, train_labels,
        verbose=2)
204
205 print("Training set Mean Abs Error: {:5.2f} Hardness".format(mae))
206
207 """# Test loss"""
208
209 loss, mae, mse = model1.evaluate(normed_test_data, test_labels,
        verbose=2)
210
211 print("Testing set Mean Abs Error: {:5.2f} Hardness".format(mae))
212
213 """# Training plot"""
214
215 train_predictions = model1.predict(normed_train_data).flatten()
216
```

```
217 a = plt.axes(aspect='equal')

218 plt.scatter(train_labels, train_predictions)

219 plt.xlabel('True Values [Hardness]')

220 plt.ylabel('Predictions [Hardness]')

221 lims = [0, 1000]

222 plt.xlim(lims)

223 plt.ylim(lims)

224 _ = plt.plot(lims, lims)

225

226 plt.savefig('7.pdf')

227

228 files.download('7.pdf')

229

230 """# Test plot"""

231

232 test_predictions = model1.predict(normed_test_data).flatten()

233

234 a = plt.axes(aspect='equal')

235 plt.scatter(test_labels, test_predictions)

236 plt.xlabel('True Values [Hardness]')

237 plt.ylabel('Predictions [Hardness]')

238 lims = [0, 1000]

239 plt.xlim(lims)

240 plt.ylim(lims)

241 _ = plt.plot(lims, lims)

242

243 plt.savefig('8.pdf')

244

245 files.download('8.pdf')

246

247 test_predictions

248

249 """# Corralation coefficient"""

250

251 t=np.corrcoef(test_labels, test_predictions)[0,1]
```

```
252 k=np.corrcoef(train_labels, train_predictions)[0,1]
253 print('the corralation on the training set is',t,'and that on the
        test set is',k)
254
255 """# Percentage Errors on the predictions
256
257 The percentage error is defined as follows:
258
259 $$PE= 100\times \Big| \dfrac{TV-PV}{TV}\Big |$$
260
261 Where $TV$, $PV$ are the true values and the predicted value
        respectively.
262 """
263
264 error1 = 100*(np.abs(test_predictions - test_labels))/test_labels
265 error2=100*(np.abs(train_predictions - train_labels))/train_labels
266
267 print(test_labels)
268 print('-'*50)
269 print(test_predictions)
270 print('-'*50)
271 print(error1)
272
273 print(train_labels)
274 print('-'*50)
275 print(train_predictions)
276 print('-'*50)
277 print(error2)
278
279 test_predictions
280
281 """# Trying something"""
282
283 k=pd.Series(train_labels).reset_index(drop=True)
284 m=pd.Series(train_predictions).reset_index(drop=True)
```

```
285
286  plt.plot(k.index, k, color='green',marker='o', label='True values',
         lw=1)
287  plt.plot(m.index,m, 'bo', label='Predictions')
288  plt.legend()
289  plt.xlabel('Experiments')
290  plt.ylabel('Hardness')
291  plt.show()
292
293  l=pd.Series(test_labels).reset_index(drop=True)
294  n=pd.Series(test_predictions).reset_index(drop=True)
295
296  plt.plot(l.index, l, color='green',marker='o', label='True values',
         lw=1)
297  plt.plot(n.index,n, 'bo', label='Predictions')
298  plt.legend()
299  plt.xlabel('Experiments')
300  plt.ylabel('Hardness')
301  plt.show()
302
303  d_f=pd.concat([pd.Series(train_predictions),pd.Series(
         test_predictions)])
304
305  plt.plot(df.index, df['Hardness'], color='r', label='dataset', lw
         =2)
306  plt.plot(df.index, d_f, 'bo', label='overall predictions')
307  plt.xlabel('Experiments')
308  plt.ylabel('Hardness')
309  plt.legend()
310  plt.show()
311
312  dff=pd.concat([pd.Series(train_labels),pd.Series(test_labels)])
313  plt.scatter(d_f, dff, color='r', label='dataset')
314
315
```

```
316  #plt.savefig('test.pdf')

317

318  #files.download('test.pdf')

319

320  def build_modell():

321    model = keras.Sequential([

322      keras.layers.Dense(64, activation='relu', input_shape=[len(
       train_dataset.keys())]),

323      keras.layers.Dense(64, activation='relu',kernel_regularizer=tf.
       keras.regularizers.l2(0.01),

324      activity_regularizer=tf.keras.regularizers.l2(0.01)),

325      keras.layers.Dense(1)

326    ])

327

328    optimizer = tf.keras.optimizers.RMSprop(0.001)

329

330    model.compile(loss='mse',

331                  optimizer=optimizer,

332                  metrics=['mae', 'mse'])

333    return model

334

335

336

337

338  model2 = build_modell()

339

340  # The patience parameter is the amount of epochs to check for
       improvement

341  early_stop = keras.callbacks.EarlyStopping(monitor='val_loss',
       patience=10)

342

343  early_history = model1.fit(normed_train_data, train_labels,

344                    epochs=EPOCHS, validation_split = 0.2, verbose
       =0,

345                    callbacks=[tfdocs.modeling.EpochDots()])
```

```
346
347 loss, mae, mse = model2.evaluate(normed_train_data, train_labels,
        verbose=2)
348
349 print("Training set Mean Abs Error: {:5.2f} Hardness".format(mae))
350
351 print(history.history.keys())
352 # "Loss"
353 plt.plot(history.history['loss'])
354 plt.plot(history.history['val_loss'])
355 plt.title('model loss')
356 plt.ylabel('loss')
357 plt.xlabel('epoch')
358 plt.legend(['train', 'validation'], loc='upper left')
359 plt.show()
360
361 from sklearn.metrics import r2_score
362
363 r2_score(test_labels , test_predictions)
364
365 r2_score(train_labels, train_predictions)
366
367 Validation_data=(test_labels,test_predictions )
368
369 print(Validation_data)
370
371 Validation predictions = model1.predict(normed_test_data).flatten()
372
373 a = plt.axes(aspect='equal')
374 plt.scatter(test_labels, test_pred)
375 plt.xlabel('True Values [Hardness]')
376 plt.ylabel('Predictions [Hardness]')
377 lims = [0, 1000]
378 plt.xlim(lims)
379 plt.ylim(lims)
```

```
380 _ = plt.plot(lims, lims)

381

382

383 plt.savefig('8.pdf')

384

385 files.download('8.pdf')

386

387 import numpy

388

389

390 import matplotlib.pyplot
391 from sklearn.preprocessing import StandardScaler
392 from sklearn.model_selection import train_test_split
393 numpy.random.seed(78)

394

395 import pandas as pd

396

397 weldingdata=pd.read_excel('data_1004.xlsx')
398 df=weldingdata

399

400 from sklearn.model_selection import train_test_split
401 from sklearn.linear_model import LinearRegression

402

403 from sklearn import metrics

404

405

406 X=df[['S-temp','S-time', 'Wel-power', 'Wel-speed']]
407 y=df['Hardness']
```

Appendix A.B   :SVM code

```
1 function [trainedModel, validationRMSE] = trainRegressionModel(
    trainingData)
2 % [trainedModel, validationRMSE] = trainRegressionModel(
    trainingData)
```

```
3  % returns a trained regression model and its RMSE. This code
       recreates the
4  % model trained in Regression Learner app. Use the generated code
       to
5  % automate training the same model with new data, or to learn how
       to
6  % programmatically train models.
7  %
8  %  Input:
9  %      trainingData: a table containing the same predictor and
       response
10 %       columns as imported into the app.
11 %
12 %  Output:
13 %      trainedModel: a struct containing the trained regression
       model. The
14 %       struct contains various fields with information about the
       trained
15 %       model.
16 %
17 %      trainedModel.predictFcn: a function to make predictions on
       new data.
18 %
19 %      validationRMSE: a double containing the RMSE. In the app,
       the
20 %       History list displays the RMSE for each model.
21 %
22 % Use the code to train the model with new data. To retrain your
       model,
23 % call the function from the command line with your original data
       or new
24 % data as the input argument trainingData.
25 %
26 % For example, to retrain a regression model trained with the
       original data
```

```matlab
27 % set T, enter:
28 %    [trainedModel, validationRMSE] = trainRegressionModel(T)
29 %
30 % To make predictions with the returned 'trainedModel' on new data
       T2, use
31 %    yfit = trainedModel.predictFcn(T2)
32 %
33 % T2 must be a table containing at least the same predictor columns
        as used
34 % during training. For details, enter:
35 %    trainedModel.HowToPredict
36
37 % Auto-generated by MATLAB on 06-Dec-2020 20:03:26
38
39
40 % Extract predictors and response
41 % This code processes the data into the right shape for training
       the
42 % model.
43 inputTable = trainingData;
44 predictorNames = {'Stemp', 'Stime', 'Welpower', 'Welspeed'};
45 predictors = inputTable(:, predictorNames);
46 response = inputTable.Hardness;
47 isCategoricalPredictor = [false, false, false, false];
48
49 % Train a regression model
50 % This code specifies all the model options and trains the model.
51 responseScale = iqr(response);
52 if ~isfinite(responseScale) || responseScale == 0.0
53     responseScale = 1.0;
54 end
55 boxConstraint = responseScale/1.349;
56 epsilon = responseScale/13.49;
57 regressionSVM = fitrsvm(...
58     predictors, ...
```

```matlab
59      response, ...
60      'KernelFunction', 'gaussian', ...
61      'PolynomialOrder', [], ...
62      'KernelScale', 0.5, ...
63      'BoxConstraint', boxConstraint, ...
64      'Epsilon', epsilon, ...
65      'Standardize', true);
66
67  % Create the result struct with predict function
68  predictorExtractionFcn = @(t) t(:, predictorNames);
69  svmPredictFcn = @(x) predict(regressionSVM, x);
70  trainedModel.predictFcn = @(x) svmPredictFcn(predictorExtractionFcn
        (x));
71
72  % Add additional fields to the result struct
73  trainedModel.RequiredVariables = {'Stemp', 'Stime', 'Welpower', '
        Welspeed'};
74  trainedModel.RegressionSVM = regressionSVM;
75  trainedModel.About = 'This struct is a trained model exported from
        Regression Learner R2018a.';
76  trainedModel.HowToPredict = sprintf('To make predictions on a new
        table, T, use: \n  yfit = c.predictFcn(T) \nreplacing ''c'' with
         the name of the variable that is this struct, e.g. ''
        trainedModel''. \n \nThe table, T, must contain the variables
        returned by: \n  c.RequiredVariables \nVariable formats (e.g.
        matrix/vector, datatype) must match the original training data.
        \nAdditional variables are ignored. \n \nFor more information,
        see <a href="matlab:helpview(fullfile(docroot, ''stats'', ''
        stats.map''), ''appregression_exportmodeltoworkspace'')">How to
        predict using an exported model</a>.');
77
78  % Extract predictors and response
79  % This code processes the data into the right shape for training
        the
80  % model.
```

```matlab
81  inputTable = trainingData;

82  predictorNames = {'Stemp', 'Stime', 'Welpower', 'Welspeed'};

83  predictors = inputTable(:, predictorNames);

84  response = inputTable.Hardness;

85  isCategoricalPredictor = [false, false, false, false];

86

87  % Perform cross-validation

88  KFolds = 5;

89  cvp = cvpartition(size(response, 1), 'KFold', KFolds);

90  % Initialize the predictions to the proper sizes

91  validationPredictions = response;

92  for fold = 1:KFolds

93      trainingPredictors = predictors(cvp.training(fold), :);

94      trainingResponse = response(cvp.training(fold), :);

95      foldIsCategoricalPredictor = isCategoricalPredictor;

96

97      % Train a regression model

98      % This code specifies all the model options and trains the
        model.

99      responseScale = iqr(trainingResponse);

100     if ~isfinite(responseScale) || responseScale == 0.0

101         responseScale = 1.0;

102     end

103     boxConstraint = responseScale/1.349;

104     epsilon = responseScale/13.49;

105     regressionSVM = fitrsvm(...

106         trainingPredictors, ...

107         trainingResponse, ...

108         'KernelFunction', 'gaussian', ...

109         'PolynomialOrder', [], ...

110         'KernelScale', 0.5, ...

111         'BoxConstraint', boxConstraint, ...

112         'Epsilon', epsilon, ...

113         'Standardize', true);

114
```

```matlab
115    % Create the result struct with predict function
116    svmPredictFcn = @(x) predict(regressionSVM, x);
117    validationPredictFcn = @(x) svmPredictFcn(x);
118
119    % Add additional fields to the result struct
120
121    % Compute validation predictions
122    validationPredictors = predictors(cvp.test(fold), :);
123    foldPredictions = validationPredictFcn(validationPredictors);
124
125    % Store predictions in the original order
126    validationPredictions(cvp.test(fold), :) = foldPredictions;
127 end
128
129 % Compute validation RMSE
130 isNotMissing = ~isnan(validationPredictions) & ~isnan(response);
131 validationRMSE = sqrt(nansum(( validationPredictions - response )
       .^2) / numel(response(isNotMissing) ));
```

Appendix A.C   :The Synergy between powder metallurgy processes and welding of metallic alloy

The synergy between powder metallurgy processes and welding of metallic alloy: a review

Ayorinde Tayo Olanipekun , Nthabiseng Beauty Maledi & Peter Madindwa Mashinini

Published online: 19 Aug 2020.

Submit your article to this journal ⬈

Article views: 139

View related articles ⬈

View Crossmark data ⬈

IOm³

The Institute of Materials, Minerals and Mining

Taylor & Francis
Taylor & Francis Group

REVIEW

Check for updates

The synergy between powder metallurgy processes and welding of metallic alloy: a review

Ayorinde Tayo Olanipekun [a], Nthabiseng Beauty Maledi [b] and Peter Madindwa Mashinini [a]

aDepartment of Mechanical and Industrial Engineering, University of Johannesburg, Johannesburg, South Africa; bSchool of Chemical and Metallurgical Engineering, University of the Witwatersrand, Johannesburg, South Africa

ABSTRACT
Powder metallurgy (PM) technology is an ideal manufacturing process to produce near net shape parts i.e. part that requires little or no machining, examples of PM processes are spark plasma sintering, isostatic pressing and additive manufacturing. PM allows maximisation of materials and produces part with optimised mechanical and physical properties. Also, PM process provides the possibility to further increase the industrial use of PM parts by fabricating it into complex geometrical shapes via joining. Joining is the most important mechanical process necessary for PM parts to perform in actual service conditions expected in automobile parts and structural parts. Despite apparent advantages of PM processes, joining PM parts has been a tedious process, due to challenges associated with inherent characteristics, like porosity, chemical composition and impurities like oil or grease, which tend to impair the weldments property. In this document, a review of PM process is presented, focusing on different welding methods that can be used to effectively join PM components.

1. Introduction

Powder Metallurgy (PM) process can be described as a rapid, economical and high-volume production method for making high precision components from powder material [1].

PM provides the possibility of fabricating metallic alloy to near net shape, also more importantly avoiding issues associated with traditional manufacturing. Traditional manufacturing processes can be distinguished viz: casting, forging, rolling, machining and extrusion. Parts produced by traditional manufacturing processes are usually characterised by the precipitation of secondary and intermetallic phases along the grain boundary. The variation in the thermal decomposition of various phases present in the metallic alloy usually have a detrimental effect on the metallic alloy [2,3].

PM has enjoyed diverse applications in many industrial sectors, automobile applications, in the medical field as implants and dental restoration due to their good balance between corrosion resistance, impact strength and tensile strength [4,5].

PM process produces near net shape parts, i.e. parts requiring little or no machining. However, the economic aspect in terms of producing multi parts endears PM parts to find usage in a diverse range of engineering applications, necessitating joining of different PM parts together using welding technology. Also, joining is one of the mechanical processes necessary for PM parts to

perform in actual service conditions most importantly in the automobile industry and for structural parts. Keeping in mind that these parts are often joined to similar and dissimilar materials as non-detached components. Therefore, the weldability of the PM components must be insured [6,7].

Nevertheless, the weldability of PM metallic alloy varies with density and porosity. The pores act as a thermal insulator, reducing the thermal conductivity, and causes low hardenability, also the pores traps impurity such as oil or grease, eventually resulting in solidification cracking in the weld, which negatively affects the mechanical property of the welded metallic material. Additionally, the microstructure of the weld is principally determined by the production process employed, the grain size and the chemical composition of the metallic alloy [8–12]. The following factors are important in determining microstructural and mechanical properties of PM parts, namely: microstructure, composition (alloy and micro-alloy elements percentage), size and shape of the pore, sintering conditions, heat input and cooling rates. The aforementioned factors must be considered to achieve a better-welded joint. The microstructural complexities and peculiarity of PM produced metallic alloy should not change the precautions to be observed in the fusion welding process, the precautions observed for fusion welding of cast, extruded and wrought materials should also be applicable to PM parts [13].

CONTACT Ayorinde Tayo Olanipekun ✉ atolanipekun@uj.ac.za 🖅 Department of Mechanical and Industrial Engineering, University of Johannesburg, Doornfontein Campus, Johannesburg 2028, South Africa

Two major joining processes have been identified in joining PM parts, which are solid state and liquid state joining techniques. Diffusion bonding, friction stir welding and brazing categorised under solid state process were known to have been used to effectively join parts with low density or high porosity material together while liquid state or fusion-based process such as metal arc welding (MAW), laser welding (LW) and electro-beam welding (EBW) have been used majorly to weld parts with minimal porosity and high density [14].

The current review critically analyses the research outcome of other researchers based on their investigations on the weldability of PM metallic alloys. Different welding processes for PM alloys are reviewed, special attention is paid to the effect of welding processes on the microstructure, and mechanical properties of welded PM alloy. This review has laid a good foundation for the first author's PhD research on laser welding of spark plasma sintered produced (2507) duplex stainless steel, and its effects on the microstructure, mechanical and corrosion properties.

Various applications of powdered metallic alloys were explained with Figure 1.

The figure clearly explains the sequential process from PM to sintering process and lastly welding process.

2. Powder metallurgy process (PM)

PM process has witnessed an extensive research to its operation over the years, owing majorly to its versatility in application of metal forming processes. Equally, PM has seen a wide use in forming advanced materials which may not be possible with other traditional processes such as casting and forging. The PM process allows effective use of material without wastage giving a product with suitable mechanical properties and high density [15–17] Figure 2.
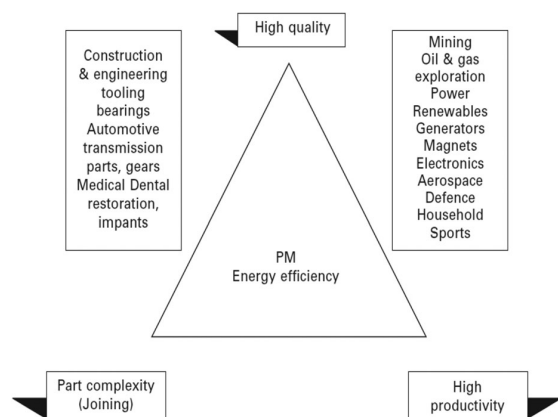
Figure 1. Joining PM to create complex geometries for industry [14].

The principal steps in PM are powder preparation, powder shaping and consolidation of the powder, which are presented schematically in Figure 3. The powder can be shaped or compacted under uniaxial pressure. Furthermore, the shaped compacts usually contain pores between the particles. Meanwhile, heat treatment and sintering below the melting temperature of the metallic alloy can be used to remove the pores that may be present. This phenomenon is driven by the reduction in solid–vapor interface area reduction [18].

The parameters that influence sintering include optimum conditions for sintering in a furnace, which is fundamental in obtaining sintered parts with a good metallurgical bond between the sintered particles, consequently, giving products with better mechanical properties [19–23].

3. Mitigating porosity effect through plastic deformation

Porosity is one of the features encountered in sintered PM materials. These porosity sites serve as potential sites for crack initiation. The porosity affects many mechanical properties including tensile properties, ductility and fatigue behaviour [24].

Major approach that can be used to alleviate or reduce porosity is plastic deformation at elevated temperature, in particular, hot forging thermal mechanical processing (TMP) Joining processes for PM parts [25]. Hot forging is usually carried out on fully dense, wrought or cast billets, formed into shape through multiple force of forging dies [26]. The forging exerts a uniaxial stroke with plastic strain added with frictional forces to collapse the pore [27], disrupt the oxide networks [28] and grain refinement [29].

Subsequently in this review, the weldability of sintered forged PM alloy will be discuss.

4. Joining processes for PM parts

Joining is a compendious term used to represent all processes adopted to attach one part to another [30]. The methods used in joining PM alloy are categorised as liquid and solid-state welding. Liquid welding processes such as gas metal arc welding (GMAW), gas tungsten arc welding (GTAW), electro-beam welding (EBW) and laser welding (LW) are usually used to weld high dense PM alloy, while solid-state welding processes such as brazing and diffusion welding are used for low dense PM parts (i.e. parts with high porosity) [4].

Notable welding techniques that have been applied in welding of PM materials are discussed.

Figure 2. Synergy between sintering process and welding process.
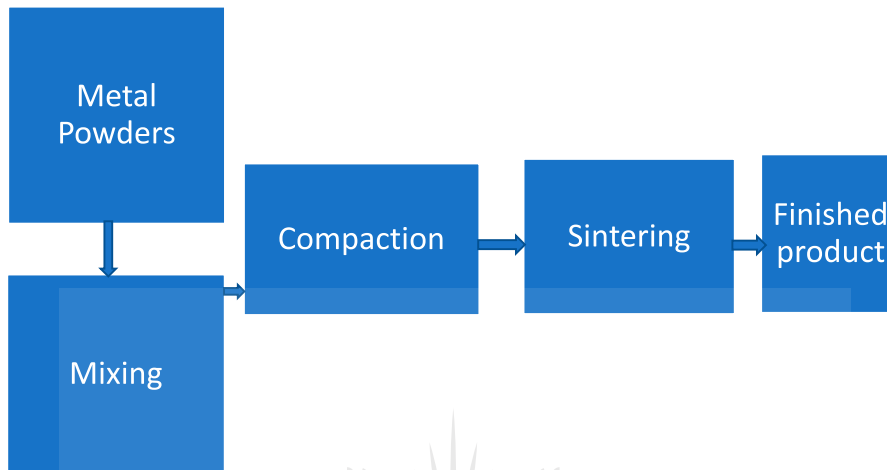
Figure 3. The powder metallurgy process.

4.1. Laser welding

Laser welding processes have gained prominence over the years in welding different metallic alloys. These processes are characterised by high welding speeds, precision and high efficiencies. Moreover, laser welding is associated with low heat input which result in low thermal distortion, residual stresses and deformation compared to other welding techniques [4,31–36]. Laser beam welding (LBW) uses laser beam to melt and join metals. The laser beam is either solid-state laser or gas [37] as shown in Figure 4. Notably, types of main laser used for welding are CO_2 laser, YAG
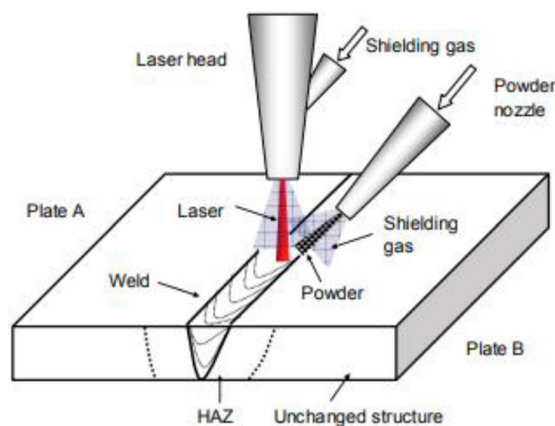
Figure 4. Schematic representation of a laser beam welding process [39].

laser, lamp-pumped, Laser diode (LD), LD-pumped solid state laser, disc laser, and fiber laser [38].

However, laser welding of sintered parts is characterised by various defects such as blow holes, resulting from gas entrapment, that fails to leave the melt during rapid solidification. Researchers have also noticed a phenomenon called hydrogen cracking, cold and hot cracking in medium carbon steel [40].

4.2. Electron beam

Electron beam welding (EBW) method melts and joins metals by heating with electron beam. EBW is normally carried out in a high vacuum (10^{-6} mbar). It has has the capability of giving a high cooling rate and high hardness in carbon steel. Also, EBW gives low distortion, keeping the dimensional stability of near net shape PM welded alloy [4,41]. Meanwhile, the metallic materials welded with an EBW method usually have a greater tendency for pore formation due to the vacuum acting as a potential site that trap gas during welding. However, choosing a suitable welding beam parameter has been known to control porosity in the sintered ferrous compacts [42].

4.3. Arc welding

In an arc welding process, an electric arc is usually struck between an electrode and a workpiece. Arc welding usually gives some level of porosity in the welded metal, which have a detrimental effect on

weld properties. Researchers also noticed porous weld can result from GMAW of low-density powder compacts, which negatively affects the mechanical properties through low ductility achieved in welded parts. As it is well known that the PM density and its composition eventually determines the mechanical properties of the welded parts [4].

5. Effect of porosity on the weldability PM alloy

It is important to note that welding PM metallic parts are usually different from welding cast or rolled metallic parts, due to the presence of pores in the microstructure of powder metallic alloy. Therefore, porosity forms part of the microstructural properties of PM component. Porosity is determined by several variables, such as particle size and shape, compaction pressure, sintering time and temperature, alloy additions, and processing route. These variables play a vital role in the mechanical properties of the resulting weld [43,44].

Porosity also plays a vital role in the welding of PM metallic alloys. The pores can have significant control on the ability of the material to resist thermal stresses and prevent the transfer of heat and electricity to the weld zone. However, impurities from lubricant residues and quench oils can be trapped in the pores, eventually impairing the mechanical properties of the weld metal [45–49].

Graver and Urffer [50] researched how gases entrapped in the pores can influence the mechanical properties of welded PM alloy. They successfully join ferritic 409L stainless steel with an average density of 6.80 g/cm^3 to wrought 409 tubing. The PM stainless steel with a density of 7.20 g/cm^3 density that was joined using GMAW comes up with a mechanical property that can be compared to that of wrought stainless steel. However, to reach the state of completely closed porosity the density must be > 7.4 g/cm^3, reducing gases entrapment in the pores, which eventually result in a product with improved mechanical property.

Kurt et al. [51] reported the use of friction stir welding technique in processing sintered aluminium (Al) powders of average size 80 μm pressed at different ranging from 350, 400 to 450 MPa, sintered at 450°C for 30 minutes in an argon atmosphere. Different densities were obtained at different compacted pressure, due to the work hardening, and continuous growth in the densified area fraction, the density increases progressively, with equal increases in pressure. In other words, increasing the pressure leads to an increase in density. Meanwhile, PM material usually comes with some level of porosity, that can be regulated by pressure and reduced by sintering. In their research they noticed the porosity level decreased with pressure. Defects and porosity were also found to have

deleterious effects on joining the sintered Al. Low compacted sintered Al has more porosities and greater defects, which have a consequential effect on the mechanical properties of sintered Al. Likewise, density increases the hardness level of sintered Al material, leading to porosity decrease.

Bahador et al. [12] showed that furnace sintered shape memory alloy (SMA) Ti–Ni welds exhibited the lowest weld quality owing to high porosity. While the microwave sintered (SMA) Ti–Nb and Ti–Ta displayed better weldability despite the presence of porosity. The authors concluded that porosity formed in the fusion zone is dependent on the pre-existing gases in the base material during processing, this elucidated why the microwave sintered Ti–30%Ta SMA showed lower weld porosity when compared with vacuum sintered Ti–51%Ni. Also, they studied the welding metallurgy of SMAs by comparing the weldability of sintered SMAs, with that of Ti–30%Ta cast alloy. Figure 5(a) shows the weld seam of Ti–30%Ta cast alloy revealing a T shape geometry with minimal porosity compared to Figure 5(b) weld of PM produced SMAs. They concluded that porosity and weld geometry are dependent on material processing.

6. Welding behaviour effect on the microstructure and mechanical properties of PM alloy

The changes in mechanical properties, microstructure and corrosion resistance of PM alloy largely depends on heat input and cooling rate [52].

6.1. Microstructural analysis of welded PM alloy

The phase and grains structure present in a metallic component are referred to as microstructure. Furthermore, the final properties achieved in a material is governed by microstructure, largely determined by the manufacturing process.

In welding research conducted by Elrefaey et al. [53] on the extruded PM Aluminium alloy using friction stir welding, they made it known that alloy produced through atomisation route, powder metallurgy and extrusion route are free from grain coarsening, and micro-segregation, predominantly because of the high cooling rate attained in those processes. Thus, material produced through these processes will have a fine grain structure, segregation free and also have homogenous microstructure. The atomised powder was cold compacted before hot extrusion and friction stir welded. The welding was performed at a speed of 500 rev/min, at a travelling speed of 3.3 mm/s and a force of 35 kN. They were able to achieve a sound weld, with no void and discontinuities. Meanwhile, the microstructure of the stir zone was observed to be finer and homogenous than that of the base metal resulting
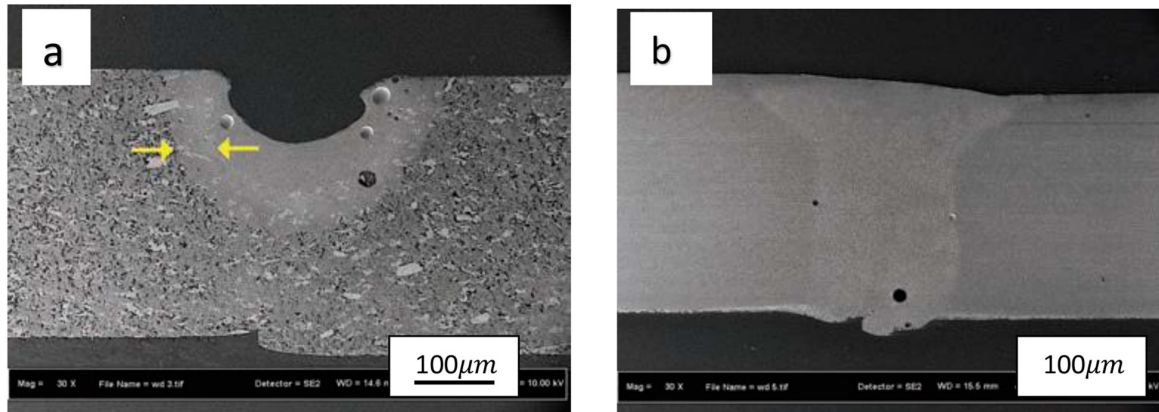
Figure 5. Cross-section of welds (a) Ti–30at.-%Ta P/M (b) Ti–30at.-%Ta casting SMAs.

into substantial average yield strength and tensile strength in stir zone compared to the base metal. Figure 6 presents a microstructure to better understand the above discussion. The figure shows a stir zone (SZ) structure to be finer and more homogeneous to the base metal structure, while the thermomechanical affected zone (TMAZ) has a slightly deformed structure, which is observed on both sides of the joint. Whereas, the heat affected zone (HAZ) has a microstructure similar to that of the base metal, formed adjacent to the TMAZ. A pattern called 'Onion' ring pattern was observed around the top area of the weld, emanating from the interaction between the material flow caused by the rotating pin and the shoulder-driven flow.

Also, Metzger [54] worked on the fusion welding process, using gas tungsten arc welding (GTAW) process to join PM of aluminium alloy Al–10Fe–5Ce (wt-%), consolidated from powder by extrusion to form a bar of rectangular cross-section. The study evaluated the effects of preweld vacuum heat treatment of the base metal, filler metal and the welding current type on the mechanical properties of the weld. Consequently, the author was able to remove the porosity in the weld using pre-weld vacuum heat treatment and a direct current electrode negative (DCEN) welding arc with helium shielding gas. The heat treatment was carried out at an estimated temperature of 400°C, resulting in the base metal strength reduction from 448 to 414 MPa. It was noticed that intermetallic compounds present close to the weld interface caused low ductility and strength.

Bahador [12] and his research team, worked on laser beam welding of PM Ti-based shape memory alloy (SMAs). The effect of laser welding defocused distance was examined on three shape memory alloys (Ti–51at.-%Ni, Ti–28%atNb and Ti–30at.-%Ta). tThe alloys were sintered by furnace and microwave sintering process. From the investigation it was reported that Ti–Nb and Ti–Ta SMAs sintered by microwave showed

good weldability, with high porosity, compared to furnace sintered Ti–Ni weld. An impairment in the weld quality of Ti–Nb and Ti–Ta SMAs furnace sintered was observed. The microstructural composition of PM alloy and cast Ti-based alloy SMAs weld seams was also investigated by field emission scan electron microscope (FESEM) and X-ray diffraction (XRD). Figure 7 shows an acicular α″ and β phases as the constituent phases of Ti–28at.-%Nb and Ti–30at.-%Ta welds, TiNi appeared to be the major phase observable in Ti–51at.-%Ni, as shown in Figure 7.

Yu et al. [55], worked on the stabilisation of Y–Ti–O precipitates on friction stir welded nano structured ferritic alloys comprising a dispersion of stable oxide particles, nanoclusters and ultrafine ferrite grains. They characterised the welded sample with JOEL 6500FEG Scanning electron microscope equipped with and electron back scatter diffraction (EBSD) detector. The maps orientation was analysed with 0.1M software. Consequently, an analysis was carried out on the stir zone (SZ), thermomechanically affected zone (TMAZ) and the base metal (BM). Figure 8 shows EBSD orientation maps of the three regions. Each colour represents a specific orientation. The red line represents low angle boundaries having misorientation angle between 2^0 and 15^0 while the black lines represent high angle grain boundaries, particularly having mis-orientation angle larger than 15^0. The grains size in the SZ is slightly elongated than that of the BM. The orientation maps of both SZ and BM indicates a fine-grained structure. While the average grain size for BM, SZ and TMAZ are 0.24 ± 0.11 nm, 1.04 ± 0.96 nm and 0.97 ± 0.85 nm, respectively. Consequently, the grain refinement mechanism in the SZ of the friction stir welded metal is caused by dynamic recrystallization (DRX). There are three types of recrystallization mechanisms, that vividly explains the refinement of grains during friction stir welding (FSW), Discontinuous (DDRX), Geometric (GDRX) and continuous (CDRX). Ferritic
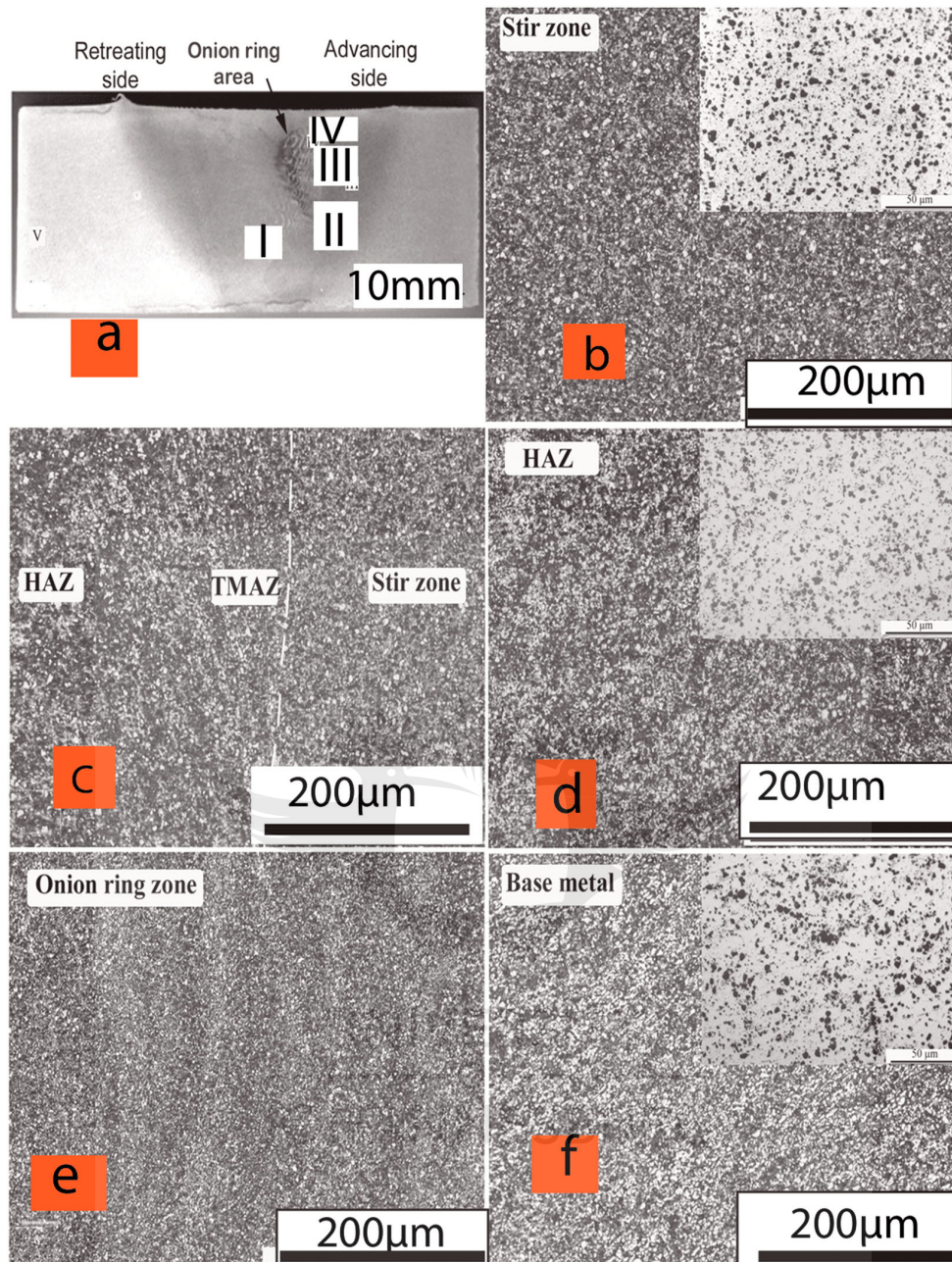
Figure 6. Joint microstructure: showing (A) cross-section macrostructure (B) microstructure of the stir zone (C) microstructure at the stir zone/HAZ interface D microstructure of the HAZ (E) microstructure of the onion ring zone (F) Microstructure of base metal [53].

steels usually have body centre cubic crystal structure, also known for high stacking fault energy, and CDRX recrystallization mechanisms [56].

However, elongated grains in friction stir welded material creates high strain rate deformation in the material, resulting in elongated subgrains that developed from the elongated dislocated cells formed by dynamic recovery. Likewise, the rotating tool stirring action results in grain boundaries with a high angle along a preferred direction, eventually giving birth to an elongated grain as shown in Figure 8(b) [57]. The <111> shear texture with an intensity of 9.8 was observed at the SZ, which was also reported in the

work of Chen et al. [58] on microstructural evolution offriction stir welded nanostructured ODS alloys.

6.2. Mechanical properties

In the available research on PM welding, tensile strength, hardness and fracture properties are the most evaluated mechanical properties, which can be used to evaluate the performance of load-bearing capabilities of the welded PM alloy in engineering application. The discussion below addresses how porosity level can play a role in the mechanical properties of welded PM alloy.
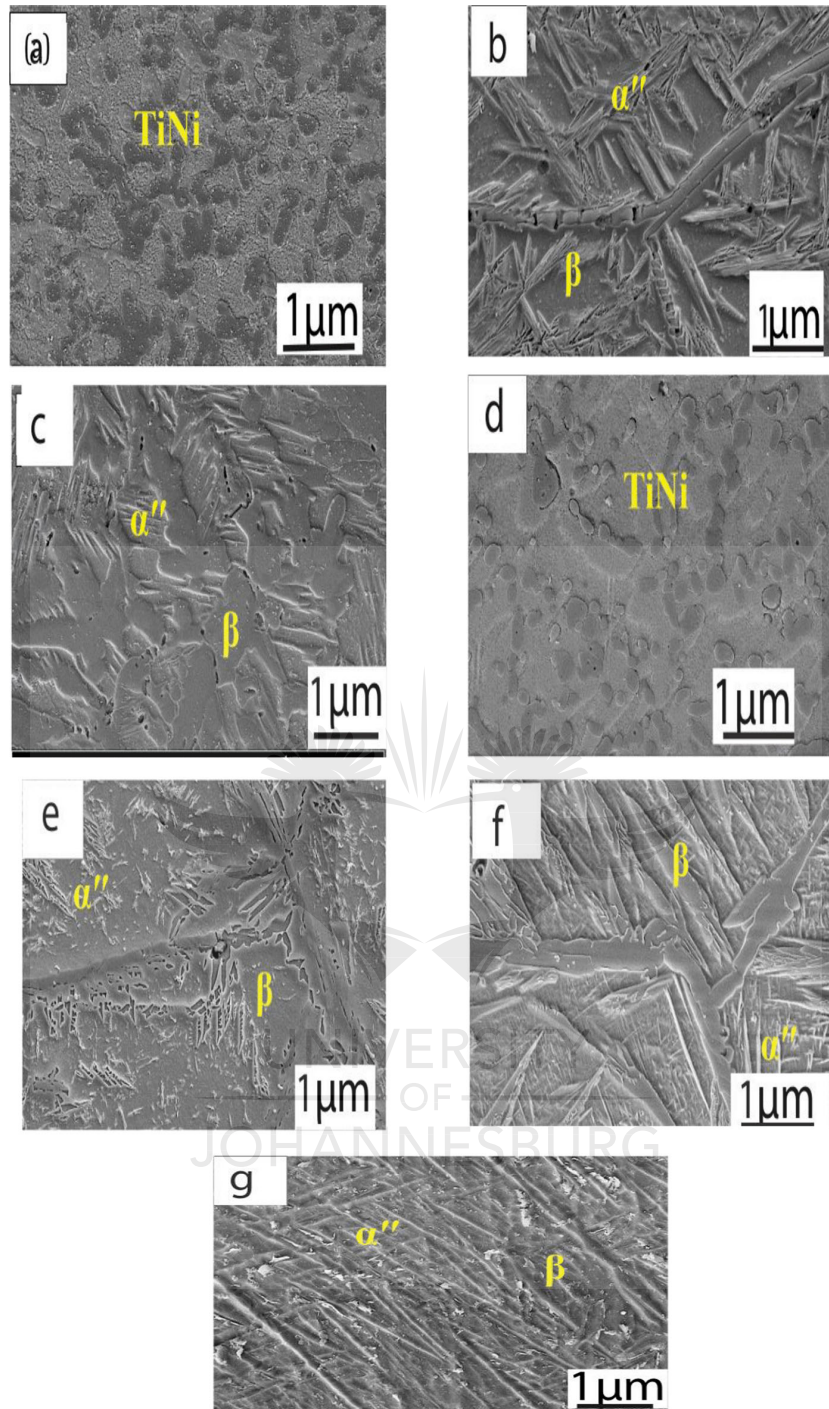
Figure 7. FESEM microstructure, positive defocusing distance (a) Ti–51at.-%Ni, (b) Ti–28at.-%Nb and (c) Ti–30at.-%Ta P/M, negative defocusing distance (d) Ti–51at.-%Ni, (e) Ti–28at.-%Nb (f) Ti–30at.-%Ta P/M and (g) Ti–30at.-%Ta casting SMAs [12].

6.2.1. Hardness

Correa et al. [59] conducted hardness test on pulsed gas tungsten arc welded powder metal Fe–Ni alloy using mild steel filler metal and Fe–Ni filler metal. Figure 9, shows no major variation in hardness profile in the heat-affected zone (HAZ) when compared with the base metal for both filler metals, indicating a fine continuity of mechanical properties.

Chandramouli et al. [60] studied the hardness variation on welded sinter-forged steel based on the pre-alloyed Atomet 4601 steel, explained in Figure 10. Little variation in hardness values at the weld zone (WZ) and the heat-affected zone (HAZ) is in agreement with obseravation made by Correa [59] The high hardness at the WZ was due to the pore-free formation in the welding zone, caused by the
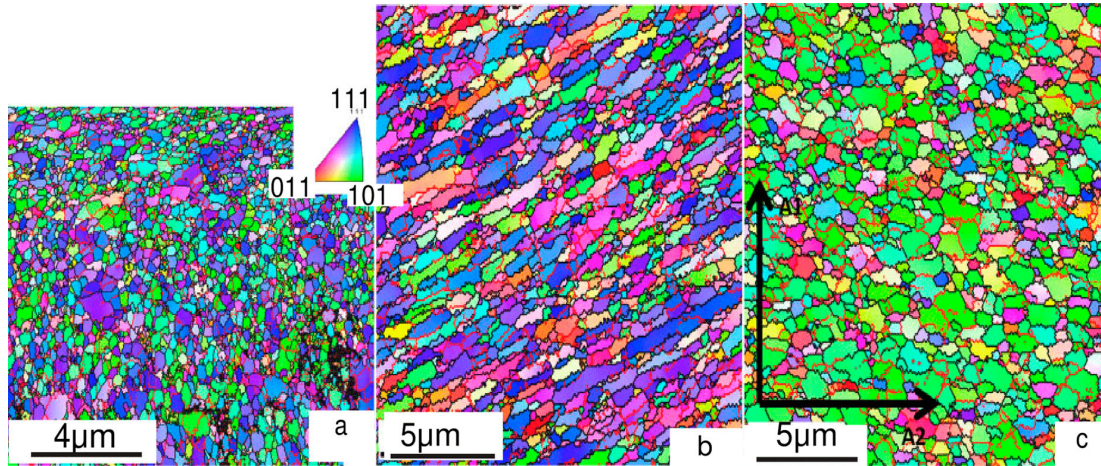
Figure 8. (a) Orientation maps of a BM, (b) SZ and (c) TMAZ. BM shows fine equiaxed ferrite grains and SZ shows elongated ferrite grains; grains in SZ and TMAZ are coarser than grains in BM [55].

melting and solidification of the material. Thermal welding cycle also plays an important role in the hardness around friction zone (FZ). It was explained that parent metal density is more responsible for the increased hardness of the parent alloy steel than the welded joint. However, the parent metal hardness can be linked to the level of porosity. Also, the parent metal has high density due to it being subjected to a compressive load upset. Meanwhile, the density of the upset material was enhanced through pores closure and strain hardening.

In another work by Chandramouli et al. [61] on the experimental investigations off welding behaviour of sintered forged Fe–0.3%C–3%Mo low alloy steel. The hardness profile for the welded steel shown in Figure 11(a), reveals minimal variations of hardness values along the weld zone owing to the microstructural homogeneity in the welded zone, which agrees with our earlier discussion. They discovered the highest hardness weld zone of 245 HV, accounted for by the homogenous acicular/lathe ferrite structure in-conjunction with and blow holes absence, as also explained in the reference [62–64].

A study conducted by Kurt et al. [51] on porosity effect on the weldability of powder metal parts joined by friction stir welding at a speed of 1800 rev /min, and welding speed of 3.33 mm/s, reveals that the hardness increase was associated with an increase in
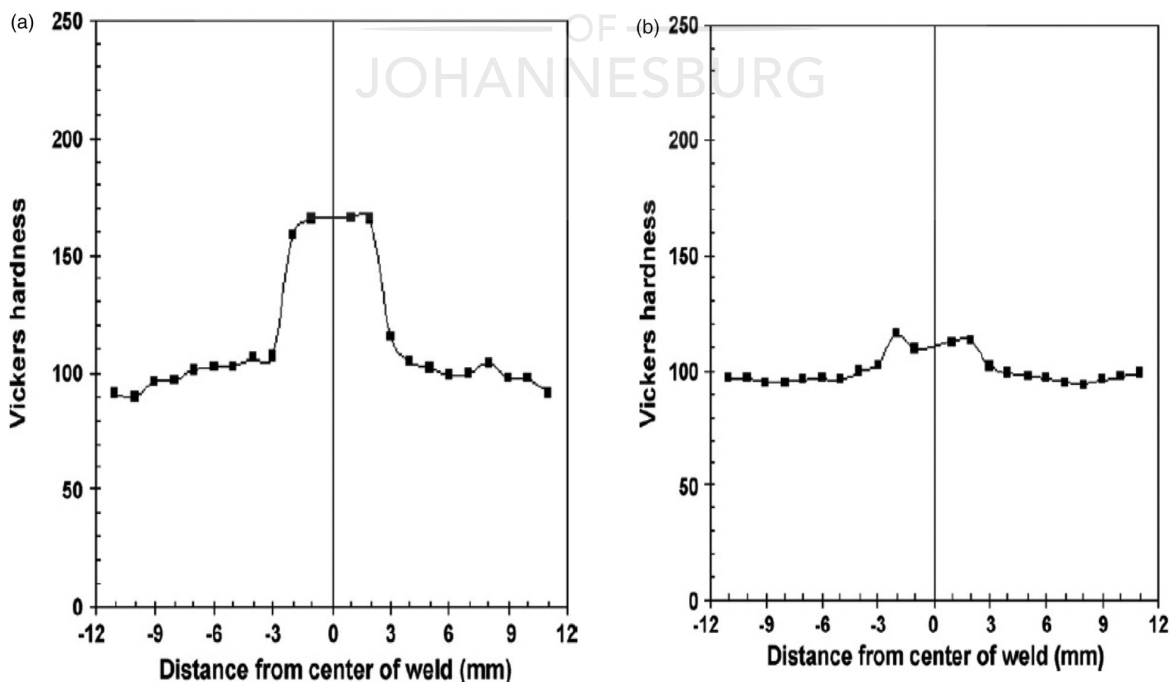
Figure 9. (a) Hardness profile of a Fe–Ni powder metal alloy using filler metal of mild steel (b) Hardness profile of a Fe–Ni powder metal alloy using filler metal of Fe–Ni [59].
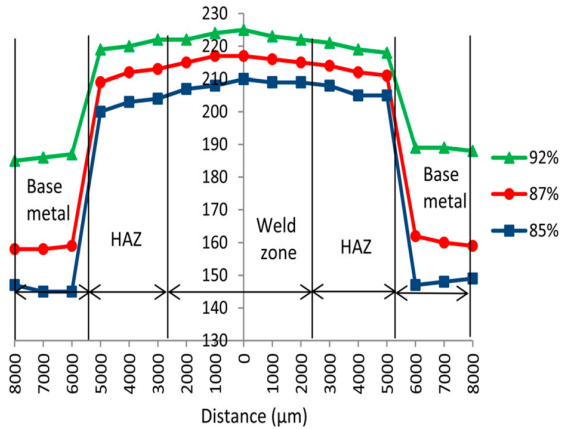
Figure 10. Plots of hardness values at various zones of weldment of welded alloy steel [60].

compacting pressure owing to the amount of porosity and change of density. However, base material compacted at a load of 450 MPa is 56 HV, and 49 HV for the base metal compacted at 350 MPa in the heat-affected zone as shown in Figure 11(b)

PM preform steel sheets were joined to wrought copper using gas tungsten arc welding, using current pulse frequency to refine the fusion zone microstructure. The pulse current allows iron dendrites to become more equiaxed and distributed uniformly because of the dendrite fragmentation. In the investigation, the weld strength increased due to density increase of the steel preforms, which was attributed to fast cooling rate of the weld pool. From Figure 12, the frequency of 6 Hz gives minimum hardness when juxtapose with other frequencies. This agrees with the equiaxed dendrites and uniform dendrites in the weld metal at the highest frequency. Also, the concentration of iron variation in the weld metal can also be responsible for the situation. They explained the science behind the grain refinement through optimum

frequency, as due to thermal reduction and enhanced flow [65].

6.2.2. Tensile strength

The uniaxial standard tensile test is mostly conducted on cylindrical bars or dog-bone shaped specimen, machined from welded sample and tested according to ASTM E8. From the further review of Chandramouli et al. [61] work on experimental investigations behaviour of welded sintered and forged Fe–0.3%C–3%Mo low alloy steel. They discussed the variation of tensile properties for both the welded alloy and base metal with respect to density. The percentage reduction in area and elongation decreases linearly with porosity, in agreement with the findings by Correa et al. [66]. They eventually came up with a welded alloy that has higher tensile strength when compared to the base material as shown in Figure 13. This phenomenon was accounted for by three factors, namely: residual stress in the base metal after welding, acicular ferrite formation at the weldment, segregation of the metal alloy. In addition, porosity absence in the weld metal could have also increased the welded joint strength.

Joseph et al. [7] work on pulsed current gas tungsten arc welding (PCGTAW) of sintered forged AISI 4135 steel. They examined the transverse tensile properties such as the tensile strength and percentage elongation on the based specimen and the welded metal, the results are shown in Figure 14. Their result shows an average tensile strength of 685 MPa for the base metal while the tensile strength value of the PCGTAW joints was 703 MPa. They associated the good quality of the weldments to low heat input. Meanwhile, a percentage elongation of the PCGTAW joints was 8.60% and 8.50% for the base metal as shown in Figure 14, suggesting little difference in the ductility of both the base metal and the welded metal. Consequently, strain-hardening effect occurring during hot upsetting
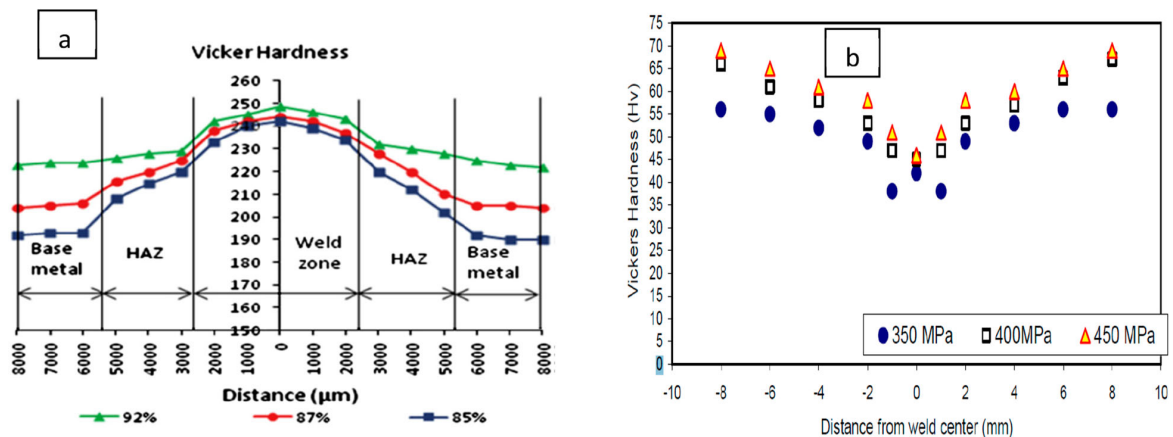
Figure 11. (a) Hardness profile of the welded alloy steels [61]. (b) The effect of compact pressure and welding zone on the hardness of compacted Aluminium [51].
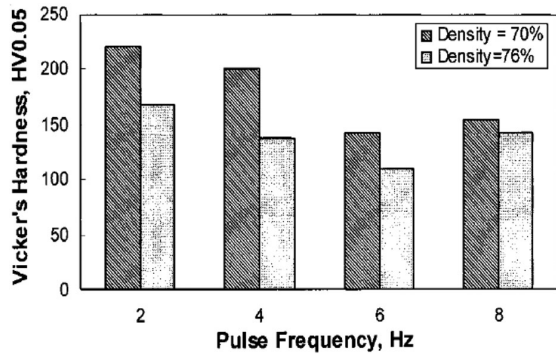
Figure 12. Hardness at centre of weld bead [65].

6.2.3. Fracture analysis

Chandramouli et al. [61], discussed the fracture pattern for both the Tungsten inert gas (TIG) welded and base metal alloy steel, as shown in Figure 15(a) shows the fracture morphology in the base metal alloy. They notice a de-cohesion caused by the presence of large voids and a few microvoids. Also, the deep valleys and depressions presence in the fractography explains the brittle nature of the fracture. A few micro dimples were spotted in Figure 15(b), a mixed mode of fracture was discovered in the welded steel, shown by the occurrence of large number of dimples. Vertical facets with few large-sized voids were also seen, which are pointers to crack initiation and stress concentration Figure 15.

Elrefaey et al. [53] carried out a fracture test on friction sir welded extruded powder metallurgy Al alloy, welded at applied rotation speed of 500 rev/min, at a travelling speed of 3.33 mm/s and a compressive force of 35 kN. Figure 16(a) shows a tensile fracture surface with few cracks, many ridges and tears. The macroscopic fracture process accounted for the rough landscape, taking place at a plane closer to the angle of applied stress. However, a dimple-like structure is observed in the morphology when the rectangular area is carefully observed in Figure 16(a) and (b).
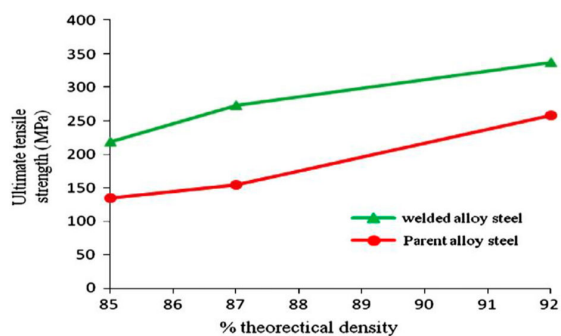

Figure 13. Plots of tensile strength plots of parent and welded low alloy steels at various densities [61].
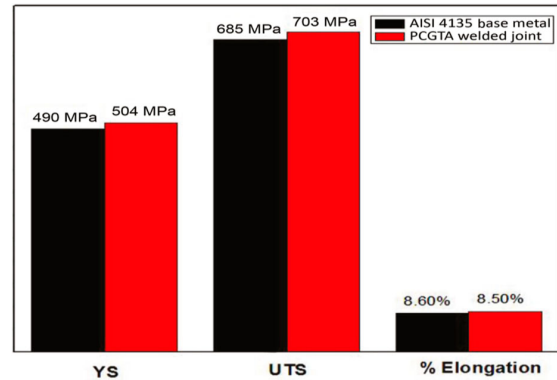

Figure 14. Tensile properties of AISI 4135 base metal and welded joint [7].

Meanwhile, voids and Si particles originating from unattached silicon was observed in Figure 16(c).

Jobel et al. [7] conducted a fracture test on welded pulsed gas tungsten arc welded (PCGTAW) sintered AISI steel. Fractography of different spherical dimples for both base metal and the welded metal tensile test specimen was shown in Figure 17(a,b), representing the base metal. It was shown that the metal fails in a ductile manner under tensile force. However, from Figure 17 (b) and (d) representing the welded joints, a parabolic-shaped dimple was observed, characterising ductile fracture. Also, flat cleavage like facets is seen with large size pores, indicating the initiation of rupture on the surface, partly brittle and partly ductile behaviour, also known as mixed mode of failure, explains the enhanced strength and hardness. Lastly, the increase in the strength of the welded area can be explained by the grain refinement that occurred during the welding operation.

Table 1 compares the Tungsten welding process at different welding conditions, for different PM alloy, based on the existing literature.

7. Summary and outlook

Based on the overview of the metallurgy of welded PM alloys, their related microstructures, and mechanical properties of PM welded alloys were comparatively studied. The review shows an understanding of microstructural analysis and mechanical properties of welded PM alloy and how the current understanding can inspire new approaches for the fabrication of powdered metallic alloy through the welding process. Also, the review has provided a background for our current research on Laser welding of spark plasma sintered steel.

The following major conclusions can be drawn:

(1) The porosity in the PM alloy goes a long way to determine the mechanical and microstructural properties of the weld. The pores trap impurity and cause hot or cold cracking, and reduces the
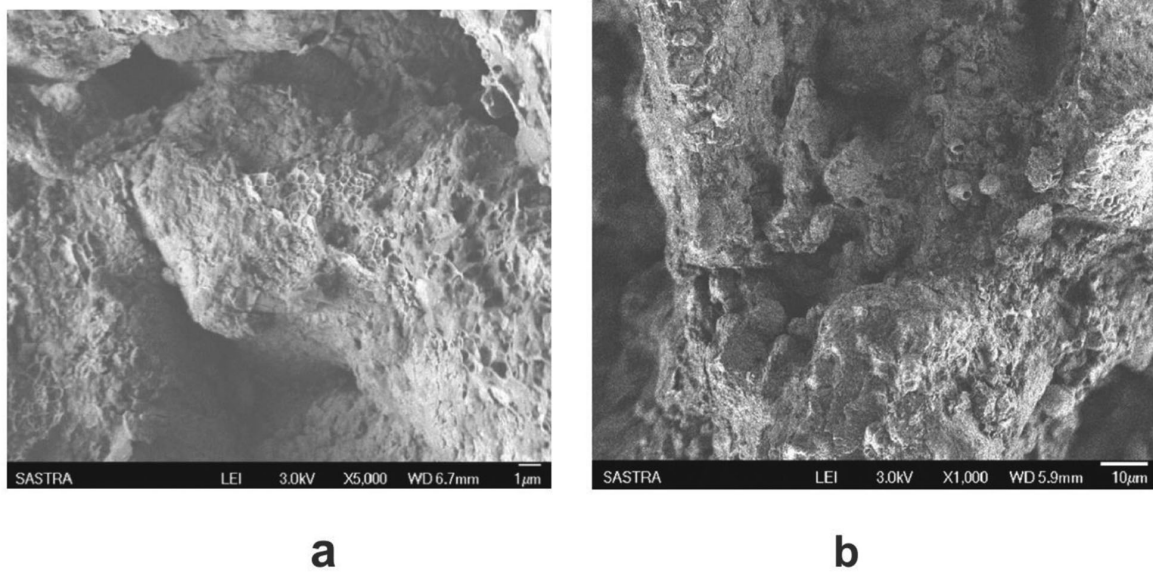
Figure 15. SEM images of fracture surfaces of (a) Base metal, (b) welded alloy steel [61].

thermal conductivity of the weld, resulting in low hardenability, It is true the pores reduce the thermal conductivity (and thermal diffusivity as well) but the pores also reduce the amount of heat to be dissipated. However, the lower the porosity of PM alloy the more outstanding the mechanical properties of the weld.

(2) Difficulties associated with powder materials such as porosity, contaminations, inclusion, affect the ductility of the welded material, reducing its capability to resist strain in the heat-affected zone.

(3) The solid-state welding processes e.g. friction stir welding may be appropriate to reduce the effect of the pores on the final weld properties since it promotes pore closure which eventually leads to pore-free weld. Welding is carried out below the melting temperature of the PM alloy, and it also refines the grains of the welded metallic alloy.

(4) PM alloy comes with some level of porosity, therefore, the use of low input welding method is therefore recommended. Laser fusion welding process with high welding speed and low heat input, limit the thermal distortion, considerable produce small heat-affected zone that reduces the residual stress, strain and effectively minimised the thermal distortion.

(5) The tensile strength of welded PM alloy steel is majorly influenced by its porosity.
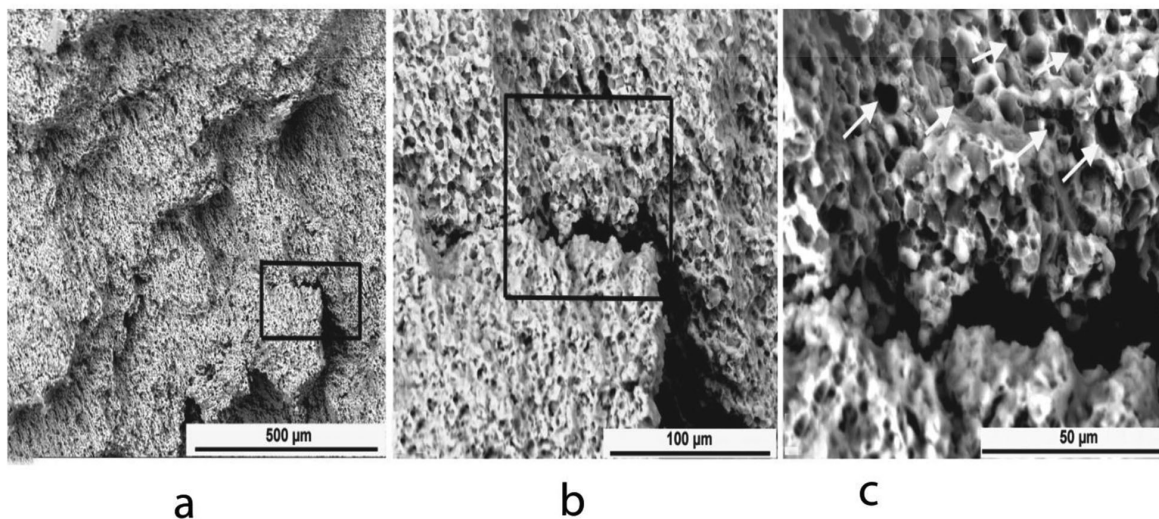
Figure 16. SEM of fracture tension sample: (a) General view of the surface; (b) magnified view of the propagated crack; (c) Dimple-like fracture surface [53].
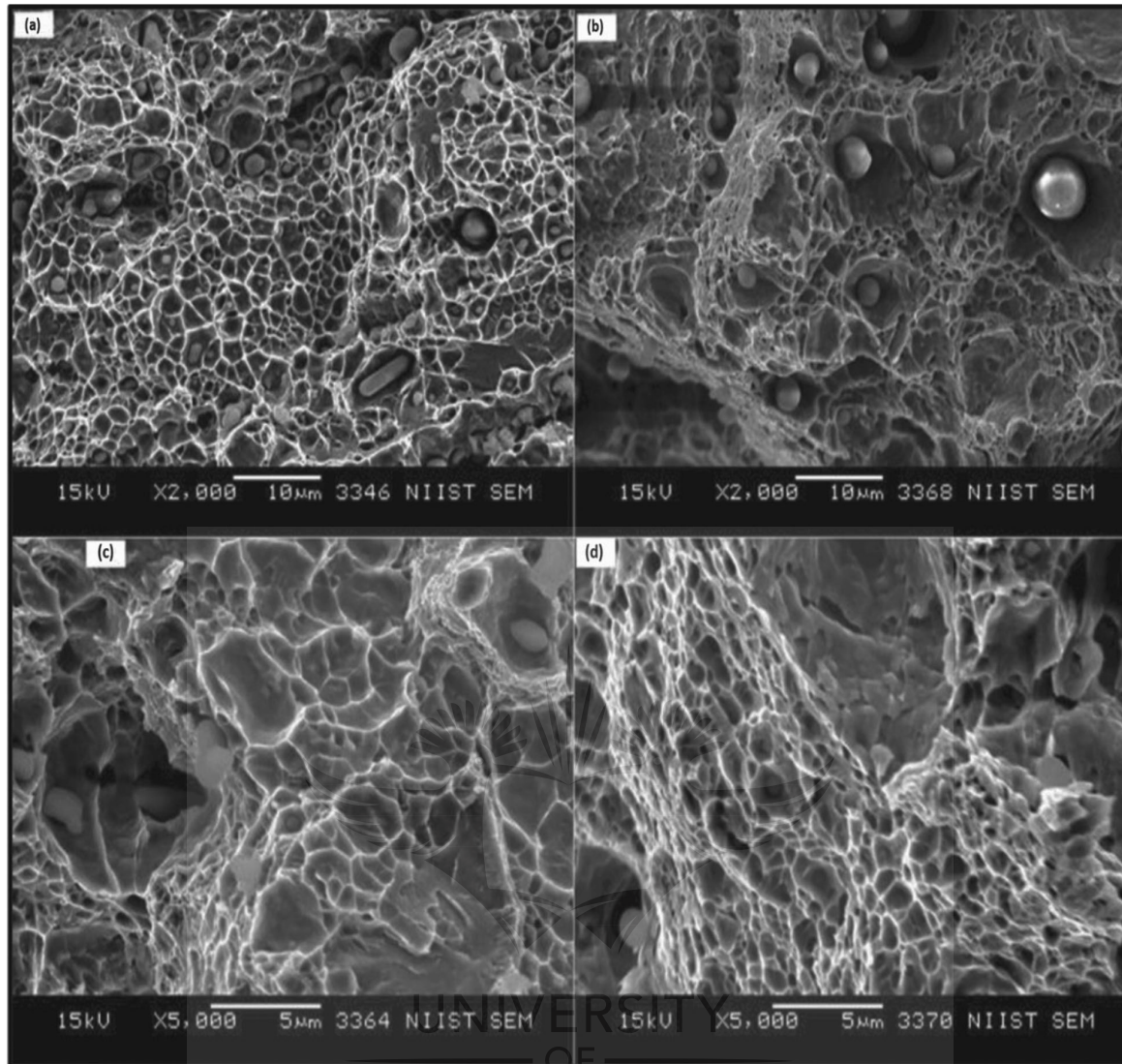
Figure 17. Fractographs of tensile specimens: (a) and (c) base metal, and (b) and (d) welded metal [7].

Table 1. Recommended parameters for Tungsten inert gas welding of powdered metallic alloy.

Powdered metallic alloy	Types of weld preparation	Welding processes	Relative density (%)	Operating parameters			References
				I(A)	Voltage (V)	Speed(mm/s)	
Sintered forged pre-alloy –Atomet 4601	–	Tungsten Inert gas welding (TIG)	85–92	150	9	1.167–1.25	[60]
PM steel and wrought copper	Butt welding preparation	Gas tungsten Arc welding	70–76	160	12	0.002	[65]
sintered and forged Fe–0.3%C–3% Mo low alloy steel	No joint preparation	Tungsten Inert gas welding (TIG)	85–92	150	9	1.167–1.25	[61]
Sintered AISI 316 Stainless Steel	Butt Joint Without gap on the joint	Tungsten Inert gas welding (TIG)	-	16–24	15–25		[67]

Disclosure statement

No potential conflict of interest was reported by the author(s).

Notes on contributors

Ayorinde Tayo Olanipekun is currently a Ph.D. student of Mechanical Engineering, University of Johannesburg. His

curiosity and strong background in research has allowed him to keep up with the latest developments in computational materials science and Machine learning research. He received his M.Sc. degree in Mechanical Engineering, University of Ibadan, 2014.

Dr Nthabiseng Beauty Maledi is a Senior Lecturer at the School of Chemical & Metallurgical Engineering, University of the Witwatersrand. She is currently registered for a Professional Master's degree in Welding. Her research interests are in the broad areas of physical metallurgy, corrosion science, materials characterisation, welding, energy, and the environment. Her particular research focus is in welding of engineering and new materials intended for novel applications.

Dr Peter Madindwa Mashinini has published over 20 publications in international journals and conference proceedings. Peter Madindwa Mashinini received his doctoral degree from Nelson Mandela Metropolitan University, Port Elizabeth, South Africa. He is presently working as an associate professor and head of department at the department of Mechanical and Industrial Engineering Technology at University of Johannesburg in South Africa. His research interest includes friction stir processing, laser processing, and development of composite materials. He has published more than 40 technical articles in peer reviewed international journals and conferences.

ORCID

Ayorinde Tayo Olanipekun http://orcid.org/0000-0001-6284-0732
Nthabiseng Beauty Maledi http://orcid.org/0000-0003-2862-2218
Peter Madindwa Mashinini http://orcid.org/0000-0001-8614-1610

References

[1] Upadhyaya GS. Powder metallurgy technology. Cambridge Int Science Publishing; 1997.

[2] Han Y, Zou D, Chen Z, et al. Investigation on hot deformation behavior of 00Cr23Ni4N duplex stainless steel under medium–high strain rates. Mater Charact. 2011;62:198–203.

[3] Dutkiewicz JM, Maziarz W, Czeppe T, et al. Powder metallurgy technology of NiTi shape memory alloy. Eur Phys J Special Topics. 2008;158:59–65.

[4] Selcuk C, Bond S, Woollin P. Joining processes for powder metallurgy parts: a review. Powder Metall. 2010;53:7–11.

[5] Krishnaa MV, Kandavel T, Reddy KP, et al. Weldability study on atomet 4601+ TIC alloy steels. Int J Pure Appl Math. 2017;117(16):465–473.

[6] Jayabharath K, Ashfaq M, Venugopal P, et al. Investigations on the continuous drive friction welding of sintered powder metallurgical (P/M) steel and wrought copper parts. Mater Sci Eng A. 2007;454:114–123.

[7] Joseph J, Muthukumaran S, Pandey K. Weldability characteristics of sintered hot-forged AISI 4135 steel produced through P/M route by using pulsed current gas tungsten arc welding. High Temp Mater Process. 2016;35:9–19.

[8] Datta P, Upadhyaya G. Sintered duplex stainless steels from premixes of 316L and 434L powders. Mater Chem Phys. 2001;67:234–242.

[9] Martín Pedrosa F, García Cabezón C, Blanco Val Y, et al. Tribocorrosion behaviour of powder metallurgy duplex stainless steels sintered innitrogen, (2013).

[10] Morakotjinda M, Kuljittipipat N, Poolthong N, et al. Sintered materials prepared from stainless steel series 300 and 400 powders. J Metals Mater Miner. 2017;18:69–74.

[11] Layus P, Kah P, Khlusova E, et al. Study of the sensitivity of high-strength cold-resistant shipbuilding steels to thermal cycle of arc welding. Int J Mech Mater Eng. 2018;13:3.

[12] Bahador A, Hamzah E, Kondoh K, et al. Defocusing effects of laser beam on the weldability of powder metallurgy Ti-based shape memory alloys. Proc Eng. 2017;184:205–213.

[13] Hamill JA, Manley FR, Nelson DE. Fusion welding P/M components for automotive applications, in, SAE Technical Paper, 1993.

[14] Selcuk C. Joining processes for powder metallurgy parts. In: Chang Isaac, Yuyuan Zhao, editors. Advances in powder metallurgyElsevier; 2013. p. 380–398.

[15] Orban R. New research directions in powder metallurgy. Rom Rep Phys. 2004;56:505–516.

[16] Salak A. Ferrous powder metallurgy. Cambridge: Cambridge International Science Publishing; 1995. 227-237.

[17] R.M. German, Powder metallurgy of iron and steel, John! Wiley & Sons, Inc, 605 Third Ave, New York, NY 10016, USA, 1998. 496 (1998).

[18] Kaysser WA, Petzow G. Advanced materials by powder metallurgy. Angew Chem. 1988;100:1021–1025.

[19] German RM. Powder metallurgy and particulate materials processing: the processes, materials, products, properties, and applications. Metal Powder Industries Federation Princeton. 2005.

[20] Jenkins I, Wood JV. Powder metallurgy: an overview. London: Woodhead Publishing Ltd; 1991.

[21] Lenel FV. Powder metallurgy: principles and applications. Princeton: Metal Powder Industry; 1980.

[22] Thümmler F., Oberacker R. Introduction to PM, the institute of materials. London: Institute of Materials; 1993. p. 255–258.

[23] Schatt W, Wieters K-P. Powder metallurgy: processing and materials, European powder metallurgy association, 1997.

[24] Yi J, Gao Y, Lee P, et al. Scatter in fatigue life due to effects of porosity in cast A356-T6 aluminum-silicon alloys. Metall Mater Transact A. 2003;34:1879.

[25] James WB. Powder forging. Rev Part Mater. 1994;2:173–213.

[26] Bose A, Eisen WB. Hot consolidation of powders & particulates. Princeton: Metal Powder Industries Federation; 2003.

[27] Abdel-Rahman M, El-Sheikh M. Workability in forging of powder metallurgy compacts. J Mater Process Technol. 1995;54:97–102.

[28] Altan T, Ngaile G, Shen G. Cold and hot forging: fundamentals and applications. Ohio: ASM International; 2004.

[29] Sweet GA, Wells MA, Taylor A, et al. Thermal mechanical processing of press and sinter Al-Cu-Mg-Sn-(AlN) metal matrix composite materials. Metals (Basel). 2018;8:480.

Appendix .A :Data on assessment and exploratory statistical correlation data analysis of sintered Nd:YAG laser welded 2507 duplex stainless steel
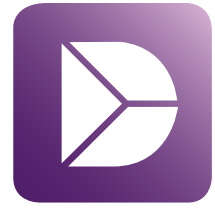
Data Article

Data on assessment and exploratory statistical correlation data analysis of sintered Nd:YAG laser welded 2507 duplex stainless steel

Ayorinde Tayo Olanipekun [a],[*], Peter Madindwa Mashinini [a], Nthabiseng Beauty Maledi [b]

[a] *Department of Mechanical and Industrial Engineering Technology, University of Johannesburg, South Africa*
[b] *School of Chemical and Metallurgical Engineering, University of the Witwatersrand, Johannesburg, South Africa*

ARTICLE INFO

ABSTRACT

The effect of Spark Plasma Sintering (SPS) parameters and Nd:YAG laser welding parameters such as sintering temperature, sintering time, welding power, welding speed, on Vickers hardness mechanical properties of the Weld Zone(WZ) was statistically investigated. Rectangular plates of 2507 Duplex Stainless Steel (DSS) fabricated by SPS were joined by Nd: YAG laser welding process. Linear regression analysis was performed on the data, followed by Pearson correlation analysis to relate hardness with other predicting variables and show their statistical significance to hardness value of the weld zone.The evaluated R^2 which is 49% was used to measure the closeness of the data to the regression fitted line.

© 2020 The Author(s). Published by Elsevier Inc.
This is an open access article under the CC BY-NC-ND license (http://creativecommons.org/licenses/by-nc-nd/4.0/)

---

* **Corresponding author**.
  E-mail address: atolanipekun@uj.ac.za (A.T. Olanipekun).

Specifications Table

Subject	Mechanical Engineering and Materials science
Specific subject area	Data analysis, Welding Engineering and Nanotechnology
Type of data	Table
	Chart
	Graph
	Figure
How data were acquired	The data was acquired using Future-Tech Microhardness tester (FM-700)
	Software: Google Tensor flow, Python and Jupyter
Data format	Raw
	analyzed
	Filtered
	Normalized
Parameters for data collection	
	• Sintering process: 2507 DSS powder samples was sintered at the following temperatures (S-temp) 900 °C, 1000 °C, 1100 °C at a pressure of 50 MPa under vaccum. A heating rate of 100 °C/m was considered for the sintering process that lasted for between (S-time) 5min-10 min.
	• Nd:YAG laser welding: The laser power and welding speed adopted in this research for Sample A, B and C were Laser power (Wel-power) of 1500 W, 1700 W, 2000 W, while the welding speed employed are 3 m/min, 3 m/min and 2 m/min respectively
	• Vickers Hardness test: Vickers microhardness (HV) test was carried out using Vickers microhardness (Future Tech FM-700) tester, applying a load of 300 gf with dwell time of 10 s at room temperature.
Description of data collection	The data used for the stastical analysis was gotten from three experimnetal processes, Sintering parameters and hardness test data. The welding parameters were selected based on the optimized parameters from literature. The Vickers microhardness test data was targeted at the welded zone (WZ) for this research.
Data source location	University of Witwatersrand, Johannesburg, South Africa
Data accessibility	With the article
	Mendeley Data
	https://data.mendeley.com/datasets/c49p4g34cc/
	2#folder-795deb94-da97–479a-b3ec-71154d68a4bd

Value of the Data

- The data is beneficial to researchers that may likely want to work in the area of data and machine learning analysis of engineering materials.
- Data utilized as a reference to investigate the statistical coefficient of sintered and welded data on the overall mechanical properties of 2507 DSS and regression analysis.
- Further research on microhardness analysis of welded specimen can be built on the Vickers analysis carried out in this research.

1. Data Description

In this information dispensation there is enormous data like feedbacks, medical data, materials data and share data e.t.c., data science has in no doubt assisted us to make quality decisions in all sphere of life. Recently, material science and engineering field has accepted data science as a tool to analyse materials properties data. Data science has help to greatly reduce the cost save time in material structure design, overall reduce time in material design and its behaviour [1]. The data and analyses included here corroborate the statistical analysis drawn from the study of ND:YAG laser welded 2507DSS. Chemical composition data analysis of the powdered 2507 (DSS) Table 1. Data sets in Table 2. Summarizes the experimental data gotten from the sintering process and laser welding of 2507 DSS which includes the sintering temperature, sintering time,

Table 1
Chemical composition of the As-received powdered 2507 DSS (wt%).

Material	C	P	Si	Ni	N	Mn	S	Cr	Mo	Fe
2507	0.02	0.014	0.4	7.1	0.31	0.8	0.001	24.4	3.76	Balance

Table 2
Sintering and welding parameters [3].

S-temp (°C)	S-time (min)	Wel-power (W)	Wel-speed(m/min)	Hardness (HV)
1000	5	1500	3	343.7
1000	5	1500	3	350.1
1000	5	1500	3	351.7
1000	5	1500	3	365.6
1000	5	1500	3	337.5
1000	5	1500	3	362.8
1000	5	1500	3	356.7
1000	5	1500	3	357
1000	5	1500	3	356.9
1000	5	1500	3	361.2
900	10	1700	3	347.6
900	10	1700	3	325
900	10	1700	3	310
900	10	1700	3	331.8
900	10	1700	3	349.9
900	10	1700	3	339.3
900	10	1700	3	386.1
900	10	1700	3	347.9
900	10	1700	3	381.8
900	10	1700	3	355.7
1100	5	2000	2	354
1100	5	2000	2	379
1100	5	2000	2	380.4
1100	5	2000	2	373.7
1100	5	2000	2	380.9
1100	5	2000	2	401.4
1100	5	2000	2	396.9
1100	5	2000	2	392.7
1100	5	2000	2	377.2
1100	5	2000	2	395.1

Table 3
Pearson correlation between Hardness and S-time.

	Hardness (HV)	S-time (min)
Hardness(HV)	1.0000	−0.4539
S-time (min)	−0.4539	1.0000

welding power, welding speed and hardness. Fig. 1 shows the graphics detail seaborn plot for all the data. Fig 2. Shows the heat mapping representation for the data. Fig. 3 depicts the linear regression plot for predicted value and true value of the hardness. Fig. 4 represents the linear regression plot for sintering time(S-time) against hardness. Fig. 5 represents the linear regression plot for welding power (Wel-power) against hardness. Fig. 6 describes the linear regression plot for welding speed (Wel-speed) against hardness. Fig. 7 illustrates the linear regression plot for sintering temp (S-temp) against hardness.

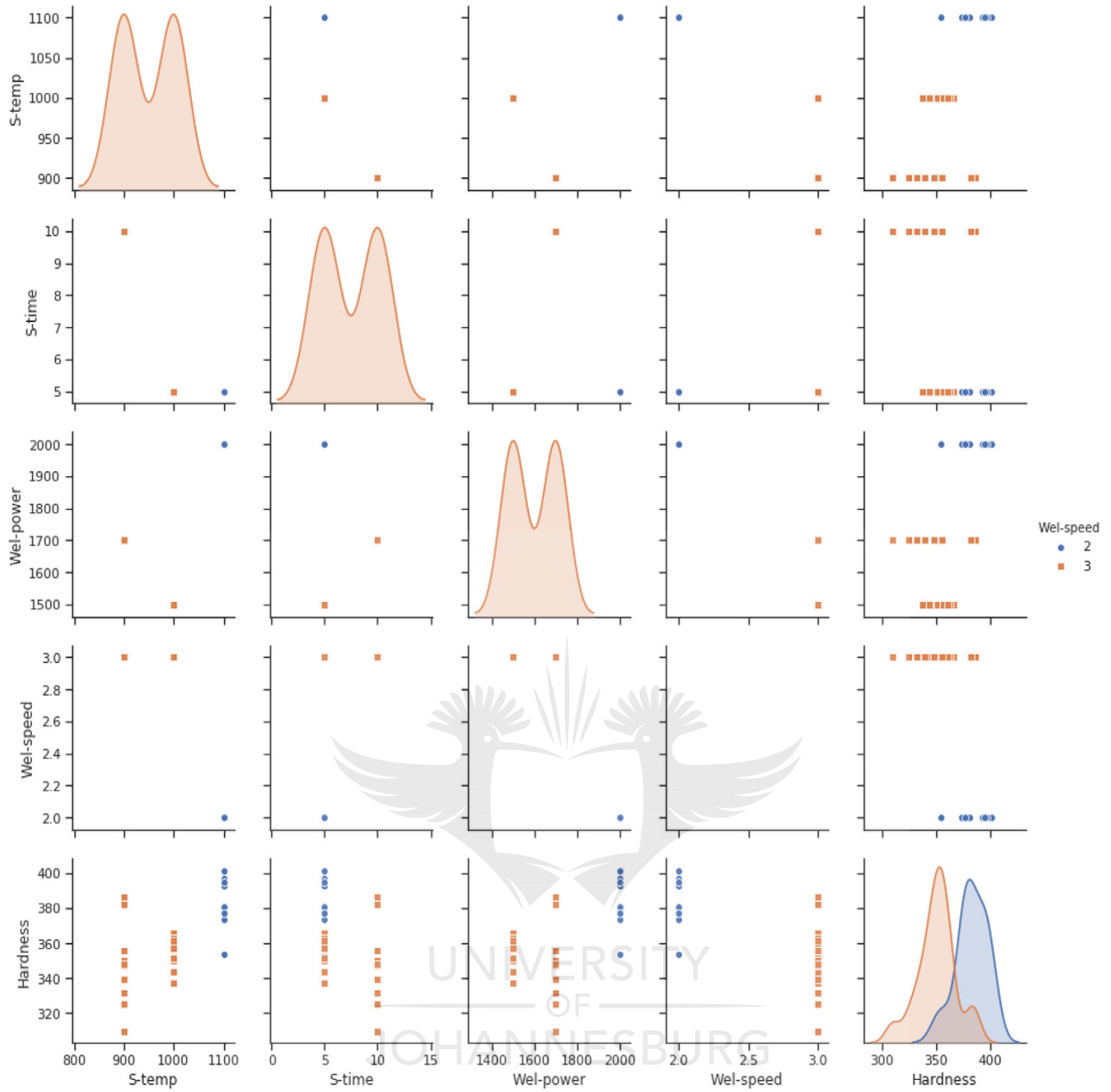Table 3 –Table 6 explain the extent of pearson correlation of hardness to the predictor values.
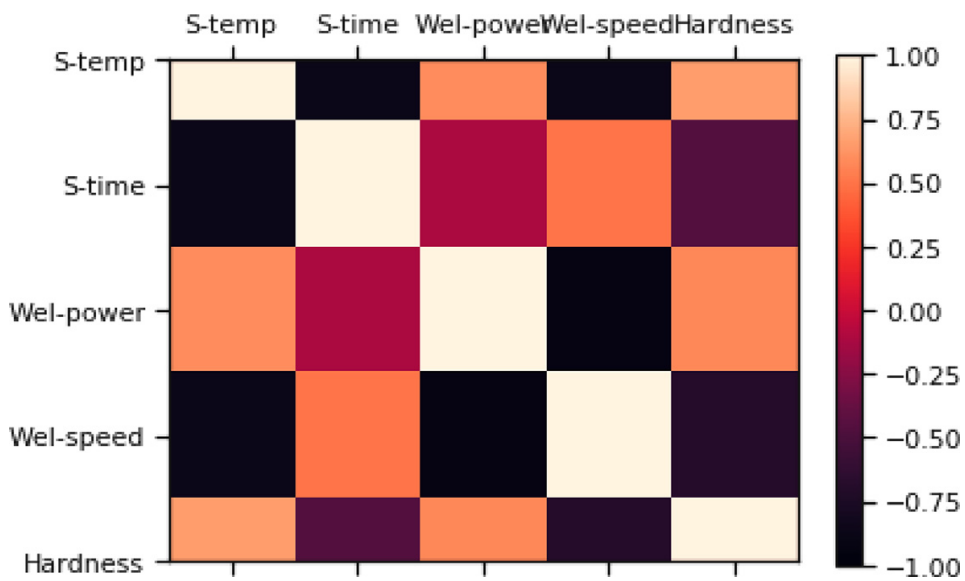
Fig. 1. Seaborn plot.

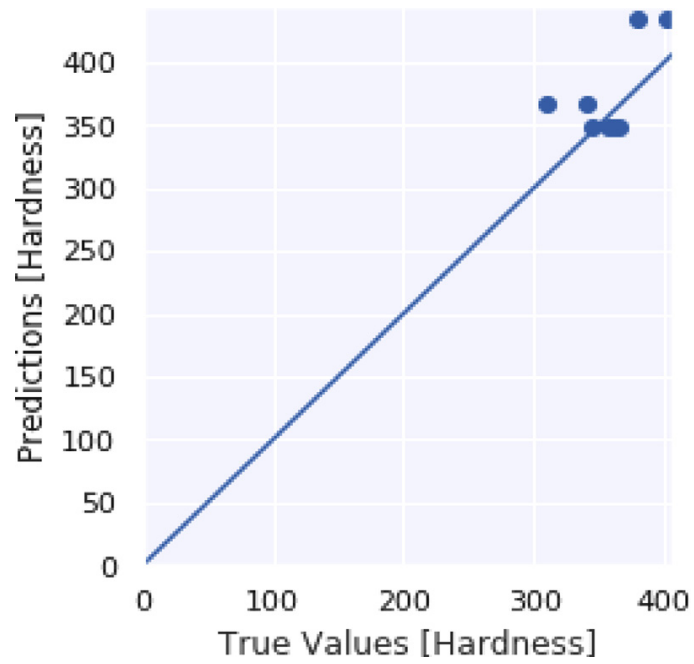

Fig. 2. Heat map visualization.

Fig. 3. Linear regression plot of hardness prediction values against the true value.
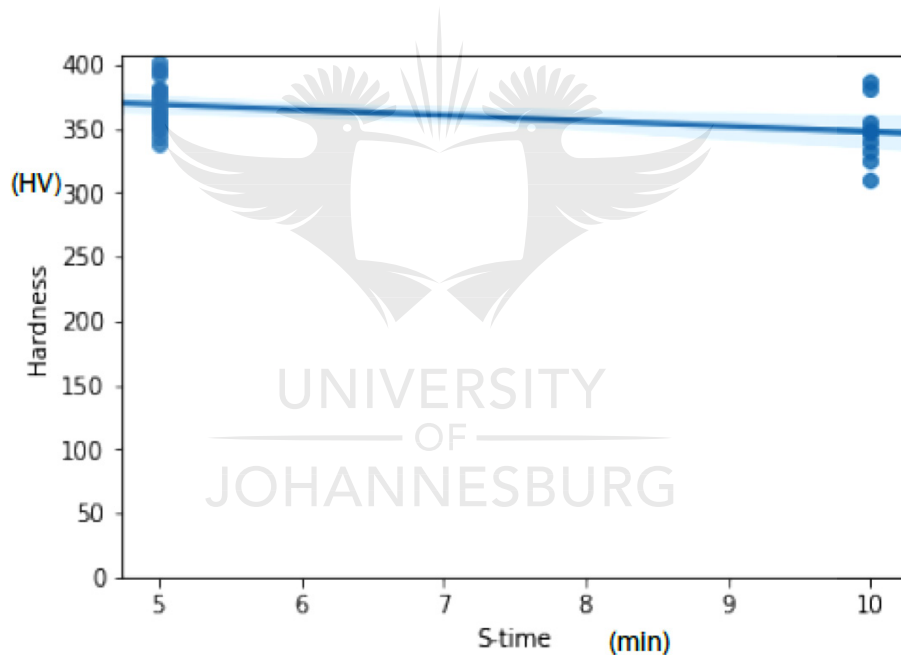

Fig. 4. Regression plot of hardness against Sintering time.

Table 4
Pearson correlation between Hardness and Wel-power.

	Hardness (HV)	Wel-power (W)
Hardness(HV)	1.0000	0.5824
Wel-power(W)	0.5824	1.0000

Table 5
Pearson correlation between Hardness and Wel-speed.

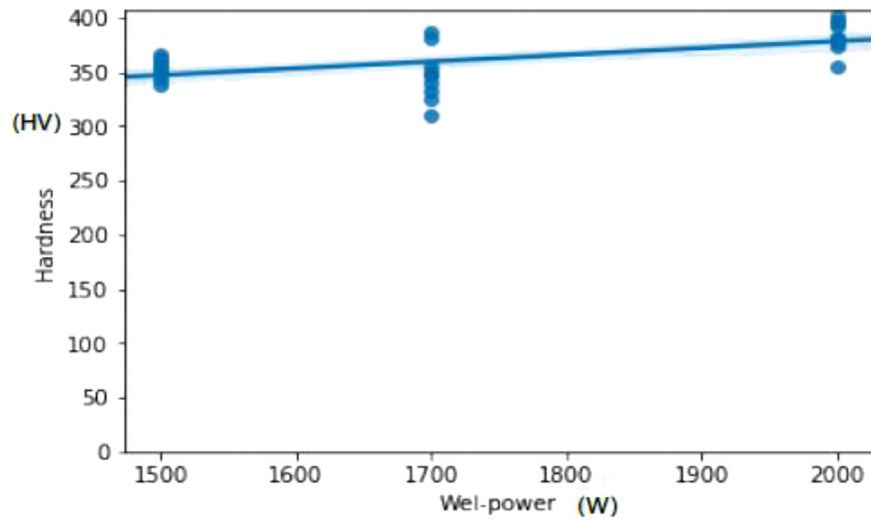|	Hardness (HV)	Wel-speed (m/min)
Hardness(HV)	1.0000	−0.6892
Wel-speed(m/min)	−0.6892	1.0000

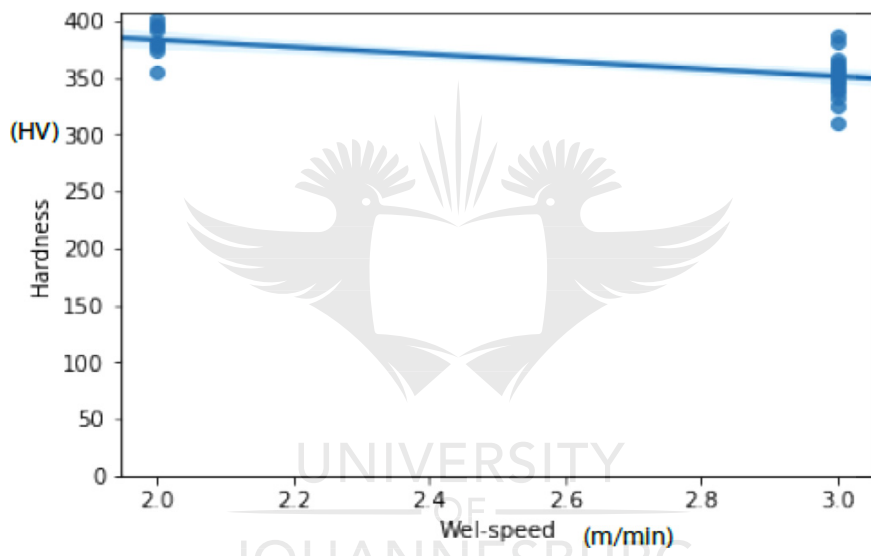**Fig. 5.** Regression plot of hardness against welding power.

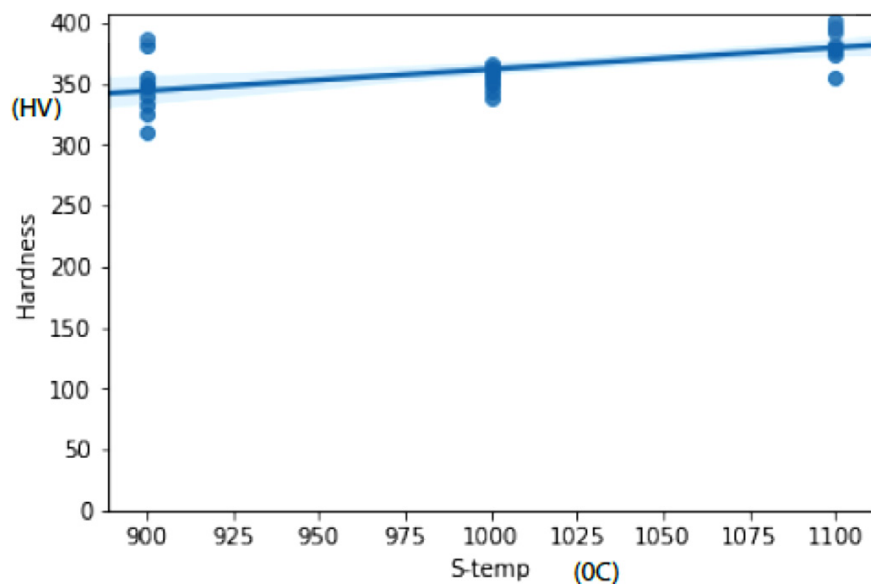**Fig. 6.** Pearson correlation of hardness and welding speed.

Fig. 7. Regression plot of hardness against sintering temperature.

Table 6
Pearson correlation between Hardness and S-temp.

	Hardness(HV)	S-temp (°C)
Hardness	1.0000	−0.6892
S-temp (°C)	0.6600	1.0000

2. Experimental design, materials, and methods

2.1. Fabrication of the materials using sintering and welding processes

2507 DSS powdered material whose compositions is shown in Table 1, was sintered with spark plasma sintering equipment SPS equipment (model HHPD-25, FCT system GmbH, Rauenstein, Germany, situated at Tshwane university of Technology Pretoria, South Africa). Meanwhile, the welding process proceded with the cutting of the sintered 2507 two parts of size (size: 12 × 12 × 3 mm^3), which was later prepared in butt configuration for the welding process. Laser welding equipment used is JK 600 pulsed Nd:YAG laser welding machine, at the council for scientific and industrial research (CSIR) South Africa. Also, parameters used in the data analysis was gotten from the sintering and welding processes as show in Table 2. Which form our predictor variables.

2.2. Microhardness

Hardenss of welded samples was carried using Vickers microhardness (Future Tech FM-700) tester, applying a load of 300 gf with dwell time of 10 s at room temperature. In this research, we consider Vickers microhardness at the weld zone (WZ). It has been indicated in literature that the chemical composition of the WZ goes along way to detrermine mechanical integrity of the welded metallic alloy, and it is also worthy to note that the microstructure of the WZ differs from the base metal (BM) because of the thermal history variation and differnce in chemical composition [2]. Also, for the data analsis, the Microhadness data form our targeted variable.

2.3. Data analysis

A raw dataset comprising of 30 instances was subjected to preprocesing using sklearn packges in tensor flow, for data cleaning, normalization, followed by splitting the data into 25% testing and 75%training set and eventually subjected it to regression analysis and visualized using different packages in tensor flow. The determination coefficient R^2, Pearson correlation coefficient, were determination coefficient on which we based benchmarking and prediction, respectively. Prediction data-set was used to test the model, also, process taking for the data analysis is shown in the taxonomical figure below.

Meanwhile, linear model was imported from scikit-learn, and from sklearn.linear_model, linear regression is imported, we then define the predictor variable and target variable. Normalization was performed using the Eq. (1) below.

$$Y = \frac{(Ymax - Ymin) * (X - Xmin)}{Xmax - Xmin} + Ymin \tag{1}$$

Where Y are the normalized datasets and X are input datasets. Eq. (2) was used to calculate the output datasets.

Eq. (2) represents the simple linear progression,

$$y = b_0 + b_1 x \tag{2}$$

x represent the predictor (independent) variable while target (dependent) variable y, while b_0 is intercept and b_1 is slope.

$$\text{Coefficient of determination or } R^2 = \left(1 - \frac{MSE \ of \ regression \ line}{MSE \ of \ the \ average \ data} \right) \quad (3)$$

MSE is mean square error, and R^2 is a measure or meteric we have useed to determine how close the dats is to fitted regression line in Fig. 3 to Fig. 7.

Pearson correlation is another metric we used to measure the strength of correlation between the hardness values and other predictor values.

2.3.1. Data visualization

Seaborn plot showed in Fig. 1 shows stastitical info-graphics four the data, providing high-level interface for stastical analysis and variation of hardness to dependent variables 'wel-power', 'S-temp', 'S-time', and 'wel-speed'.

Heat map plots in Fig. 2 was used to visualize data and it shows target variable (Hardness) proportional to colour with respect to variables, 'wel-power', 'S-temp', 'S-time', and 'wel-speed' in the vertical and horizontal axis respectively. This allows us to visualize the Hardness is related to 'wel-power', 'S-temp', 'S-time', and 'wel-speed'.

2.4. Code implemented

"""Copy of Copy of Copy of Copy of model.ipynb

Automatically generated by Colaboratory.

Original file is located at

https://colab.research.google.com/github/AyorindeTayo/Artificial-Neural-Network-for-Mechanical-Hardness-property-of-Welded-DSS-/blob/master/Copy_of_Copy_of_Copy_of_Copy_of_model.ipynb⟨?PMU?⟩

In this notebook, I am going to implement a simple linear regression model with tensorflow. We are going to predict the Hardness of a welded material in term of the welding power, speed, time.

"""

```
# importing the tensorflow package and other auxilary packages
import tensorflow as tf
import numpy as np
import pandas as pd
import seaborn as sns
import matplotlib.pyplot as plt
from tensorflow import keras
from sklearn.pipeline import Pipeline
from sklearn.preprocessing import StandardScaler,PolynomialFeatures
from sklearn.datasets import make_classification
from matplotlib import pyplot as plt
from sklearn.linear_model import LogisticRegression
sns.set()
```

"""##1. Loading the data with pandas"""

```
# Loading the data with the pandas read_csv attribute
from google.colab import files
```

```
files.upload()

df=pd.read_excel('data_1004.xlsx')
data = pd.DataFrame(df)

def boxplot(df,x,y):
    ax = sns.boxplot(x="x", y="x", data=df)

# Renaming the feature and looking at the data
data

# The shape of our data.
data.shape

# looking at the type of the data
data.dtypes

"""##1. Box plotting"""
ax = sns.boxplot(x="S-temp", y="Hardness", data=df)

ax = sns.boxplot(x="S-time", y="Hardness", data=df)

ax = sns.boxplot(x="Wel-power", y="Hardness", data=df)

ax = sns.boxplot(x="Wel-speed", y="Hardness", data=df)

df.plot(kind='box',figsize=(15,15), subplots=True, layout=(3,3), sharex=False, sharey=False)
plt.show()
```

"""One could do more plotting but we are ok now to build up our model. But first of all let us write a function that will help normalize our data.

##3. Definig the function to normalize the data
Normalization is very important in machine learning as building a model on a raw data set may result in poor performance of the model. It is always advisable to do so before feeding the data into your machine learning algorithm.
"""

```
#This function will return the normalized data
def Normalize(x):
    return (x-np.mean(x))/np.std(x)
```

"""##4- Splitting the data in test and train set"""

```
#I steal this from tensorflow tutorial. One could also used the split function in sklearn.
train_set=data.sample(frac=0.75,random_state=0)
test_set=data.drop(train_set.index)
```

"""## 5. Data visualisation and statistics"""

```
sns.set() sns.pairplot(train_set, height=3);

train_set.describe()
```

"""## 6. Defining the labels"""

```
train_labels=train_set.pop('Hardness')
test_labels=test_set.pop('Hardness')
```

"""##3. Defining and compiling the model
Next we will create the simplest possible neural network. It has 1 layer, and that layer has 1 neuron, and the input shape to it is just 1 value.

```python
"""

def build_model():
  model = keras.Sequential([
  keras.layers.Dense(64, activation=tf.nn.relu, input_shape=[len(train_set.keys())]),
  keras.layers.Dense(64, activation=tf.nn.relu),
  keras.layers.Dense(1)
])

optimizer = tf.keras.optimizers.RMSprop(0.001)

model.compile(loss='mse',
    optimizer=optimizer,
    metrics=['mae','mse'])
return model

model=build_model()
model.summary()

"""##
Training the model
Here we are going to train our model by feeding into the model the training sets of data
(features and labels).
"""

history = model.fit(
  train_set, train_labels,
  epochs=150, validation_split = 0.2, verbose=0)

hist = pd.DataFrame(history.history)
hist['epoch'] = history.epoch
hist.tail()

"""## Plotting the results"""

def plot_history(history):
  hist = pd.DataFrame(history.history)
  hist['epoch'] = history.epoch

plt.figure()
plt.xlabel('Epoch')
plt.ylabel('MAE for concrete strength')
plt.plot(hist['epoch'], hist['mean_absolute_error'],
  label='Train
  Error') plt.plot(hist['epoch'], hist['val_mean_absolute_error'],
  label = 'Val Error')
#plt.ylim([0,5])
plt.legend()

plt.figure()
plt.xlabel('Epoch')
plt.ylabel('MSE [concrete strength]')
plt.plot(hist['epoch'], hist['mean_squared_error'],
  label='Train Error')
plt.plot(hist['epoch'], hist['val_mean_squared_error'],
  label = 'Val Error')
#plt.ylim([0,20])
plt.legend()
```

```python
plt.show()

plot_history(history)

model=build_model()
early_stop = keras.callbacks.EarlyStopping(monitor='val_loss', patience=10)

history = model.fit(train_set, train_labels, epochs=150,
        validation_split=0.2, verbose=0, callbacks=[early_stop])

plot_history(history)

hist = pd.DataFrame(history.history)
hist['epoch'] = history.epoch
hist.tail()

loss, mae, mse = model.evaluate(test_set, test_labels, verbose=0)

print("Testing set Mean Abs Error: {:5.2f} Hardness".format(mae))

test_predictions = model.predict(test_set).flatten()

plt.scatter(test_labels, test_predictions)
plt.xlabel('True Values [Hardness]')
plt.ylabel('Predictions [Hardness]')
plt.axis('equal')
plt.axis('square')
plt.xlim([0,plt.xlim()[1]])
plt.ylim([0,plt.ylim()[1]])
_ = plt.plot([-1000, 1000], [-1000, 1000])

test_predictions

test_labels

Normalize(train_set)

Normalize(train_labels)

sns.pairplot(data, hue="Hardness", palette="husl")

"""Plotting *italicized text*"""

df.plot(kind='density',figsize=(15,15), subplots=True, layout=(3,3), sharex=False)
plt.show()

import seaborn as sns; sns.set(style="ticks", color_codes=True)
sns.pairplot(data)

sns.pairplot(data, hue="Hardness")

sns.pairplot(data, hue="Wel-speed", markers=["o", "s"])

sns.pairplot(data, kind="reg")

corr_matrix=df.corr()
corr_matrix

names=['S-temp','S-time','Wel-power','Wel-speed','Hardness']
fig = plt.figure()
ax = fig.add_subplot(111)
cax = ax.matshow(corr_matrix, vmin=-1, vmax=1)
fig.colorbar(cax)
```

```
ticks = np.arange(0,5,1)
ax.set_xticks(ticks)
ax.set_yticks(ticks)
ax.set_xticklabels(names)
ax.set_yticklabels(names)
plt.show()

"""**ANOVA ANALYSIS**"""

df.corr()

"""We can use the Pandas method corr() to find the feature other than price that is most
correlated wit
price"""
df.corr()['Hardness'].sort_values()

sns.regplot(x="Hardness", y="Wel-speed", data=df)
plt.ylim(0,)

df[["Hardness", "Wel-speed"]].corr()

sns.regplot(x="Hardness", y="Wel-power", data=df)

plt.ylim(0,)

df[["Hardness", "Wel-power"]].corr()

sns.regplot(x="S-temp", y="Hardness", data=df)
plt.ylim(0,)

df[["Hardness", "S-temp"]].corr()

sns.regplot(x="Hardness", y="S-time", data=df)
plt.ylim(0,)

df[["Hardness", "S-time"]].corr()

from scipy import stats

pearson_coef, p_value = stats.pearsonr(df['Hardness'], df['Wel-power'])
print("The pearson Correlation Coefficient is", pearson_coef, "with a p-value of p =", p_value)

pearson_coef, p_value = stats.pearsonr(df['Hardness'], df['S-temp'])
print("The pearson Correlation Coefficient is", pearson_coef, "with a p-value of p =", p_value)

pearson_coef, p_value = stats.pearsonr(df['Hardness'], df['S-time'])
print("The pearson Correlation Coefficient is", pearson_coef, "with a p-value of p =", p_value)

pearson_coef, p_value = stats.pearsonr(df['Hardness'], df['Wel-speed'])
print("The pearson Correlation Coefficient is", pearson_coef, "with a p-value of p =", p_value)

"""To see if different types 'Wel-power' impact 'Hardness"

**MODEL DEVELOPMENT**
"""

import matplotlib.pyplot as plt
from sklearn.linear_model import LinearRegression

X = df[['Wel-power']]
Y = df['Hardness']
lm = LinearRegression()
lm.fit(X,Y)
```

```
lm.score(X, Y)
```

```
features =["S-temp", "S-time","Wel-power","Wel-speed"]
```

"""We can Fit a linear regression model using the longitude feature 'long' and caculate the R^2."""

```
X=df[['S-temp','S-time','Wel-power','Wel-speed']]
Y=df['Hardness']
lm.fit(X,Y)
lm.score(X,Y)
```

"""Create a list of tuples, the first element in the tuple contains the name of the estimator:'scale'
'polynomial' 'model'"""

```
Input=[('scale',StandardScaler()),('polynomial',
PolynomialFeatures(include_bias=False)),('model',LinearRegression())]
```

"""We use the list to create a pipeline object, predict the 'price', fit the object using the features in the list features, then fit the model and calculate the R^2"""

```
Input= [('scale', StandardScaler()), ('polynomial',
PolynomialFeatures(include_bias=False)),('model',LinearRegression())]
pipe=Pipeline(Input)
pipe
X=df[['S-temp','S-time','Wel-power','Wel-speed']]
Y=df['Hardness']
```

```
pipe.fit(X,Y)
```

```
pipe.score(X,Y)
```

"""**MODEL EVALUATION AND REFINEMENT**"""

```
from sklearn.model_selection import cross_val_score
from sklearn.model_selection import train_test_split
print("done")
```

we will split the data into training and testing set""" features =["S-temp", "S-time","Wel-power","Wel-speed"]

```
X = df[features]
Y = df['Hardness']
```

```
x_train, x_test, y_train, y_test = train_test_split(X, Y, test_size=0.15, random_state=1)
```

```
print("number of test samples:", x_test.shape[0])
print("number of training samples:",x_train.shape[0])
```

Create and fit a Ridge regression object using the training data, setting the regularization parameter to 0.1 and calculate the R^2 using the test data.**"""

```
from sklearn.linear_model import Ridge
```

```
RigeModel = Ridge(alpha=0.1)
RigeModel.fit(x_train, y_train)
yhat = RigeModel.predict(x_test)
Rsqu_test= RigeModel.score (x_test,y_test)
print(Rsqu_test)
```